ETH
Eidgenössische Technische Hochschule Zürich
Swiss Federal Institute of Technology Zurich

Inhomogeneous Condensation in quark-based QCD Effective Models via Wavelet Pseudoparticles

Master Thesis
Philipp Maximilian Schicho
03/08/2016

Supervisor:
Prof. Dr. Philippe de Forcrand
Insitute for Theoretical Physics, ETH Zürich

Abstract

Some exactly solvable models for QCD like the Gross-Neveu model in $(1+1)$ dimensions exhibit a crystal phase that becomes stable for large baryon chemical potential. Inspecting for the generality of this effect I investigate if a similar topological crystal may occur in higher dimensions and in QCD, respectively. Prior research using an unbiased finite-mode approach obviated the need for a specific functional ansatz for the condensate. This allowed to examine if the phase diagram of the Gross-Neveu model in $(3+1)$ dimensions shows an emergent crystalline phase for small chemical potential. However, towards high density, this phase becomes unstable such that other ansätze might become favourable. To this end, I propose to expand the fermion fields and the inhomogeneous condensate in terms of Daubechies wavelet bases. First, analytically known results for $(1+1)$ dimensional models (such as the Gross-Neveu model) are reproduced and compared within the pseudoparticle approach. Eventually, the same procedure is extended to higher dimensions.

Acknowledgements

Special thanks to Dr. Philippe de Forcrand for his thorough discussions, guidance and of course patience throughout the various stages of this work. Additionally, my gratitude goes to the other members of the Lattice QCD group at ETH Zurich namely Tobias Rindlisbacher, Oscar Åkerlund and Helvio Vairinhos for their dedicated conversations and programming advises during the preparation of this thesis. Finally, I wish to thank my parents for their unconditional support that opened the door for many opportunities during my studies – I could not appreciate it more.

Contents

Chapter 1

Introduction and Motivation

The crux of Quantum Chromodynamics (QCD) as a core part of the Standard Model (SM) regarding strong interaction between particles, remains in its lacking of low energy solutions. In order to investigate the theory at high energy, *asymptotic freedom* allows to make use of perturbative techniques with the coupling constant approaching zero. However, this does not hold at the other end of the energy spectrum where one has to revert to non-perturbative methods due to a large coupling constant. Low temperature QCD (below about 1 GeV) is believed to predict interesting phenomena as confinement. Fundamental degrees of freedom (d.o.f.) are quarks and gluons which constitute only colour-neutral composite particles. Only these bound states like baryons, mesons or even glueballs are expected to be observed. In turn nuclear physics describes the interaction between exactly these baryons namely protons and neutrons resulting from the residual strong force among their components. In pursuit of exploring this regime dominated by events concerning atomic nuclei, QCD offers all essential tools, provided we omit electromagnetic and electroweak forces.
We are interested in QCD in environments of high baryon density ρ_{B} and/or high temperature T. Under these extreme conditions we keep the theory at equilibrium and relate to thermodynamic observables. Mathematically the quantity that encompasses all the information is the grand canonical partition function $\mathcal{Z}(\mu_{\mathrm{B}}, T)$ which connects the baryon density ρ_{B} to the chemical potential μ_{B}. At finite temperature this means that eventually the phase diagram in the (μ_{B}, T)-plane becomes non-trivial. We sketch the conjectured diagram in Fig. 1.1. The partition function $\mathcal{Z}$ is obtained in the path integral formalism of QCD and in general poses an untenable task when calculating it from first principle. Only in the two limiting cases of high and low baryon density with negligible quark masses (chiral limit) QCD becomes analytically tractable to some extent.

An essential feature of the conjectured phase diagram of QCD is the existence of a confined phase i.e. a hadronic phase for low chemical potential and temperature. When increasing the temperature one encounters a first order transition and a deconfined phase of Quark Gluon Plasma (QGP) in accordance with high energy (perturbative) QCD. On the other hand, at low temperature and higher baryon chemical potential nuclear matter exists around the mass of the proton $\mu_{\mathrm{B}} = \mathcal{O}(m_p = 1 \text{ GeV})$. Furthermore, at ultra high baryon densities a *colour-flavour locked* (CFL) phase resembling a superfluid (like cold nuclear matter) with broken chiral symmetry (c.f. Hadronic Gas) emerges. Interestingly, this sector of the theory can be understood rigorously. As μ_{B} becomes large the coupling decreases and observables can be computed from first principles. This is the upper limit in μ_{B} where the partition function $\mathcal{Z}$ can be calculated at least to leading order [1].
However, the focus of this thesis lies in the regime of a speculated phase boundary at intermediate baryon densities where the temperature is kept low. The point is that if the CFL terrain extends all the way down to nuclear matter we would already have full under-

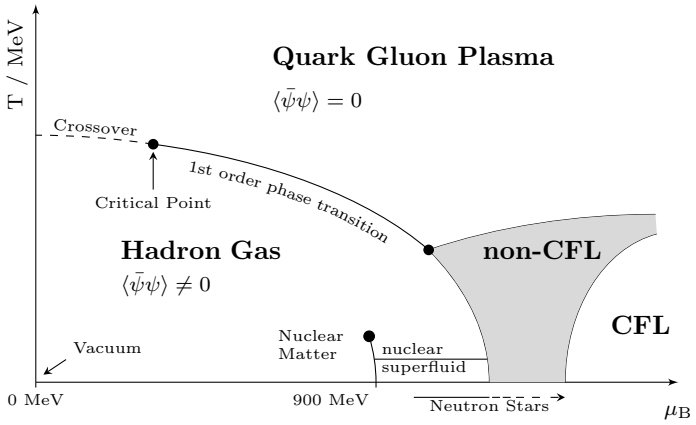

Fig. 1.1: Schematic outline of the conjectured QCD phase diagram featuring a hadronic, QGP, colour superconducting phases (non-CFL, CFL) as well as a first order deconfinement transition ending in the QCD critical endpoint.

standing of the phenomena therein. Currently very little is known about the existence and nature of this phase denoted as *non*-CFL because perturbative techniques are defeated by a high valued coupling constant as mentioned before. Ideally a non-perturbative option would be to revert to lattice QCD and conduct a brute-force Monte-Carlo simulation of the QCD path integral. Unfortunately due to the *sign problem* [2], standard algorithms tackling the intermediate density region are ruled out.

The remaining non-perturbative gap under these conditions urges towards a tradeoff by considering alternative i.e. *effective* models. These inherit as many features of the original theory as possible - especially chiral symmetry. Therefore, different versions regarding either chiefly hadronic or quark degrees of freedom have been proposed. During the study in this thesis we restrict ourselves to the latter option among which the Gross-Neveu (GN) model [3] and the Nambu-Jona-Lasinio (NJL) model [4, 5, 6] with four-fermi interaction are most prominent. Their uniting property, chiral symmetry breaking (χSB), gives rise to a chiral condensate σ which is equivalent to the quark-antiquark expectation value in quark constituent models $\langle\bar{\psi}\psi\rangle$.
In the large N_f limit, with N_f-the number of fermion flavours, one determines the condensate via minimisation of the effective action. A first naive attempt includes a spatially homogeneous condensate. The phase structure of the GN model in $(1+1)$ dimensions was already determined in 1985 [7] but was hard to reconcile with the known baryon spectrum. Only in 2000 after trading translational invariance for an inhomogeneous condensation $\sigma = \sigma(\mathbf{x})$ this issue was analytically resolved utilising Jacobi elliptic functions [8]. Motivated through the gaseous hadronic phase at low density, the revised phase diagram then included a soliton crystal phase built from baryons [9] in which the condensate assumed kink-solutions with wavelengths inversely proportional to the baryon density. Consequently the transitions between all three, the massive, crystal and massless matter phase were of second order.
Knowing that the GN model already provides a wide range of QCD-like properties, studies conjectured that an equivalent behaviour could also be found in QCD non-CFL phases using three dimensional models like the NJL model, respectively [10]. The significance of this argument originating from $(1+1)$ dimensional models is especially noted when considering high density $(3+1)d$ QCD which then naturally becomes a $(1+1)d$ theory [11] when translation invariance is broken in one spatial direction only.

Among numerous seemingly straightforward attempts to establish an unbiased universal algorithm independent of functional ansätze to evaluate chiral condensates at non-zero temperature and chemical potential, any practical realisation is subject to high computational costs. Generally one employs a condensate only dependent on a single spatial coordinate i.e. $\sigma = \sigma(x_3)$ which, discretised by use of lattice regularisation, produces the GN model correctly [12]. Nevertheless, as an ultimate goal we aim to reduce the degrees of freedom in the parameter space of the condensate and the fermion fields. To this end, studies propose usage of special basis functions localised in space and time also known as the *pseudoparticle approach*, which will serve as the main ingredient on our search for a crystal phase in QCD. We will expand both the chiral condensate and fermion functions in terms of plane waves [13], B-Splines [14] and eventually conduct a phase boundary determination adopting wavelets. As an orthonormal basis with compact support and very good approximation of not too heavily oscillating functions their distinct advocates in applied mathematics are Daubechies wavelets [15] that we mostly target as possible candidates. The search for a reliable numerical procedure to tackle also totally spatially inhomogeneous condensation without restrictions on the condensate ansatz triggered investigations leading to this thesis. We aim to successfully implement such a general method to study inhomogeneous condensation and give new insight on non-perturbative ntermediate density QCD. In addition, this permits to also verify hypothesised properties and shapes of condensates like chiral density waves (CDW) [16, 10].

We organise the thesis by classifying quark-based effective models in Ch. 2 according to QCD related features, symmetries and formulations. In Ch. 3 the pseudoparticle approach, possible candidate functional bases and nomenclature are introduced in order to set the stage for regularising the $(1 + 1)d$ GN model in Ch. 4. Additional focus lies on unbiased numerically determined phase diagrams investigating inhomogeneous condensation. Eventually, Ch. 5 is devoted to the same approach adapted for the three dimensional GN model reconstructing the phase transition between constant σ and spatially inhomogeneous $\sigma(x)$ at high density. Finally, we draw conclusions and devise possible improvements based on our results in Ch. 6 followed by an outlook on applications of wavelets in Quantum Field Theory.

Chapter 2

Classification of Quark-Based Effective Models

As argued in the introduction we exploit features of effective QCD toy models as an alternative non-perturbative method in order to investigate intermediate density regions of the phase diagram. We restrict ourselves only to quark degrees of freedom such that gauge fields are neglected for the remainder of the thesis. Also the models are studied at zero bare quark mass i.e. in the *chiral limit*.
Therefore, in this chapter we recall essential concepts of these simplified continuum models that exhibit inhomogeneous condensation. Including necessary augmentations towards QCD, the most important Lagrangians for both (1+1) as well as (3+1) dimensional models are presented. At this point the Euclidean path integral as a quantisation prescription is proposed

$$\langle \mathcal{O} \rangle = \frac{1}{\mathcal{Z}} \int \mathcal{D}\bar{\psi}\mathcal{D}\psi\mathcal{D}\phi\, \mathcal{O}\left[\bar{\psi}, \psi, \phi\right] e^{-S\left[\bar{\psi},\psi,\phi\right]}, \tag{2.1}$$

$$\mathcal{Z} = \int \mathcal{D}\bar{\psi}\mathcal{D}\psi\mathcal{D}\phi\, e^{-S\left[\bar{\psi},\psi,\phi\right]} \tag{2.2}$$

for observables $\mathcal{O}$ and the partition function $\mathcal{Z}$. Here the field ϕ is an arbitrary bosonic field like the non-abelian gauge field in QCD or simply the chiral condensate $\phi \to \sigma \sim \langle \bar{\psi}\psi \rangle$ of the Gross-Neveu model (cf. Sec. 2.1). Focusing on theories exclusively built from constituent massless quarks $m_0 = 0$ we will encounter so-called Q-operators which we will refer to as *enhanced* Dirac operators. These are very similar to the pure Dirac operator $D = \not{\partial}$ except for an additional bosonic potential $V(\phi)$

$$Q = \not{\partial} + V(\phi) = \gamma_i \partial_i + \gamma_0(\partial_0 + \mu) + V(\phi) \tag{2.3}$$

Also the bosonic fields ϕ enter in this yet general bosonic term

$$Q = \underbrace{\not{\partial} + \gamma_0\mu}_{\text{Dirac operator}} + \underbrace{V(\phi).}_{\text{bosonic potential}} \tag{2.4}$$

The affixed baryon chemical potential μ (dropping the subscript $_{\mathrm{B}}$) is introduced along the temporal derivative and coupled to the quark charge $\mu_{\mathrm{B}} = N_{\mathrm{f}}\mu_{\mathrm{q}}$.

In the follow-up different regularisation schemes are proposed to implement further calculations and determine the shape of σ in subsequent chapters. The main ingredient is given by the effective action after transforming away the prevailing four-Fermi interactions.

2.1 Gross-Neveu Models

Exploratory models at low dimensionality often already feature a genuine set of QCD-like properties. Models proposed by *Gross* and *Neveu* (GN) [3, 8, 7, 17] enjoy either discrete or continuous chiral symmetry. We will elucidate both in the subsequent sections.

2.1.1 Chirally discrete GN model in 1+1 dimensions

Yet the discrete-symmetry version of the $(1+1)d$ GN model (GN_2) constitutes a four-fermion interaction theory with a single flavour, N_c colour-degenerate massless quarks. Since the GN model is not a gauge theory, colours can be regarded as "flavours". To avoid ambiguities we refer to n_f as the number of flavours and its level of degeneracy $N = N_\mathrm{c}$ as colours. In the single flavour case $N_\mathrm{f} = 1$ these are often used interchangeable $N = N_\mathrm{f} = N_\mathrm{c}$.
in pursuit of features existing in QCD the model's most interesting regime - the large-N limit - displays asymptotic freedom, dynamical chiral symmetry breaking and its restoration, dimensional transmutation, and meson and baryon bound states. Stating the model in euclidean space time one obtains the Lagrangian density,

$$\mathcal{L}_\mathrm{GN} = \sum_{a=1}^{N} \bar{\psi}^a \not{\partial} \psi^a - \frac{g^2}{2} \left[\sum_{a=1}^{N} \bar{\psi}^a \psi^a \right]^2 , \tag{2.5}$$

with fundamental variables $\{\psi^a\}_{a=1}^n$ of n massless two spin component fermion fields in $(1+1)d$. subsequently, products and sums over colour indices a are implied and thus omitted. We observe from the kinetic term in eq. (2.5) the dimension of $\psi^a \sim [L]^{-\frac{1}{2}}$ which renders the four-fermion term two-dimensional and g dimensionless. The latter induces renormalisability upon the interaction term.
corresponding to the Clifford algebra in euclidean space where Dirac matrices fulfill $\{\gamma_\mu, \gamma_\nu\} = 2\delta_{\mu\nu}\mathbf{I}_2$ there exists a unique two-dimensional irreducible representation $\mathcal{C}\ell_{1,1}(\mathbb{R}) \cong \mathbb{R}(2) \cong \mathcal{C}\ell_{0,2}(\mathbb{R})$ isomorphic to the ring of two-by-two matrices over the real numbers. The two gamma matrices are given in terms of σ_i pauli matrices $\gamma_0 = \sigma_1$ and $\gamma_1 = \sigma_3$, with the additional $\gamma_5 = \gamma_0\gamma_1 = -i\sigma_2$ implying $\gamma_\mu = \gamma_\mu^\dagger = \gamma_\mu^*$ and $\{\gamma_5, \gamma_\mu\} = 0$.

Next, we discuss the regularisation of the model by defining the action from the Lagrangian density in eq. (2.5)

$$\mathcal{S}_\mathrm{GN}\left[\bar{\psi}, \psi\right] = \int \mathrm{d}x\, \mathrm{d}\tau\, \mathcal{L}_\mathrm{GN} \tag{2.6}$$

and its partition function $\mathcal{Z}$

$$\mathcal{Z} = \int \left(\prod_{a=1}^{n} \mathcal{D}\bar{\psi}^a \mathcal{D}\psi^a \right) e^{-S}. \tag{2.7}$$

an efficient means to replace the four-fermion coupling $(\sum_{i=1}^N \bar{\psi}^a\psi^a)^2$ is a Hubbard-Stratonovich transformation (cf. sec. A.1) which has no effect on physics. We wish to introduce a scalar auxiliary bosonic field, which we shall designate by $\sigma(x)$. The summation over colour a renders σ a singlet under $O(2n)$. Effectively the insertion of unity

$$\mathbf{I} = \int \mathcal{D}\sigma \exp\left\{ - \int \mathrm{d}x\, \mathrm{d}\tau \, \left[\frac{1}{\sqrt{2}g}\sigma - \frac{g}{\sqrt{2}} \bar{\psi}^a\psi^a \right]^2 \right\}. \tag{2.8}$$

disposes of quartic terms in ψ^a. For simplicity the operator Q from (2.4) is altered using the bosonic field $\phi \to \sigma$ and potential $v(\phi) \to \sigma$

$$q = \not{\partial} + \gamma_0\mu + \sigma \, , \tag{2.9}$$

which will be used when appropriate from now on. also the classical equations of motion and the Lagrangian (2.5) are recovered when integrating out σ

$$\begin{aligned}\mathcal{Z} &= \int \mathcal{D}\sigma \left(\mathcal{D}\bar{\psi}^a \mathcal{D}\psi^a\right) \exp\left\{-\mathcal{S}_{\mathrm{GN}} - \int \mathrm{d}x\, \mathrm{d}\tau \left[\frac{1}{\sqrt{2}g}\sigma - \frac{g}{\sqrt{2}}\bar{\psi}^a\psi^a\right]^2\right\} \\ &= \int \mathcal{D}\sigma \left(\mathcal{D}\bar{\psi}^a \mathcal{D}\psi^a\right) \exp\left\{-\int \mathrm{d}x\, \mathrm{d}\tau \left[\frac{1}{2g^2}\sigma^2 + \bar{\psi}^a Q \psi^a\right]\right\} . \end{aligned} \tag{2.10}$$

we are now able to write down an effective action

$$S_{\mathrm{eff}}[\sigma] = \int \mathrm{d}x\, \mathrm{d}\tau \left(\frac{1}{2g^2}\sigma^2 + \bar{\psi}^a q \psi^a\right) . \tag{2.11}$$

Besides, fermionic degrees of freedom ψ^a can also be bilinearly integrated out using $\int \mathcal{D}\bar{\psi}\mathcal{D}\psi \exp\left\{-\bar{\psi}a\psi\right\} = \det a$ via the functional determinant det(.)

$$\begin{aligned}&\int \mathcal{D}\bar{\psi}^a \mathcal{D}\psi^a \exp\left\{-\int \mathrm{d}x\, \mathrm{d}\tau \left(\bar{\psi}^a \left(\not{\partial} + \gamma_0\mu\right)\psi^a + \sigma\bar{\psi}^a\psi^a\right)\right\} \\ &\qquad = \left[\det\left(\not{\partial} + \gamma_0\mu + \sigma\right)\right]^N , \end{aligned} \tag{2.12}$$

to recover an effective action solely dependent on even powers of the auxiliary field σ because of vanishing traces over odd γ matrices vanish. Especially also as a result of the change in sign of σ due to γ in eq. (2.17)

$$\begin{aligned}\mathcal{Z} &= \int \mathcal{D}\sigma \left[\det Q\right]^N \exp\left\{-\int \mathrm{d}x\, \mathrm{d}\tau\, \frac{1}{2g^2}\sigma^2\right\} \\ &= \int \mathcal{D}\sigma \exp\left\{n \log\left(\det Q\right)\right\} \exp\left\{-\int \mathrm{d}x\, \mathrm{d}\tau\, \frac{1}{2g^2}\sigma^2\right\} \\ &= \int \mathcal{D}\sigma \exp\left\{-\int \mathrm{d}x\, \mathrm{d}\tau\, \frac{1}{2g^2}\sigma^2 + N \log\det Q\right\} . \end{aligned} \tag{2.13}$$

with the Dirac operator in (2.9), the partition function gives rise to a restated effective action (2.11) utilising the redefinition of the coupling constant eq. (2.21)

$$S_{\mathrm{eff}}[\sigma] = \int \mathrm{d}x\, \mathrm{d}\tau\, \mathcal{L}_{\mathrm{eff}} = N\left\{\int \mathrm{d}x\, d\tau\, \frac{1}{2\lambda}\sigma^2 - \frac{1}{2}\log\det Q^\dagger Q\right\} . \tag{2.14}$$

We already got ahead of the discussion by replacing the argument of the determinant in (2.14)

$$\left(\det Q\right)^2 = \det(Q^\dagger Q) \geq 0. \tag{2.15}$$

Remark 2.1 *The identity* (2.15) *is only valid if* $\det Q$ *is real. To prove this assumption one can check the eigenvalues* λ *of* Q*. For the Dirac operator* Q *there are only two possibilities when acting on its eigenfunction* $f(x)$ *with eigenvalue* α*, namely (i)* $qf(x) = (\not{\partial} + \sigma)f(x) = \alpha f(x)$ *or (ii)* $Qf(x) = (\not{\partial} + \sigma)f^*(x) = \alpha^* f^*(x)$*. This signifies that the* λ *come in complex conjugate pairs or are real in the first place such that the determinant as a product over diagonal elements itself remains real valued.*

Remark 2.2 *Naturally the product of Dirac operators* $Q^\dagger Q$ *will be hermitian*

$$Q^\dagger Q = \left(Q^\dagger Q\right)^\dagger = Q^\dagger \left(Q^\dagger\right)^\dagger = Q^\dagger Q$$

such that the inequality of the right-hand side of (2.15) *is fulfilled.*

The salient point along this seemingly innocent mathematical change is its numerical stability which will be elaborated in more detail below (cf. sec. 3.1.1). Certainly this is only true for even n supported by

$$\log\det Q = \mathrm{Tr}\,\log Q. \tag{2.16}$$

Due to its $O(2n)\times\gamma$ global symmetry (2.5) is invariant under the discrete γ_5 transformation

$$\gamma: \quad \psi^a \to \gamma_5\psi^a\,, \quad \bar\psi^a \to -\bar\psi^a\gamma_5\,, \quad \sigma\to-\sigma. \tag{2.17}$$

Note that $\bar\psi^a = \psi^{a\dagger}\gamma_0 \to \psi^{a\dagger}\gamma_5\gamma_0 = -\bar\psi^a\gamma_5$. However, the mass term will transform as

$$m\bar\psi^a\psi^a \to -m\bar\psi^a\psi^a\,. \tag{2.18}$$

Hence, the theory respecting chiral symmetry does not allow a mass term. We classify γ as Z_2 symmetry as twice the action of $(\gamma_5)^2 = 1$ is trivial. Obviously the Lagrangian (2.5) is unaffected by a $U(n)$ transformation. On the other hand, the prevalent continuous global symmetry is $O(2n)$ for which $U(n)$ is a subgroup [9]. This is the *isospin* symmetry and responsible for rotation in the space of colour degenerate massless flavours ψ^a. This can be seen when expanding

$$\psi^a = \xi_1^a + i\xi_2^a \tag{2.19}$$

into hermitian two-component spinors $\xi_{1,2}$. This signifies that $\{\xi^a_{1,2}\}_{a=1}^n$ is a $2n$ component vector with apparent $o(2n)$ symmetry

$$\xi(x,\tau) = r\xi(x,\tau)\,, \quad r\in O(2n)\,. \tag{2.20}$$

so far we have not given any details on the n degeneracy which, however, plays an essential role in the discrete $(1+1)d$ GN model. For $1<n<\infty$ its solution is neither trivial nor analytically tractable. Nevertheless, for finite n one of the most pressing QCD connections, chiral symmetry breaking, is still intact. In fact, the discrete Z_2-symmetry in γ forbids the existence of massless Goldstone bosons but the theory still exhibits χSB for $t=0$ at all

$$\lambda = g^2N \tag{2.21}$$

fixed with λ the t'hooft coupling. This does not contradict the Mermin-Wagner-Coleman theorem [18, 19] because Z_2 is discrete and not continuous. However, χSB with mass generation becomes non-trivial and dynamical but was shown to exist by Gross and Neveu [3]. A non-vanishing $\sigma\sim\langle\bar\psi\psi\rangle$ as the vacuum expectation value (VEV) $\sigma_0 = \langle 0|\sigma|0\rangle = \langle\sigma\rangle$ then yields a non-zero fermion mass.
the failure of dynamical symmetry breakdown to occur for any finite n in $(1+1)d$ was demonstrated [20]. The core issue concerns the logarithmic $2d$ euclidean massless σ-boson propagator which favours cheap long-range fluctuations [19] destroying any sort of ordering. Only for diverging number of fermions spontaneous mass generation resurfaces when suppressing fluctuations sufficiently such that the interaction term equals a constant for large-N limits

$$\big\langle\bar\psi(x)\psi(x)\bar\psi(y)\psi(y)\big\rangle = \langle\sigma(x)\sigma(y)\rangle \sim 1+\frac{1}{n}\log|x-y| + \mathcal{O}(1/n^2)\,. \tag{2.22}$$

Following these arguments, we consider the large-N limit from this point on such that an analytic solution is possible. From the fact that $S_{\text{eff}}\propto N$ counting powers in N becomes simple. As a result the new partition function

$$\mathcal{Z}\propto\int\mathcal{D}\sigma\, e^{-S_{\text{eff}}[\sigma]}\,, \tag{2.23}$$

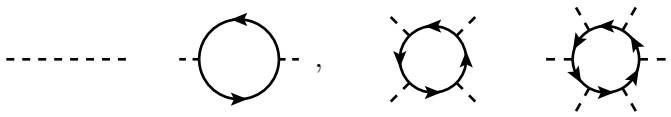

Fig. 2.1: Diagrams in the $1/N$ expansion of the Gross-Neveu effective Lagrangian $\mathcal{L}_{\text{eff}}$ in leading order of the large-N_{f} expansion based on Feynman rules in sec. A.2. With dashed and solid lines corresponding to the auxiliary field σ and the fermion field ψ, respectively.

is directly dominated by a field saddle point configuration where S_{eff} becomes minimal with respect to σ and admits the standard *gap equation* (cf. sec. 2.1.2) meaning

$$\lim_{N\to\infty} S_{\text{eff}}[\sigma, N] = \inf_{\sigma} S_{\text{eff}}[\sigma, N] \,, \tag{2.24}$$

and its solution being exact for large-N. Moreover, σ is a large-N invariant and in minimum acquired in eq. (2.24) it assumes the role of a fermionic mass term resulting from perturbations. At the beginning of this section we hinted that the GN model exhibits renormalisation. To this end, we inspect the leading order (LO) diagrammatic contribution in the $1/N$ expansion equal to $\mathcal{L}_{\text{eff}}[\sigma, \lambda, n] = N\tilde{\mathcal{L}}_{\text{eff}}[\sigma, \lambda]$ depicted in Fig. 2.1. To delve into answering this question we compute the β-function by dimensional regularisation of the integral in eq. (2.12) yielding in momentum space

$$\begin{aligned}\int \mathcal{D}\bar{\psi}^a \mathcal{D}\psi^a \exp\left\{-\int \mathrm{d}x\, d\tau\, \bar{\psi}^a \left(\not{\partial} + \sigma\right) \psi^a\right\} \\ = \exp\left\{\int \frac{d^2k}{(2\pi)^2} n \log\left(k^2 + \sigma^2\right)\right\} \,.\end{aligned} \tag{2.25}$$

Naturally the Fourier transformation (2.25) has this simple form only if σ is translationally invariant. In arbitrary dimensions d the integrand is restated in the limit of $d = 2 - \epsilon$ and $\epsilon \to 0$ employing the γ-function [21]

$$\begin{aligned}\int \frac{d^dk}{(2\pi)^2} n \log\left(k^2 + \sigma^2\right) = \quad & \frac{N}{(4\pi)^{\frac{d}{2}}} \frac{2}{d} \gamma(1 - \frac{d}{2}) (\sigma^2)^{\frac{d}{2}} \\ \overset{\lim_{\epsilon\to 0}}{=} \quad & \frac{n\sigma^2}{4\pi} \left(\frac{2}{\epsilon} - \gamma + \log(4\pi) - \log(\sigma^2) + 1\right) \,.\end{aligned} \tag{2.26}$$

as the low energy regime, that is the infrared (IR) behaviour, poses most interest we place a momentum cut-off $k^2 \leq \lambda^2$. This renders the $\sigma^2 \sim [m]^2$ argument of the logarithm on the right-hand side dimensionless again. Together with eq. (2.14) the effective potential equipped with a renormalisation condition at $\frac{\partial^2 \mathcal{L}_{\text{eff}}}{\partial \sigma^2}\big|_{\sigma=\mu} = 1$ yields

$$\mathcal{L}_{\text{eff}}[\sigma] = n \left[\frac{\sigma^2}{2\lambda^2} + \frac{1}{4\pi}\sigma^2 \left(\log \frac{\sigma^2}{\mu^2} - 3\right)\right] \,. \tag{2.27}$$

If we carry out the minimisation one finds that the effective potential admits global minima at $\sigma = \pm\sigma_0 = \pm\mu e^{1-\frac{\pi}{\lambda}}$. Therefore, the discrete γ-symmetry is broken and initially massless fermions realise a mass equal to σ_0 to lo. Eventually, we make use of the renormalisation group equation [22] to retrieve the β-function

$$\beta(\lambda) = -\frac{n-1}{2\pi}\lambda^3 + \mathcal{O}(\lambda^5) \,. \tag{2.28}$$

Here the negative sign of the leading term in (2.28) indicates an asymptotically free theory where the coupling vanishes towards high momenta. We also observe that (2.27) is now

independent of the cut-off λ due to the renormalisation condition at $\sigma = \sigma_0$. This result clearly shows the renormalisability of the theory.

Concluding a rather detailed description of a very simple toy model in the pursuit of QCD properties, we have already assembled enough similarities towards first finite temperature and density investigations.

2.1.2 The gap equation

As we argued before eq. (2.24) introduces the gap equation as the condition

$$\frac{\delta S_{\text{eff}}[\sigma]}{\delta \sigma(x)} = 0 \,, \tag{2.29}$$

that is responsible for minimising the effective action. In general eq. (2.29) yields a self consistency equation for the fermion condensate.
in order to illustrate this idea we start from the effective action (2.14) in the large-N limit with a single n-degenerate flavour fermion. We are looking for the field configuration corresponding to its extremum. As long as we assume a spatially inhomogeneous condensate $\sigma(x)$ we obtain a system of non-linear functional differential equations

$$\frac{\partial_{\sigma(x)} S_{\text{eff}}}{n} = \frac{\sigma(x)}{\lambda} - \partial_{\sigma(x)} \text{Tr} \, \log[\not{\partial} + \gamma_0 \mu + \sigma(x)] = 0 \,, \forall x \,, \tag{2.30}$$

where we applied eq. (2.16). For the time being the condensate is assumed to be translational invariant $\sigma(x) = \sigma$ giving rise to

$$\frac{\sigma}{\lambda} = \partial_\sigma \text{Tr} \, \log[\not{\partial} + \gamma_0 \mu + \sigma] \,. \tag{2.31}$$

Eventually after transition to momentum space one ends up with a self consistency equation additionally to the trivial solution where $\sigma = 0$

$$\frac{1}{\lambda} = \int \frac{d^2k}{(2\pi)^2} \frac{2}{k^2 + \sigma^2} \qquad \text{for} \quad \mu = 0, \tag{2.32}$$

which is considered as the gap equation of the discrete GN_2 model. Its solution with respect to the fermion condensate gives rise to the phase structure for finite μ and T. We will only focus on this gap equation approach. Other possibilities would involve solving e.g. Hartree-Fock equations.

Before proceeding to higher dimensions we briefly present a more general candidate theory in $(1+1)$ dimensions.

2.1.3 Chiral χGN model

For the first augmentation of the discrete GN case we present the following euclidean Lagrangian known as the chiral GN model (χGN)

$$\mathcal{L}_{\chi\text{GN}} = \bar{\psi}^a \not{\partial} \psi^a - \frac{g^2}{2} \left[\left(\bar{\psi}^a \psi^a \right)^2 + \left(\bar{\psi}^a i\gamma_5 \psi^a \right)^2 \right] \,. \tag{2.33}$$

With an extra pseudoscalar term $\bar{\psi}^a i\gamma_5 \psi^a$. The Lagrangian density in eq. (2.33) deals with invariance under Abelian chiral symmetry $U(1)_L \times U(1)_R$ which can be rewritten as $U(1)_V \times U(1)_A$ via $L \pm R = V/A$ under axial (A) and vector (V) symmetries. The crucial difference to the prior discussed discrete GN model is that for χGN the discrete

symmetry is enhanced to a continuous symmetry group $U_A(1)$. Fermion fields under this transformation are invariant

$$U_V(1): \quad \psi^a \to e^{i\alpha}\psi^a\,, \quad \bar{\psi}^a \to -e^{i\alpha}\bar{\psi}^a \tag{2.34}$$

$$u_a(1): \quad \psi^a \to e^{i\alpha\gamma_5}\psi^a\,, \quad \bar{\psi}^a \to e^{i\alpha\gamma_5}\bar{\psi}^a\,. \tag{2.35}$$

It is pivotal to understand that due to the continuous symmetry (2.34) now also a massless Goldstone boson appears. In two dimensions correlation functions of massless particles are infrared divergent. Thus, in contrast to the discrete GN model chiral symmetry is restored at any finite temperature in two dimensions. On the other hand, the Mermin-Wagner-Coleman theorem [18, 19] explicitly forbids the existence of Goldstone bosons in $(1+1)d$. At leading order, however, one observes the aforementioned massless π field. Does this contradict the theorem?
in fact one has to take into account all orders in the large-n expansion. Then no Goldstone bosons are present. Thus, in the attempt of an analytic solution chiral symmetry breaking only emerges at the limit of infinite fermions $n \to \infty$ suppressing other field configurations that possibly would prohibit χSB.
furthermore, in this model condensation may not only occur for the scalar field σ but also for a pseudoscalar field π that is related to the second term in brackets of (2.33) via $\pi \sim \langle \bar{\psi} i\gamma_5 \psi \rangle$. The effective action is obtained in the same way as for the discrete GN model (cf. sec. 2.1.1) by a Hubbard-Stratonovich transformation of the four-fermion terms

$$S_{\text{eff}}[\sigma,\pi] = N\left\{\int \mathrm{d}x\, d\tau\, \frac{1}{2\lambda}\left(\sigma^2+\pi^2\right) - \frac{1}{2}\log\det q^\dagger q\right\}\,,$$

$$\mathcal{Z} = \int \mathcal{D}\sigma\mathcal{D}\pi\, e^{-S_{\text{eff}}[\sigma,\pi]}\,, \tag{2.36}$$

with the coupling λ (2.21). Consequently the enhanced Dirac operator Q from (2.4) is varied adequately

$$Q = \not{\partial} + \gamma_0\mu + \sigma + i\gamma_5\pi. \tag{2.37}$$

With the effective actions eqs. (2.14) and (2.36) we have the necessary tools to investigate GN models, start solving gap equations and determine their phase structures. We now turn to the three dimensional Gross-Neveu model.

2.1.4 Chirally discrete GN model in 3+1 dimensions

As we will see for $d > 2$ a negative mass dimension of λ forbids perturbative renormalisation when considering the $(3+1)d$ Gross-Neveu model (GN_4). However, it is proven to be renormalisable by an $1/N$ expansion and closely related to the Higgs-Yukawa type models in the proximity of four dimensions [23]. We inspect the model with two four-component continuum fermion flavours such that the Lagrangian (2.5) for the $(1+1)d$ chirally discrete case is altered.

Let us first continue with a power counting argument of fermion fields to justify non-renormalisability in four space-time dimensions [3]. Since the fields ψ^a have dimension $[L]^{-\frac{3}{2}}$ the interaction term in (2.39) has dimension $[L]^{-6}$ compared to the Lagrangian density $\mathcal{L} \sim [L]^{-4}$. We keep g as the dimensionless coupling constant. However, the interaction term requires a coupling constant of dimension $[L]^2$ which we introduce via a cut-off

$$\frac{g^2}{2} = g\lambda^2. \tag{2.38}$$

In the chiral limit we then obtain for the euclidean Lagrangian for $N_{\text{f}} = 1$ flavours with degenerate $N_{\text{c}} = n \to \infty$ colours

$$\mathcal{L}_{\mathrm{GN}_4} = \bar{\psi}^a \not{\partial}\, \psi^a - g\left(\bar{\psi}^a\psi^a\right)^2 \tag{2.39}$$

with the replaced dimensionful coupling g. The number of colours N_c is now finite and for QCD it assumes $N_\mathrm{c} = 3$ which we will use for the $(3+1)d$ models. The corresponding symmetry group $\mathrm{SU}(2)_L \times \mathrm{SU}(2)_R$ with $U_L \in \mathrm{SU}(2)_L$ and $U_R \in \mathrm{SU}(2)_R$ leaves the Lagrangian (2.39) invariant

$$\psi_L^a \to U_L \psi_L^a \,, \quad \psi_R^a \to U_R \psi_R^a \,. \tag{2.40}$$

Thus, the fermion functions ψ_f^a are projected into left and right chiral components

$$\psi^a = \begin{pmatrix} \psi_1^a \\ \psi_2^a \end{pmatrix}, \quad \psi_L^a = P_L \psi^a \,, \quad \psi_R^a = P_R \psi^a \,. \tag{2.41}$$

A property of the vacuum is the dynamical fermion mass which we will call m_0^* with subscript $_0$ for the vacuum. The generation of m_0^* gives rise to the gap equation (cf. sec. 2.1.2)

$$m_0^* = -g \left\langle \bar{\psi}^a \psi^a \right\rangle > 0 \tag{2.42}$$

resulting from the Dirac equation for $\psi(x)$. The chiral condensate is defined [24, 5] to be constituent of field configurations $\bar{\psi}^a \psi^a$ and is an order parameter for dynamical χSB

$$\sigma = \left\langle \bar{\psi}^a \psi^a \right\rangle \,. \tag{2.43}$$

In this case the effective mass m_0^* and the condensate σ are translated into each other in the vacuum $\sigma_0 = -\frac{m_0^*}{g}$. The condensate σ in the mean field approximation takes the form [5]

$$\sigma = -N m_0^* I. \tag{2.44}$$

At this point we clearly observe that the model is not renormalisable. The integral term I results from the Dirac propagator

$$I = i \int \frac{d^4k}{(2\pi)^4} \frac{2}{k^2 - m_0^{*2}} = \int \frac{d^3k}{(2\pi)^3} \frac{1}{\sqrt{\mathbf{k}^2 + m_0^{*2}}} \,, \tag{2.45}$$

then yields a divergent integral after carrying out the k_0 integration on the right-hand side which contributes the square root in the denominator.
the divergence originates from the closed quark loop contribution in the quartic interaction term. The integral I is quadratically divergent and in order to compute meaningful results one has to define a renormalisation scheme. The latter introduces a high-energy scale cut-off λ with $k^2 < \lambda^2$. In contrast to the discrete GN_2 model the integral I still depends explicitly on λ after setting a renormalisation condition. Thus, for every λ we have to deal with a different model. All remaining parameters also become finite. The cut-off could then be implemented in (2.45). For finite density and temperature calculations it is favourable to either use the Pauli-Villars scheme, proper time regularisation or the three-momentum non-covariant cut-off [24].

First of all the latter has to be excluded when inspecting for inhomogeneous condensation. Otherwise, as empirically found, kink-antikink solutions are never realised when $|\mathbf{k}|$ is bounded by λ [25]. For the remainder of the discussion, we will then focus on the Pauli-Villars scheme. For this regularisation one introduces a set of n_pv fictitious heavy fermions of mass m_k and constants c_k

$$\begin{aligned} I &= \int \frac{\mathbf{k}^2 d|\mathbf{k}|}{2\pi^2} \sum_{k=0}^{n_\mathrm{pv}} \frac{c_k}{\sqrt{\mathbf{k}^2 + m_k^2}} \\ &= \int \frac{\mathbf{k}^2 d|\mathbf{k}|}{2\pi^2} \left(\frac{1}{\sqrt{\mathbf{k}^2 + m_0^{*2}}} + \sum_{k=1}^{n_\mathrm{pv}} \frac{c_k}{\sqrt{\mathbf{k}^2 + m_k^2}} \right) \,, \end{aligned} \tag{2.46}$$

where $m_0 = m_0^*$ and $c_0 = 1$ from the r.h.s. of (2.45). These remaining constants have yet to be determined but their purpose is to render the integral finite. The standard procedure [26] is to only include one cut-off λ which then appears in the expression for the masses m_k

$$m_k^2 = m_0^{*2} + \alpha_k \lambda^2. \tag{2.47}$$

with $c_0 = 1$ and $\alpha_0 = 0$. In the limit $|\mathbf{k}| \to \infty$ the integrand of (2.46) can be evaluated by taylor series

$$\begin{aligned} &\sum_{k=0}^{n_{\text{pv}}} \frac{c_k}{\sqrt{\mathbf{k}^2 + m_k^2}} \\ =&\frac{1}{|\mathbf{k}|}\left[\sum_{k=0}^{n_{\text{pv}}} c_k - \frac{1}{2}\frac{m_0^{*2}\sum_{k=0}^{n_{\text{pv}}} c_k + \lambda^2 \sum_{k=0}^{n_{\text{pv}}} \alpha_k c_k}{|\mathbf{k}|^2} + \mathcal{O}(|\mathbf{k}|^{-4})\right] . \end{aligned} \tag{2.48}$$

This decomposition proves that only the first two terms in (2.48) are divergent when integrated over. To circumvent this obstacle and eliminate these two terms we impose two conditions on the auxiliary masses m_k and therefore obtain

$$1 + \sum_{k=1}^{n_{\text{pv}}} c_k = 0 \tag{2.49}$$

$$\sum_{k=1}^{n_{\text{pv}}} a_k c_k = 0 \, . \tag{2.50}$$

The resulting integrand is then of order $\mathcal{O}(|\mathbf{k}|^{-3})$ and therefore superficially convergent. The choice of the number of Pauli-Villars fermions is still arbitrary but one is of course interested in keeping this number low. Note, that for $n_{\text{pv}} = 1$ the corresponding α_1 becomes trivial and $m_k = m_0 = m_0^*$ degenerate. Thus, the minimal choice is $n_{\text{pv}} = 2$ but their solutions are not unique. One popular option is $c_1 = 1$, $c_2 = -2$ where $\alpha_1 = 2$, $\alpha_2 = 1$ [26]. Lastly, we transform away the four-fermion interaction with the resultant effective action

$$S_{\text{eff}}[\sigma] = n\left\{\int \mathrm{d}^4x \, 2g\sigma^2 - \log\det q^\dagger q\right\} \tag{2.51}$$

and its matching enhanced Dirac operator Q in four euclidean space-time dimensions

$$Q = \not{\partial} + \gamma_0\mu + \sigma \, . \tag{2.52}$$

Now the renormalisation scheme is fully determined up to the parameters g and λ. Both constants are fixed by demanding that a certain effective mass m_0^* is realised. We will comment on this in sec. 2.2.3. With these tools one can then proceed to solve the gap equation.

2.2 NJL models

Finally, we dedicate the remainder of the chapter to the extremely successful phenomenological quark-meson model developed by Nambu and Jona-Lasinio (NJL) [4]. the model includes chiral symmetry breaking and again a four fermion interaction as for the GN models. For three dimensions, similar to the GN_4 model, we have to deal with the non-renormalisabiliy of this interaction term such that results depend on the choice of the ultraviolet (UV) cut-off. However, the phase diagram should not depend on the specific choice of λ unless the latter is very close to $\mathcal{O}(T_c)$ or $\mathcal{O}(\mu_c)$.

2.2.1 Two flavour NJL$_2$ model

In principle, one would have to take into account all six quark flavours when probing the phase boundary of QCD. Their masses extend over a wide range which for a given μ threshold permits to neglect those quark flavours of exceeding mass. Naturally, only the two lightest quark flavours $N_\mathrm{f} = 2$ are of interest when considering real world baryon densities.

In this context, another extension, the NJL model in (1+1) dimensions (NJL$_2$), involves the same pseudoscalar structure as the χGN (cf. sec. 2.1.3) with the exception of further pion combinations. In addition the model shows two flavours $f = 1, 2$

$$\mathcal{L}_{\mathrm{NJL}_2} = \sum_{f=1}^{2} \bar{\psi}_f^a \not{\partial}\, \psi_f^a - \frac{g^2}{2} \sum_{f=1}^{2} \left[\left(\bar{\psi}_f^a \psi_f^a\right)^2 + \left(\bar{\psi}_f^a \boldsymbol{\tau} i\gamma_5 \psi_f^a\right)^2 \right] , \tag{2.53}$$

each bearing a $N = N_\mathrm{c}$ colour degeneracy. Chiral symmetry is realised as in $(3+1)d$ GN model for $N_\mathrm{f} = 2$ isospin degrees of freedom in eq. (2.40). The matrices $\boldsymbol{\tau}^j$ with $j = 1, 2, 3$ act on the N_f-dimensional isospin space. The effective action using λ from eq. (2.21) assumes the form

$$S_\mathrm{eff}[\sigma, \boldsymbol{\pi}] = n \left\{ \int \mathrm{d}x\, d\tau\, \frac{1}{2\lambda} \left(\sigma^2 + \sum_{j=1}^{3} \pi_j^2 \right) - \frac{1}{2} \log\det Q^\dagger Q \right\} , \tag{2.54}$$

with the corresponding Q-operator

$$Q = \not{\partial} + \gamma_0 \mu + \sigma + i\gamma_5 \sum_{j=1}^{3} \tau_j \pi_j \, . \tag{2.55}$$

In the following section we will see that the NJL$_2$ model is the two-dimensional equivalent to another model.

2.2.2 Two flavour NJL$_4$ model

In $(3 + 1)$ dimensions the euclidean Lagrangian of the NJL model (NJL$_4$) is basically equivalent to the aforementioned $(1 + 1)d$ case with two flavours (2.53)

$$\mathcal{L}_{\mathrm{NJL}_4} = \sum_{f=1}^{2} \bar{\psi}_f^a \not{\partial}\, \psi_f^a - g \sum_{f=1}^{2} \left[\left(\bar{\psi}_f^a \psi_f^a\right)^2 + \left(\bar{\psi}_f^a \boldsymbol{\tau} i\gamma_5 \psi_f^a\right)^2 \right] , \tag{2.56}$$

except for the four-component two-flavour spinors and the redefinition of the coupling constant g in (2.38). Symmetries of the model are coinciding with the NJL$_2$ and GN$_4$ models (2.40), respectively. Also the Lagrangian yields a quadratically divergent integral contributions as in eq. (2.45). This obstacle is tackled in the same way as for the GN$_4$ model using the Pauli-Villars renormalisation scheme for $N_\mathrm{f} = 2$. The corresponding γ matrices in four euclidean space-time dimensions are given by

$$\gamma_0 = \begin{bmatrix} \mathbf{I}_2 & 0 \\ 0 & \mathbf{I}_2 \end{bmatrix} , \quad \gamma_i = \begin{bmatrix} 0 & \sigma_i \\ -\sigma_i & 0 \end{bmatrix} , \tag{2.57}$$

in addition to the euclidean correspondent $\gamma_5 = \gamma_0\gamma_1\gamma_2\gamma_3$. We emphasise, that the NJL model reduces to the corresponding two flavour GN model when assuming that only the chiral condensate σ condenses and pion-like field combinations $\bar{\psi}_f^a \boldsymbol{\tau} i\gamma_5 \psi_f^a$ are omitted.
following the transformations previously applied for the GN$_2$ and NJL$_2$ models we obtain an effective action after trading the quartic interaction terms for bosonic auxiliary fields.

For the NJL model in $(3+1)d$ that bears the same structure with log-determinant as before

$$S_{\text{eff}}[\sigma] = N \left\{ \int \mathrm{d}^4x \, 2g\sigma^2 - \log\det Q^\dagger Q \right\} \ . \tag{2.58}$$

And the Dirac operator Q in (2.55) adapted to four euclidean space-time dimensions.

2.2.3 Choice of parameters

As mentioned earlier, after regularisation we are left with two parameters, namely the coupling g and the cut-off λ. These have to match with the physical quantity of the theory - the pion-decay constant f_π. The latter has been measured from the decay $\pi^- \to \mu^- + \nu_\mu$ and amounts to $f_\pi = 88\text{MeV}$ [27]. Furthermore, we demand that after fixing m_0^* the pion-decay constant f_π is consistent with the cut-off λ. In the Pauli-Villars regularisation this can be calculated following [24]

$$f_\pi^2 = -\frac{N_\text{c} m_0^{*2}}{4\pi^2} \sum_{k=0}^{n_\text{pv}} c_k \log\left(\frac{m_k^2}{m_0^{*2}}\right) \ , \tag{2.59}$$

with $N_\text{c} = 3$ as in QCD. The only remaining parameter is the coupling constant g which we then infer by solving the gap equation (2.44). As usual the whole calculation is done in the chiral limit where any bare quark mass is set to zero.

This concludes the survey on continuum quark-based effective QCD models. We are now equipped with sufficiently many tools to solve the arising gap equations and handle finite density and temperature calculations. Also, we need to leave the continuum description behind and focus on finitely many degrees of freedom in the fermion fields and condensate.

Chapter 3

Fermions in the Pseudoparticle Approach

As we shall see, effective QCD models have served as the foundation when conducting and implementing an unbiased numerical study. However, the goal is to leave behind the continuum description and keep a limited amount of degrees of freedom. One obvious choice is the reformulation of the theory on the lattice. This will suffice as a first approach in Ch. 4 dedicated to regularisation schemes for the $(1+1)d$ GN model.
The salient point of this chapter is the question if there are other methods than just simple space discretisation to reduce these degrees of freedom. To this end, we introduce the *pseudoparticle approach* as the fundamental framework on which we will build our analysis. Its applications have been studied rigorously for bosonic cases like SU(2) Yang-Mills theory [28, 29, 14] such that also an adaption to fermion fields was proposed by [30].

3.1 Pseudoparticle Basics

Starting from the path integral formalism, the defining principle of the pseudoparticle approach is to numerically approximate fermion fields in (2.1) as a linear superposition of finitely many pseudoparticles. Any other field configurations that cannot be represented by this ansatz are disregarded.
In contrast to only spatially localised particles, pseudoparticles exhibit both space and time localisation. The number of building blocks is then fixed through the aforementioned decomposition

$$\psi(x) = \sum_j \underbrace{\eta_j G_j(x)}_{j\text{-th pseudoparticle}} \quad . \tag{3.1}$$

Here we employed Grassmann spinors and pseudoparticle functions G_j which have finite support in the space-time domain. The final step to translate the path integral (2.1) into its pseudoparticle equivalent is to modify the measure. Thus, the integration over field configurations is now restated by only considering pseudoparticle degrees of freedom such that the fermionic measure becomes

$$\int \mathcal{D}\bar{\psi}\mathcal{D}\psi \cdots = \int \left(\prod_j d\bar{\eta}_j d\eta_j \right) \ldots \tag{3.2}$$

The relation between ψ and η_j is linear and invertible (3.1) such that the appearing Jacobian after a change of coordinates is merely an irrelevant constant $\left|\frac{\partial\psi}{\partial\eta_j}\right| = \text{const}$. In the best case this constant is equal to 1 because of the localisation and orthogonality of the G_j such that only diagonal elements contribute to the determinant. As a first approach, we

elaborate on properties of pseudoparticle functions and how to convert previously defined continuum effective actions (cf. Ch. 2) into the pseudoparticle formalism.
For generalisation, we will consider $(d+1)$ space-time dimensions keeping the spatial dimensionality d arbitrary for now. In subsequent investigations we will specifically inspect for situations of $d \in \{1, 3\}$. From now on the theories will be restricted to a box of temporal extent L_0 and correspondingly spatial volume of $(L_1)^d$ with periodic or anti-periodic spatial boundary conditions. From [31] we know that fermions are actually anti-periodic in time with period $\beta = 1/T \propto 1/L_0$ which then affects the nature of the pseudoparticle functions at the temporal boundary

$$G_j(x_0 + L_0, \mathbf{x}) = -G_j(x_0, \mathbf{x}). \tag{3.3}$$

The effective action for all the theories introduced in Ch. 2 shows the same structure including a bilinear fermion term and a bosonic scalar/pseudoscalar field ϕ as introduced in (2.1) with its partition function $\mathcal{Z}$

$$S[\bar{\psi}, \psi, \phi] = \int d^{d+1}x \, \left(\bar{\psi} Q(\phi) \psi + \mathcal{L}(\phi)\right). \tag{3.4}$$

Recall that for the special case of the chirally discrete GN_2 model the integration over fermions was done explicitly for an effective action (cf. Sec. 2.1.1)

$$S_{\text{eff}}[\phi] = \int d^{d+1}x \, \mathcal{L}(\phi) - \log(\det \langle G_j | Q | G_{j'} \rangle). \tag{3.5}$$

The matrix $\langle G_j | Q | G_{j'} \rangle$ is subject to the choice of the finite pseudoparticle basis and is thus finite itself. In order to illustrate this, one classical example of G_j are eigenfunctions of the Dirac operator Q. Principally, these are a set of plane waves which we will discuss further in Sec. 4.3.
We aim to find a functional basis in order to reconstruct both fermion fields as well the condensate(s). For this reason, we need to be able to model exactly the whole Hilbert space $\mathcal{H}$ of $L^2(\mathbb{R})$, with inner product

$$\langle f, g \rangle = \int_{\mathbb{R}} dx \, f(x) \overline{g(x)} \, . \tag{3.6}$$

Before we explicitly consider basis candidates we motivate a different regularisation procedure. Recall that we briefly mentioned this when retrieving the effective action in Eq. (2.14). There we suggested a change $(\det Q)^2 = \det Q^\dagger Q$ provided that $\det Q \geq 0$ which was proven in Rem. 2.1 for enhanced Dirac Q operators of the form $Q(\phi) = \not{\partial} + \phi$. As previously argued this modification has important implications in the pseudoparticle approach and is highly advantageous over the naive effective action (3.5).

3.1.1 $Q^\dagger Q$-Pseudoparticle-Regularisation

So far it has not gone unnoticed that the naive Q-type approach poses an immediate problem. To make this issue more apparent we let the Dirac operator Q act on the pseudoparticle basis functions $G_{j'}$. Clearly this operation violates closure by permitting functions outside the initial pseudoparticle function space $\mathrm{span}\{G_n\}$, specifically

$$G_j(x) = \sum_k a_{j,k} G_k(x) + h_j H_j(x) \quad \text{with} \quad \langle G_k, H_j \rangle = 0 \quad \forall j, k \, . \tag{3.7}$$

When calculating matrix elements in the fermion matrix the effect of this decomposition becomes critical as soon as the second part in (3.7) dominates (ii) the sum over G_k i.e.

(i) $|\sum_k a_{j,k} G_k(x)| \gg |h_j|$

(ii) $|\sum_k a_{j,k} G_k(x)| \lesssim |h_j|$

In other words, a substantial part of QG_j namely $h_j H_j$ is neglected due to $H_j \perp \text{span}\{G_n\}$. This reasoning becomes even more evident when diagonalising the fermion matrix

$$U^\dagger_{j,k} \langle G_k|Q|G_{k'}\rangle U_{k',j'} = \langle \tilde{G}_j|Q|\tilde{G}_{j'}\rangle = \text{diag}(\mu_1, \mu_2, \dots)_{j,j'}. \tag{3.8}$$

Under these conditions Eq. (3.7) simplifies

$$Q\tilde{G}_j(x) = \mu_j \tilde{G}_j(x) + h_j H_j(x). \tag{3.9}$$

This yields a problematic scenario in the limit $\exists j\, |\mu_j = 0$ and $h_j \neq 0$. By missing out on the perpendicular part on the right-hand side of (3.9), $\tilde{G}_j$ suddenly becomes a zero mode of Q yielding a zero determinant

$$\det \langle G_k|Q|G_{k'}\rangle = \prod_j \mu_j \tag{3.10}$$

which due to $\log(0) = -\infty$ produces a diverging effective action (3.5). The existence of such unphysical zero modes is not a unique property of a specific pseudoparticle candidate. To demonstrate this let us first leave the continuum and move to box sizes of integer values $L \in \mathbb{N}$. To this end we analyse anti-periodic functions built from pseudoparticle functions F_j with integer support

$$G_j(x) = F(x-j) - F(x-j+L)\,. \tag{3.11}$$

The pseudoparticles F_j are supposed to be real $F = F^*$ and confined to the computational domain $[0, L-1]$ such that $F = 0$ when $x \leq 0$ and $x \geq L$. Conversely resulting anti-periodic pseudoparticles G_j also have integer support within the interval $[0, L-1]$. Furthermore, the G_j are then uniformly translated on L with $j = 0, \dots, L-1$. Together with locality and uniformity certain linear combinations of G_j which are real by definition, will exhibit unphysical zero modes for odd valued box lengths L. This corresponds to an odd number of elements in j. This becomes obvious when looking at a sum over $\text{span}\{G_n\}$ with alternating sign i.e. for $a_{j,k} = (-1)^j$ in the first part of (3.7)

$$\tilde{G}_{\text{zero mode}}(x) = \sum_{j=0}^{L-1} (-1)^j G_j(x). \tag{3.12}$$

However, the proposed $Q^\dagger Q$ regularisation remedies this complication. Now both sides of $\langle G_j|Q^\dagger Q|G_{j'}\rangle$ are outside of $\text{span}\{G_n\}$. But their overlap is part of a different space, namely $\text{span}\{QG_n\}$. Therefore, the naive regularisation (3.5) is traded for a type of effective action that we will use for the upcoming parts of the thesis

$$S_{\text{eff}}[\phi] = \int d^{d+1}x\, \mathcal{L}(\phi) - \frac{1}{2} \log(\det \left\langle G_j|Q^\dagger Q|G_{j'}\right\rangle). \tag{3.13}$$

In the next section we will examine how sensitive possible pseudoparticle candidates are to the type of regularisation (Q or $Q^\dagger Q$). We address this issue by considering a spatially dependent Dirac operator.

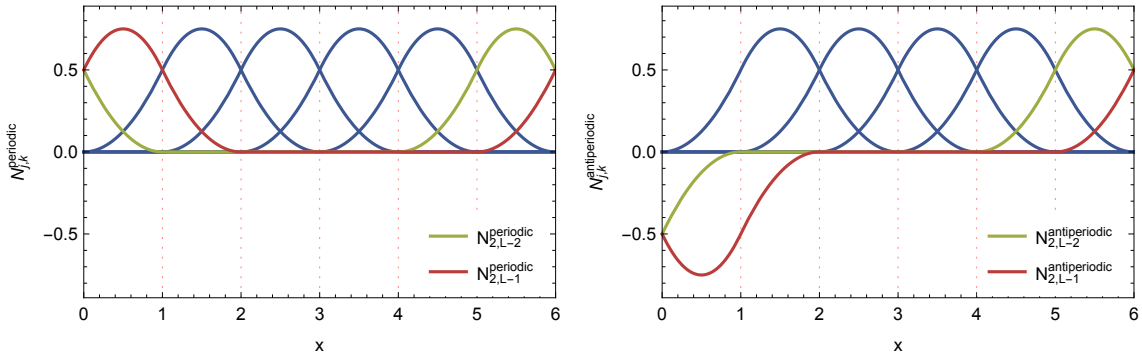

Fig. 3.1: $L = 6$. (a) Periodic B-spline basis functions of degree $j = 2$. (b) Anti-periodic B-spline basis functions of degree $j = 2$. The blue curves correspond to basis function with full support within the computational domain $[0, L-1]$.

3.2 B-Splines

We define the basis functions for B-splines of degree k by joining several polynomial pieces of degree j with at most $\mathcal{C}^{j-1}$ continuity. Correspondingly a so-called *knot* vector $\mathbf{T} = (t_0, t_1, \ldots, t_m)$ or more explicitly a set of non-descending breaking points $t_0 \leq t_1 \leq \cdots \leq t_m$ subdivides the domain into regions labelled by k [32]

$$N_{0,k} = \begin{cases} 1 & \text{if } t_k \leq x < t_{k+1} \\ 0 & \text{otherwise} \end{cases} \tag{3.14}$$

$$N_{j,k}(x) = \frac{x - t_k}{t_{k+j} - t_k} N_{j-1,k}(x) + \frac{t_{k+j+1} - x}{t_{k+j+1} - t_{k+1}} N_{j-1,k+1}(x) \,, \tag{3.15}$$

where the knot vector $\mathbf{T}$ is split uniformly such that

$$t_k = k \frac{L}{m}. \tag{3.16}$$

Here m is the number of subdivided intervals of L. This also makes the reference to *knots* clearer as the values of (3.16) *tie together* the polynomials. Both periodic and anti-periodic B-spline basis functions amount to

$$N^{\text{antiperiodic}}_{j,k}(x) = N_{j,k}(x) - N_{j,k-L}(x) \,, \tag{3.17}$$

$$N^{\text{periodic}}_{j,k}(x) = N_{j,k}(x) + N_{j,k-L}(x) \,, \tag{3.18}$$

as motivated by (3.11) and shown in Fig. 3.1. It will prove very beneficial that B-spline basis functions have finite support. In other words, it is only non-zero on a few adjacent subintervals such that the basis functions are quite localised in space[-time].
Remember, that we want to approximate fermionic fields and the chiral condensate. Already low degrees k should then be able to encompass not too heavily oscillating field configurations. With the first derivative in $Q^\dagger Q$ in Eq. (3.13) the minimal order of continuous differentiation is $\mathcal{C}^1$. Hence, the degree of the B-spline basis is at least $j = 2$ which will be used for our study.
In the explicit case for $j = 2$, basis functions consist only of three parabolic pieces of neighbouring subintervals giving rise to a total space[-time] volume of $V = 3^d$.
Considering the piecewise polynomial form of (3.14) consecutively the derivative remains analytical consisting only of B-spline basis functions of degree $j - 1$. This is tantamount to differentiating (3.14) and inductively proving the claim (cf. Sec. B.1)

$$\partial_x N_{j,k}(x) = \frac{j}{t_{k+j} - t_k} N_{j-1,k}(x) - \frac{j}{t_{k+j+1} - t_{k+1}} N_{j-1,k+1}(x) \,. \tag{3.19}$$

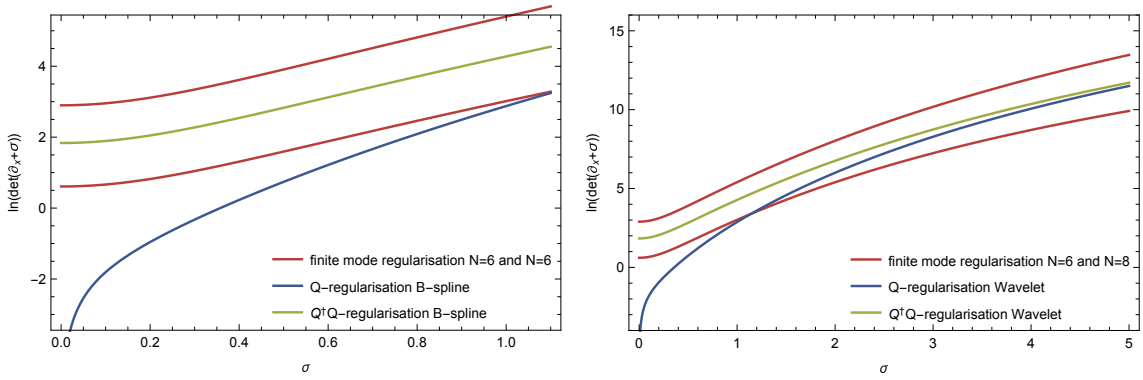

Fig. 3.2: $L = 7$. $\log\det(\partial_x + \sigma)$ as function of σ based on finite mode regularisation, Q-regularisation and $Q^\dagger Q$-regularisation for both *(a)* B-Splines and *(b)* D_3 Wavelets.

Hence, we obtain closure under $Q^\dagger Q$ which is in agreement with the account of Sec. 3.1.1. Returning to the discussion on how the regularisation influences the computation of the functional determinant we consider a simple example: the anti-Hermitian operator ∂_x on the interval $0 \leq x \leq L$. With plane wave and B-spline basis functions of degree $j = 2$

$$G_k(x) = N_{2,k}^{\text{antiperiodic}}(x), \tag{3.20}$$

for $k = 0, \ldots, L-1$ and $L = 7$. We inspect the function

$$\log\det(\partial_x + \sigma), \tag{3.21}$$

in the $Q^\dagger Q$ and Q regularisation scheme. Furthermore, the B-spline basis functions (3.19) are orthonormalised using Gram-Schmidt-Orthonormalisation. The resulting σ dependence is illustrated in Fig. 3.2 (a). The behaviour of the $Q^\dagger Q$ regularisation by plane waves and by B-splines is very similar and dependent on the amount of degrees of freedom. Both the plane wave solutions are for $N = 8$ and $N = 6$ lowest lying eigenmodes w.r.t. the momenta in (4.16). For the B-splines we had $N = 7$ orthonormal basis functions which explains the position of the curve in between. In contrast, the Q-regularised (blue) B-splines display a distinct pattern. On the one hand, it approaches the $N = 7$ solution from below at large σ because high values σ will eventually start dominating the fermion matrix diagonal. On the other hand, it shows a pole at $\sigma = 0$ due to unphysical zero-modes as discussed in Sec. 3.1.1.

The basis functions should also be *refinable* which means to express any $N_{j,k}$ as a linear combination of B-splines of finer knots at smaller scales using translations k'

$$N_{j,k} \to \sum_{k'} d_{j,k'} B_{j,k'}, \tag{3.22}$$

by adding more and more details at fixed degree j. The usage of this refinement equation would eventually lead to the possibility to reconstruct the whole $L^2(\mathbb{R})$. However, even after normalisation the spaces spanned by finer $B_{j,k}$ are not orthogonal among themselves nor the initial scale functions $N_{j,k}$. Nevertheless, this would be a favourable feature for numerical implementations regarding the fermion determinant. In the subsequent section we present a family of functional bases that circumvent this obstacle.

3.3 Wavelets

With the intention of migrating to higher dimensions and the necessity of gaining efficiency for the search of *kink solutions* in the crystal phase, we want to determine a smaller number

of physically important fermionic field configurations. In order to achieve this task using spatially localised functions as for B-Splines we propose a different kind of basis functions namely *Wavelets*. Localised means that the wavelet enjoys compact support or that its amplitude decays at least exponentially outside a given interval. Contrary to a plane wave expansion, the pivotal motivation for working with wavelets as pseudoparticles are their potential to capture both spatial and scale (momentum) information w.r.t. the function of interest.
In the upcoming sections we focus intensively on the discrete wavelet family constructed by Daubechies and set our notation. For a more comprehensive survey see [33].

3.3.1 Daubechies Wavelets

Compared to other possible candidates Daubechies wavelets assert a number of vanishing moments $\mathcal{N} = 2g$ equivalent to the wavelet system denoted by $\mathcal{W} = D_g$. Where g is a positive integer called the *wavelet genus* and describes how accurately a function is encoded through the corresponding wavelet basis. In the following context

$$\int_{\mathbb{R}} \psi(x) x^p \, dx = 0 \tag{3.23}$$

for $p \in \{0, \ldots, \mathcal{N}-1\}$, a function $\psi(x)$, the wavelet "mother" function, is supported on the interval $\operatorname{supp} \psi = [0, \mathcal{N}-1]$. As we will derive below the system D_g is fully defined by ψ and another function ϕ, the father scaling function with the same $\operatorname{supp} \psi = \operatorname{supp} \phi = [0, \mathcal{N}-1]$. This implies that the supports of their n-th derivatives $\psi^{(n)}$ and $\phi^{(n)}$ coincide, meaning $\operatorname{supp} \psi^{(n)} = \operatorname{supp} \phi^{(n)} \subseteq [0, \mathcal{N}-1]$.
Up to a certain scale it is then sufficient to express every function via wavelet functions (mother wavelet) $\psi_{j,k}$ and scaling functions (father wavelet) $\phi_{j,k}$. We will discuss this in the ensuing paragraph. For the remainder when talking about *scale*, the parameter $j \in \mathbb{Z}$ will encode information regarding higher scale at large j as well as lower scale at small j. In analogy to the plane wave formalism (cf. Sec. 4.3) the scale j directly corresponds to momentum and is inversely proportional to distance at resolution 2^{-j}.

3.3.2 Multiresolution Analysis

Following closely the account in [33] we start with the space $L^2(\Omega)$ of all square integrable functions on the domain $\Omega = \mathbb{R}$ meaning $\|f\|_{L^2}^2 < \infty$. Using a Multiresolution Analysis (MRA) an orthonormal basis thereof can be constructed from a progressing sequence of closed *scaling* subspaces $\{V_j\}_{j \in \mathbb{Z}}$ in order to approximate $L^2(\mathbb{R})$ and a function ϕ satisfying orthonormality conditions. In other words, the procedure depends on a clever choice of the scaling function ϕ, such that it satisfies some continuity, smoothness and tail requirements. But, most importantly, the family

$$\{\mathcal{T}^k \phi(x) \equiv \phi_k(x)\}_{k \in \mathbb{Z}} \tag{3.24}$$

constitutes an orthonormal basis for the reference space V_0 [15] from a single function ϕ using only discrete unitary translations $\mathcal{T}$ and dilations $\mathcal{D}$ thereof. Both the discrete translation $\mathcal{T}$ and the dilation $\mathcal{D}$ operate on functions $f \in L^2(\mathbb{R})$ and are defined via

$$\mathcal{D} f(x) = \sqrt{a} f(ax) \, , \quad \mathcal{T} f(x) = f(x-b) \, . \tag{3.25}$$

In the case of acting on $f(x)$ multiple times, we have

$$\mathcal{T}^k f(x) = \overbrace{\mathcal{T} \circ \cdots \circ \mathcal{T}}^{\text{k-times}} f(x) = f(x - kb) \, . \tag{3.26}$$

We stress that the construction is valid for all rational dilation factors $a > 1$. In general $a = 2$ is the simplest option [34] together with $b = 1$. The latter choice is not very serious because for arbitrary b (3.25) can always be translated into itself such that it suffices to assume $b \neq 0$. This alters the definition of $\mathcal{D}$ in (3.25)

$$\mathcal{D}f(x) = \sqrt{2}f(2x), \quad \mathcal{T}f(x) = f(x-1)\ . \tag{3.27}$$

We apply the latter during the definition specifying the arguments from above. Note that the overline $\bar{\cdot}$ in the following denotes the closure of a set.

Definition 3.1 *The scaling spaces V_j are nested and describe consecutive approximations of $L^2(\mathbb{R})$*

$$\{0\} \subset \cdots \subset V_{-1} \subset V_0 \subset V_1 \subset \cdots \subset L^2(\mathbb{R}) \tag{3.28}$$

Thus, the space $L^2(\mathbb{R})$ is a closure of the union of all V_j. Conversely, the closure $\overline{\bigcup_{j\in\mathbb{Z}} V_j}$ is dense in $L^2(\mathbb{R})$ while $\bigcap_{j\in\mathbb{Z}} V_j = \{0\}$. Lastly, when scaled by a factor 2 functions move from scale V_j to V_{j+1} or

$$f \in V_j \Leftrightarrow \mathcal{D}f \in V_{j+1}$$

Remark 3.2 *With ϕ being an orthonormal basis for V_0 in* (3.24) *one condition is the normalisation in the L^2-norm*

$$\|\phi\|_{L^2} = \left(\int dx\, |\phi(x)|^2\right)^{\frac{1}{2}} = 1.$$

An additional requirement is the convenient choice of the unit area of ϕ [33]

$$\int dx\, \phi(x) = 1.$$

Additionally, one defines *detail* spaces W_m as the orthogonal complement of V_j in V_{j+1}

$$V_{j+1} = V_j \oplus W_j\ , \quad W_j \perp V_j\ , \tag{3.29}$$

with the orthogonal direct sum of Hilbert spaces. We consider the spaces V_1 and V_0 for a moment which will be beneficial to understand the difference between ψ and ϕ and the W_0 and V_0, respectively. Intuitively (3.27) and (3.28) tell us that V_1 is double the size as V_0. This is true because the latter is constructed from integer translations of $\phi_{0,0}$. However, on a bigger scale namely at V_1 the basis is generated by translation of two functions $\phi_{1,0}$ and $\phi_{1,1}$. A natural consequence would be to assume that W_0 which is the complement of V_0 in V_1 is then itself generated from a single function ψ alone.
For an arbitrary scale j and in the following discussion, we define the spaces spanned by $\{\phi_{j,k}\}_{k\in\mathbb{Z}}$ and $\{\psi_{j,k}\}_{k\in\mathbb{Z}}$ over the translation parameter k and scale parameter j by closures V_j and W_j

$$V_j = \overline{\text{span}\{\phi_{j,k}\}_{k\in\mathbb{Z}}}, \tag{3.30}$$

$$W_j = \overline{\text{span}\{\psi_{j,k}\}_{k\in\mathbb{Z}}}. \tag{3.31}$$

The orthonormal bases $\{\psi_{j,k}\}_{k\in\mathbb{Z}}$ and $\{\phi_{j,k}\}_{k\in\mathbb{Z}}$ are written utilising the properties in Def. 3.1 and the adequate dilation and translation operations (3.27)

$$\psi_{j,k}(x) = (\mathcal{D}^j\mathcal{T}^k\psi)(x) = 2^{\frac{j}{2}}\psi(2^j x - k)\ , \tag{3.32}$$

$$\phi_{j,k}(x) = (\mathcal{D}^j\mathcal{T}^k\phi)(x) = 2^{\frac{j}{2}}\phi(2^j x - k)\ . \tag{3.33}$$

Before commencing an attempt to use wavelets in an expansion to reconstruct fermionic fields in the pseudoparticle approach, we retrieve some orthogonality conditions. On the account of Eqs. (3.29) and (3.24) clearly $\psi_{j,k} \in W_j$ is orthogonal to $\phi_{j,k} \in V_j$. Furthermore, all the W_j are orthogonal among themselves which effectively means that

$$\langle \phi_{j,k}, \phi_{j',k'} \rangle = \delta_{k,k'}, \tag{3.34}$$
$$\langle \psi_{j,k}, \psi_{j',k'} \rangle = \delta_{j,j'}\delta_{k,k'}, \tag{3.35}$$
$$\langle \phi_{j,k}, \psi_{j',k'} \rangle = 0 \qquad \text{for} \quad j' \geq j \; . \tag{3.36}$$

Notably in the first relation (3.34), we can see that different scales do not affect each other due to the missing $\delta_{j,j'}$. In summary, we assembled most basic features of Daubechies wavelets that will help us to construct the Hilbert space. These orthonormality conditions already reinforce the argument in (3.22) where off-diagonal elements in e.g. the fermion matrix are equal to zero.

3.3.3 Wavelet Expansion

Having outlined how to set up an orthogonal succession of "detail" W_j and "scaling" spaces V_j, a logical conclusion from (3.28) and (3.29) would be

$$L^2(\mathbb{R}) = V_\infty = V_{j_0} \oplus W_{j_0} \oplus W_{j_0+1} \oplus W_{j_0+2} \oplus \dots \tag{3.37}$$
$$= V_{j_0} \oplus \sum_{j \geq j_0} W_j = \bigoplus_{j \in \mathbb{Z}} W_j \; , \tag{3.38}$$

for the full Hilbert space $L^2(\mathbb{R})$. Assuming that approximation is good enough at a scale $j = n$ we use this fixed cut-off to find the isomorphism

$$V_{j_0} \oplus_{j=0}^{n-1} W_j \simeq V_n, \tag{3.39}$$

These properties (3.37) and (3.39) ensure the possibility to decompose every function $f(x) \in L^2(\mathbb{R})$ as a linear superposition of "scaling" basis functions $\{\phi_{j,k}(x)\}_k$ of V_j and "wavelet" basis functions $\{\psi_{j,k}(x)\}_{j \geq j_0,k}$ of W_j

$$f(x) = \sum_k c_{j_0,k}\phi_{j_0,k}(x) + \sum_{j=j_0}^{\infty}\sum_k d_{j,k}\psi_{j,k}(x) \; . \tag{3.40}$$

The number $\mathcal{N} = 2g$ of vanishing moments (3.23) of the "mother" wavelet $\psi_{0,0}$ eventually determines the accuracy of approximation. Strictly speaking the higher the genus g the better any function of the Hilbert space will be reproduced. Now, if P_n and Q_n induce orthogonal projections of $L^2(\mathbb{R})$ onto V_n and W_n respectively it follows that $P_{n+1} = P_n + Q_n$ for an arbitrary function $f(x) \in L^2(\mathbb{R})$. In this context we discriminate between a coarse *approximation coefficient*

$$c_{j_0,k} = \langle \phi_{j_0,k}, f \rangle = \int_{\mathbb{R}} \phi_{j_0,k}(x) f(x)\, dx \tag{3.41}$$

and a *detail coefficient*

$$d_{j_0,k} = \langle \psi_{j,k}, f \rangle = \int_{\mathbb{R}} \psi_{j,k}(x) f(x)\, dx \; . \tag{3.42}$$

For explanatory reasons we narrowed the discussion to one dimension. However, an extension of the MRA in higher dimensions was already proposed in [35] and will be needed

when advancing to QCD. Hence, we restrict ourselves to the description of scaling functions only and define

$$\mathbf{V}_j = V_j \oplus V_j \ . \tag{3.43}$$

Scaling functions simply factorise and the union of all $\mathbf{V}_j$ is again equivalent to $L^2(\mathbb{R}^2)$ which gives similarly to Eq. (3.30)

$$\mathbf{V}_j = \overline{\text{span}\{\Phi_{j,k}\}_{k\in\mathbb{Z}^2}}. \tag{3.44}$$

The scaling functions $\Phi_{j,k}$ obey the same pattern as for the one-dimensional case

$$\Phi_{j,k}(x_1,x_2) = 2^j\Phi(2^m x_1 - k_1, 2^j x_2 - k_2), \tag{3.45}$$

$$= \phi_{j,k_1}(x_1)\phi_{j,k_2}(x_2) \ , \tag{3.46}$$

with $k_1, k_2 \in \mathbb{Z}$, $k = (k_1, k_2)$ and $\text{supp}\,\Phi = [0, \mathcal{N}-1] \times [0, \mathcal{N}-1]$. The purpose of the two terms in (3.40) is (i) an approximation at the scale j_0 as well as (ii) a sum over details in the respective function spaces W_j using corresponding wavelet functions of increasing higher scales. It remains to mention that scaling functions ϕ themselves are uniquely defined as a superposition of shifted ϕ at the same scale which we will derive now. The parameters $\{a_k\}$ in this sum are the wavelet *filter* coefficients $\{a_k\} \in l^2(\mathbb{Z})$. As a side comment, I note here that other literature favours wavelet coefficients with the property $\sqrt{2}a_k = h_k$. Along the course of this thesis we refer to [36] being used to determine accurately with double precision accuracy the Daubechies filter coefficients.
Since $V_j \subset V_{j+1}$, any function in V_j can be expanded in terms of basis functions of V_{j+1}. In particular, $\phi_{j,0}(x) \in V_j$ are all of the same scale j. Exclusively for $j = 0$ we use $\phi(x) = \phi_{0,0} \in V_0$

$$\phi(x) = \sum_{k\in\mathbb{Z}} a_k \phi_{1,k}(x) = \sqrt{2}\sum_{k\in\mathbb{Z}} a_k \phi(2x-k) \ . \tag{3.47}$$

Especially, compactly supported Daubechies "father" scaling functions ϕ only have a finite number of nonzero a_k. These basis functions ϕ are constructed from a single function and satisfy the linear renormalisation group equation known as the recursive *dilation equation*

$$\phi(x) = \sqrt{2}\sum_{k=0}^{\mathcal{N}-1} a_k \phi(2x-k) = \mathcal{D}\left[\sum_{k=0}^{\mathcal{N}-1} a_k \mathcal{T}^k \phi(x)\right] \ . \tag{3.48}$$

In Eq. (3.48) the scaling function $\phi(x)$ first undergoes block averaging i.e. translations $\mathcal{T}^k$ weighted with the coefficients a_k. The resultant expression is rescaled with $\mathcal{D}$ where $\phi(x)$ is now a fixed point. Remark 3.2 can then be interpreted as a scale fixing condition. This makes Daubechies wavelets a natural basis for renormalisation group transformations and explains also their popularity in Field Theories. Equation (3.48) also clarifies why a higher wavelet genus g yields higher computational expenses – every block average will just involve more translations k (recall $\mathcal{N} = 2g$ in (3.48)).
The aforementioned orthonormality and support of ϕ in Rem. 3.2 also bound the summation when integrating both sides of the dilation equation (3.48) with $2x \mapsto x$ yielding the algebraic equation

$$\sum_{k=0}^{\mathcal{N}-1} a_k = \sqrt{2} \ . \tag{3.49}$$

Consequently, we can backtrack and specify the condition (3.23) for $\mathcal{N}$ vanishing moments a bit further by realising that the scaling function describes any polynomial up to degree $\mathcal{N}-1$ exactly. This signifies for the monomials $\{x^p\}$ that

$$\sum_{k\in\mathbb{Z}} M_k^p \phi_k(x) = x^p \ . \tag{3.50}$$

One can immediately derive the effect on the wavelets by integration over $\mathbb{R}$ and multiplication with $\psi(x)$

$$\sum_{k\in\mathbb{Z}} M_k^p \int_{\mathbb{R}} \phi_k(x)\psi(x) = \int_{\mathbb{R}} x^p \psi(x). \tag{3.51}$$

At last we exploit orthogonality $\langle \phi, \psi \rangle = 0$ and obtain the desired vanishing moment relation $\langle x^p, \psi \rangle = 0$.

3.3.4 Wavelet Calculus and Improper Connection Coefficients

Regarding subsequent calculations we emphasise that Daubechies wavelet scaling functions lack an expression in closed form. Their basis functions mostly exhibit a fractal structure. In other words, Daubechies wavelets families miss a classical prescription for differentiation. On our course of using wavelets as a candidate for the pseudoparticle approach, we need to compute the most important integrals occurring along the fermion matrix with $Q^\dagger Q$-regularisation. To dispose of this obstacle in the evaluation of derivative overlaps in matrix elements, one defines *improper* connection coefficients for a wavelet system $\mathcal{W}$ respecting the order of differentiation

$$\Lambda^{d_1,\ldots,d_n}_{k_1,\ldots,k_n} = \int_{\mathbb{R}} dx \prod_{l=1}^{n} \phi_{k_l}^{(d_l)}(x) = \left\langle \prod_{l=1}^{n} \phi_{k_l}^{(d_l)} \right\rangle \tag{3.52}$$

with the scale fixed at $\phi_k(x) \in V_0$ from now on. Here, the attribute *improper* refers to the fact that we are considering the whole $\mathbb{R}$ as our computational domain. If we choose finite box sizes which are smaller than the support of the utilised scaling functions ϕ one incurs a systematic error. We will resolve this issue in Sec. 3.3.5 employing so-called *proper* connection coefficients. Luckily those overlap integrals of basis functions and low-order derivatives can be carried out analytically using both the renormalisation group equation (3.48) and its scale fixing condition.

Regarding the matrix elements of Q, we need only bilinear connection coefficients up to first order in differentiation. To this end, we employ the algorithm proposed in approaches [37, 38] using the dilation equation (3.48) to reformulate the connection coefficients as a solution of a linear system. This procedure provides exact and explicit representations via rational coefficients.
Modifying the general expression (3.52) we demonstrate the ideas on two-term connection coefficients $\Lambda^{0,d}_{k,l}$ with $k, l = 0, \ldots, 2g-1$ adopting a Daubechies wavelet system D_g with genus g. The integral defined as

$$\Gamma_l^{d;k} := \langle \phi_k, \phi_l^{(d)} \rangle \,, \tag{3.53}$$

does not exist in a classical sense. Note that due to locality and integration by parts (3.52) only depends on the total degree of derivatives

$$d = \sum_l d_l. \tag{3.54}$$

For first order derivative connection coefficients $\Lambda^{1,0}_{k,l} = \Gamma_l^{1;k} = \Gamma_l^k$, we obtain

$$\Gamma_l^k := \left\langle \phi_k, \phi_l' \right\rangle \,, \tag{3.55}$$

To facilitate the discussion, we will exclusively refer to *fundamental* connection coefficients which are the non-recurring and non-zero values of Γ. These are the only non-zero coefficients obeying the overlap of both ϕ supports such that $\Gamma = \{\Gamma_l^0\}_{l=1}^{\mathcal{N}-2}$. Its skew symmetry and invariance under a global shift lead to

$$\Gamma_l^k = -\Gamma_k^l. \tag{3.56}$$

To reconstruct the whole fermion matrix, we have the necessity to continue with higher order connection coefficients in the scaling fields ϕ due the product of the two Dirac operators $Q^\dagger Q$ requiring second order bilinear and trilinear terms. Hence, we need the additional integrals of $\Lambda^{0,2}_{k,l} = \Gamma^{2;k}_l = \Omega^k_l$ and $\Lambda^{0,0,1}_{0,k,l} = \Upsilon^k_l$

$$\Omega^k_l := \left\langle \phi'_k, \phi'_l \right\rangle = -\left\langle \phi_k, \phi''_l \right\rangle \ , \tag{3.57}$$

$$\Upsilon^k_l := \left\langle \phi_k \phi_l, \phi' \right\rangle \ . \tag{3.58}$$

Also here the number of unique fundamental connection coefficients is subject to the symmetry induced by integration by parts

$$\Omega^k_l = \Omega^l_k \ , \tag{3.59}$$

$$\Upsilon^k_l = \Upsilon^l_k \ . \tag{3.60}$$

Given $\mathcal{N}$ vanishing moments (3.23) the d-th derivative of $\phi(x)$ can simply be decomposed into a superposition of dilated version of itself $\phi(x-k)$ with bilinear Γs from Eq. (3.53)

$$\phi^{(d)}_l = \sum_k \Gamma^{d;k}_l \phi_k(x) + \sum_{j,k} \Gamma^{d;j;k}_l \psi_{j,k}(x) \ . \tag{3.61}$$

Consequently, when taking the inner product with ϕ_k or $\psi_{j,k}$ only terms of identical scale j survive in the connection coefficients. This results from the orthogonality amongst them according to (3.34) - this renders Λ sparse.
For later purposes, we outline the technique by calculating fundamental two-factor connection coefficients $\Lambda^{d_1,d_2}_{0,l} = (-1)^{d_1}\Lambda^{0,d_1+d_2}_{0,l} = \Gamma^{d;0}_l$ taking the *dilation* equation to derive the identity

$$\phi_{j-1,l}(x) = 2^{\frac{j-1}{2}}\phi(2^{j-1}x - l) = \sum_{k=0}^{\mathcal{N}-1} a_k \phi_{j,2l+k}(x) \ . \tag{3.62}$$

Its d-th derivative at $j=1$ admits a relation to the scale at $j=0$ under the assumption that $\phi \in C^d(\mathbb{R})$

$$\phi^{(d)}_l(x) = \sum_{k=0}^{\mathcal{N}-1} a_k \phi^{(d)}_{1,2l+k}(x) = 2^d\sqrt{2}\sum_{k=0}^{\mathcal{N}-1} a_k \phi^{(d)}_{2l+k}(2x) \ . \tag{3.63}$$

Inserting this result together with the dilation equation into (3.53) we derive a recursion relation

$$\Gamma^{d;0}_l = \int_{\mathbb{R}} \left[\sqrt{2}\sum_{r=0}^{\mathcal{N}-1} a_r \phi_r(2x)\right]\left[2^d\sqrt{2}\sum_{s=0}^{\mathcal{N}-1} a_s \phi^{(d)}_{2l+s}(2x)\right] dx \ , \tag{3.64}$$

$$= 2^{d+1}\sum_{r=0}^{\mathcal{N}-1}\sum_{s=0}^{\mathcal{N}-1} a_r a_s \int_{\mathbb{R}} \phi_r(2x)\phi^{(d)}_{2l+s}(2x)\, dx \ , \tag{3.65}$$

$$= 2^d \sum_{r=0}^{\mathcal{N}-1}\sum_{s=0}^{\mathcal{N}-1} a_r a_s \int_{\mathbb{R}} \phi_r(x)\phi^{(d)}_{2l+s}(x)\, dx = 2^d \sum_{r=0}^{\mathcal{N}-1}\sum_{s=0}^{\mathcal{N}-1} a_r a_s \Gamma^{d;0}_{2l+s-r} \ . \tag{3.66}$$

These are called the *scaling equations* [15]. We know that $\mathbf{\Gamma}^d = \{\Gamma^{d;0}_n\}^{\mathcal{N}-2}_{n=2-\mathcal{N}}$ is a column vector of $(2\mathcal{N}-3)$ components and only non-zero around $n \in [2-\mathcal{N}, \mathcal{N}-2]$. Due to the overlap of supports of $\phi(x)$ and $\phi^{(d)}_l(x)$, we can simply act with the transformations $n = 2l+s-r$ or $s = n+r-2l$ with the summation bounds of $r \in [0, \mathcal{N}-1]$ still intact.

For limited r within $\max(0,p) \leq r \leq \min(\mathcal{N}-1, \mathcal{N}-1+p)$ one adequately substitutes $p = 2l - n$ and defines

$$\bar{a}_p = \sum_r a_r a_{r-p}. \tag{3.67}$$

Accordingly only one sum in Eq. (3.64) remains. The resulting linear system $(\mathbf{A} - 2^{-d}\mathbf{I})\mathbf{\Gamma}^d = 0$ is stated in components

$$\sum_{n=2-\mathcal{N}}^{\mathcal{N}-2} \bar{a}_{2l-n} \Gamma_n^{d;0} = \frac{1}{2^d} \Gamma_l^{d;0}. \tag{3.68}$$

These equations exhibit a unique solution only after adding a normalisation condition of the moments which can be computed in closed form demonstrated in Appendix B.2. Therefore, Eq. (3.50) is differentiated at $p = d$ by the order of its degree

$$\sum_{k\in\mathbb{Z}} M_k^d \phi_k^{(d)}(x) = d!, \tag{3.69}$$

which, after taking the inner product with $\phi(x)$, results in

$$\sum_{l=2-\mathcal{N}}^{\mathcal{N}-2} M_l^d \Gamma_l^{d;0} = (-1)^{d_1} d! \tag{3.70}$$

Here d_1 is the first derivative in the summation (3.54). Clearly one is not simply interested in connection coefficients at scale $j = 0$. Thus, for an arbitrary resolution $j > 0$ the set of homogeneous equations (3.68) remains unchanged and only the r.h.s. of the inhomogeneous moment equation (3.70) acquires an additional factor 2^{jd} which signifies

$$\Gamma_l^{d;k}(j) = 2^{jd} \Gamma_l^{d;k}. \tag{3.71}$$

Remark 3.3 *Equation* (3.68) *implies that the connection coefficient vector* $\mathbf{\Gamma}^d$ *belongs to the eigenspace related to the eigenvalue* $\lambda = 2^{-d}$ *of* $[\mathbf{A}]_{l,n} = \bar{a}_{2l-n}$*. The only exception to this statement is the case* $g = 2$*,* $d = 2$ *where* $\lambda = \frac{1}{4}$ *does not correspond to an eigenvector of* $\mathbf{A}$

$$\{\lambda_n\}_{n=0}^{\mathcal{N}-1} = \{1, \tfrac{1}{2}, \tfrac{1}{4} + 9.95398 \times 10^{-9} i, \tfrac{1}{4} - 9.95398 \times 10^{-9} i, \tfrac{1}{8}\}$$

and henceforth the solution to (3.68) *is ill-defined.*

A similar procedure is applied to deal with the trilinear coefficients (3.58). The leftover difficulty of a high condition number $\kappa_2(\mathbf{A}) = \|A\|_2 \|A^\dagger\|_2$ is tackled by applying shifted Chebyshev polynomials $T_n^*(x) = T_n(2x-1)$ on the interval $[0,1]$ in order to form the extra inhomogeneous equations [39] i.e. mixed moment conditions. Thus, one extends Eq. (3.14) by a change of basis and by replacing the monomials $\{x^d\}$ on the right with an equivalent $T_d^*(x)$ basis of the same degree. Therefore, we match the coefficients $\{t_n^j\}_{j=0}^n$ of the monomials in $T_n^*(x)$ on both sides

$$\sum_{l=2-\mathcal{N}}^{\mathcal{N}-2} \sum_{j=0}^{d} t_d^j M_l^j \phi_l(x) = T_d^*(x)\ . \tag{3.72}$$

Differentiating both sides of this relation d times, similar to Eq. (3.14), yields the redefined moment equation

$$\sum_{l=2-\mathcal{N}}^{\mathcal{N}-2} \sum_{j=0}^{d} t_d^j M_l^j \Gamma_l^{d;0} = (-1)^d 2^{2d-1} d!\ . \tag{3.73}$$

Recall that the d-th derivative of $T_d^*(x)$ respecting the shift causes an additional factor of 2 in comparison to the known $T_d^{(d)}(x) = 2^{d-1}d!$. The problematic part of the matrix $\mathbf{A}$, however, is that the rank deficiency lies in the homogeneous equations (3.68) such that the effect of blending moments only affects results at higher scale of refinement $j > 0$. Equipped with the necessary tools to express the effective action (3.13) in a basis of wavelets, we now discuss the construction of periodic and anti-periodic bases on a finite interval.

3.3.5 Proper Connection Coefficients

For the transition towards finite size extensions in both spatial and temporal direction, we need to compute the connection coefficients of compactly supported wavelets on bounded intervals. These *proper* connection coefficients are introduced in [40] and will be defined on the support range $[0, \mathcal{N}-1]$

$$\Delta_{k_1,\dots,k_n}^{d_1,\dots,d_n} = \int_0^{\mathcal{N}-1} dx \prod_l \phi_{k_l}^{(d_l)}(x) \tag{3.74}$$

such that the integrand has support $[k, \mathcal{N}-1+l]$ for $k > l$. Hence, for the special case when the integrand lies in the computational domain both *proper* and *improper* coefficients are equal. Non-zero values which are different from the already known improper coefficients, correspond to $2-\mathcal{N} \leq k, l \leq -1$ or $1 \leq k, l \leq \mathcal{N}-2$, respectively. The scaling equations as derived in (3.64) constitute of Eq. (3.74) and

$$\Delta_{k_1-(\mathcal{N}-1),\dots,k_n-(\mathcal{N}-1)}^{d_1,\dots,d_n} = \int_0^{\mathcal{N}-1} dx \prod_l \phi_{k_l-(\mathcal{N}-1)}^{(d_l)}(x) \tag{3.75}$$

$$= \int_{\mathcal{N}-1}^{2\mathcal{N}-2} dx \prod_l \phi_{k_l}^{(d_l)}(x) \; . \tag{3.76}$$

To recover improper connection coefficients Λ on the full support $[0, 2\mathcal{N}-2]$ we combine (3.74) and (3.75) for the resulting identity

$$\Delta_{k_1,\dots,k_n}^{d_1,\dots,d_n} + \Delta_{k_1-(\mathcal{N}-1),\dots,k_n-(\mathcal{N}-1)}^{d_1,\dots,d_n} = \Lambda_{0,k_2-k_1,\dots,k_n-k_1}^{d_1,\dots,d_n} \; . \tag{3.77}$$

Furthermore, we limit calculations to the special case mentioned above where the integrand's support in (3.74) never exceeds the integration boundaries. Using this property we will be able to evaluate proper connection coefficients in the finite interval of periodic and anti-periodic basis functions.
This is exactly what was done for the B-splines except that we did not have to pay attention because we could simply analytically evaluate their proper connection coefficients.

3.3.6 Wavelet Basis Functions

As addressed during the introduction of B-splines in Sec. 3.2, we now construct wavelet basis functions $W_{j,k}$ for $k = 0, \dots, L-1$ and $0 \leq x \leq L$ at scale j, shift k and polynomial approximation up to degree $2g-1$. Again g is the genus of the Daubechies wavelet system D_g

$$W_{j,k}^{\text{antiperiodic}}(x) = \phi_{j,k}(x) - \phi_{j,k-L}(x) \tag{3.78}$$

$$W_{j,k}^{\text{periodic}}(x) = \phi_{j,k}(x) + \phi_{j,k-L}(x) \; . \tag{3.79}$$

For $g = 2$ we present both periodic and anti-periodic basis functions on an interval of $L = 6$ in Fig. 3.3.

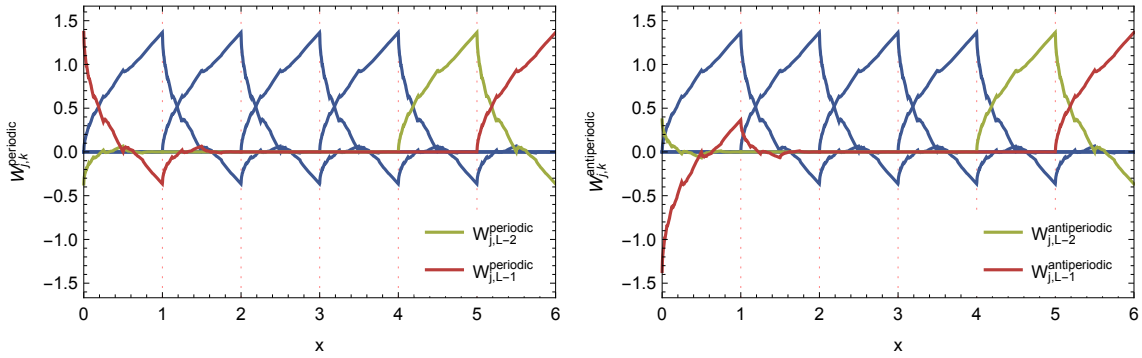

Fig. 3.3: $L = 6$. (a) Periodic Daubechies wavelet basis functions of genus $g = 2$. (b) Anti-periodic Daubechies wavelet basis functions of genus $g = 2$. The blue curves correspond to basis function with full support within the computational domain $[0, L-1]$.

Similarly to the example for B-splines, we inspect Eq. (3.21) for an analogous pathological behaviour regarding unphysical zero modes from Sec. 3.2. Again the comparison of the regularisation schemes on anti-periodic D_3 wavelet pseudoparticles with mode expansion as an eigenfunction reference for the anti-Hermitian $Q = \partial_x$ is illustrated in Fig. 3.2. We assign the shape for the Q-regularisation to the presence of unphysical low lying pseudoparticle modes. Surprisingly, the $Q^\dagger Q$ regularised wavelets also are not just parallel shifted to the plane waves but rather coincide with the $N = 8$ solution at $\sigma = 0$. This result is unexpected but yet means that we have a higher overlap with Q using less basis functions. Hence, wavelets appear to suit the requirements when aiming for a minimal set of physically relevant fermionic pseudoparticles. Reducing the functional basis will be favourable especially when considering the full QCD Dirac operator.

This closes the characterisation of wavelets. In the next chapter we will apply the approaches gathered above within the $(1 + 1)$ dimensional GN model. Finally, we will devise an unbiased procedure to pursue QCD analyses and justify the utilisation of pseudoparticles further.

Chapter 4

Regularisation of the discrete GN_2 Model

Having collected the necessary tools to regularise the GN model in $(1+1)$ dimensions, which is renormalisable in the four-fermi coupling (cf. Sec. 2.1.1), we present different paths prompting the pseudoparticle approach from Ch. 3. We outline parallels between the lattice formulation and the mode expansion before using B-splines and Daubechies wavelets to reconstruct the phase-boundary for both homogeneous and inhomogeneous condensation. By illustrating the cornerstones of these regularisation schemes we fine-tune the procedures in order to develop a wavelet-based unbiased algorithm which is capable of dealing with consecutive calculations in $(3+1)$ dimensions.

4.1 Finite-Density Calculations

In principle the algorithm to determine the phase boundary in the (μ, T)-plane (cf. Fig. 1.1) and the evaluation of $\sigma(x)$ are straightforward when considering QCD effective models. One simply has to find the field configuration that minimises the effective action with respect to σ. In the presence of different phases, we monitor S_{eff} with three solutions of different topologies at our disposal

(I) Restored symmetry $\sigma = 0$

(II) Broken symmetry by homogeneous condensate $\sigma = \text{const.}$

(III) Broken symmetry by spatially inhomogeneous condensate $\sigma = \sigma(x)$

The strategy is to either fix the chemical potential μ or the temperature T, the finite temporal extension L_0 of the box, and to simultaneously vary the other variable in the (μ, T)-plane. For a given μ, we then decrease from high T which coincides with the regime of restored symmetry. For intermediate densities a phase transition occurs from the symmetric towards a crystalline phase in the $(1+1)d$ GN model [8]. This signifies that in the first case $\sigma = 0$ where in the second region $\sigma = \sigma(x)$ oscillating around zero with a given amplitude.

4.1.1 Twisted Chiral Kinks

Before moving to more technical parts for the minimisation procedure of the effective actions, we evaluate some assumptions on the ansatz of the inhomogeneous condensate. In general, the simplest non-constant field configuration is the chiral density-wave ansatz (CDW) [41], which is a one-dimensional plane wave type of the chiral condensate. The latter assumes an oscillating form of $\sigma(x_1) \sim \cos(px_1)$ with momentum p. It has already

been shown that inhomogeneous condensation in $(1+1)d$ is favoured over any constant σ provided densities are high enough [10, 8]. However, when considering multi-fermion bound states *twisted kinks* appear suitable for mostly all regions of the (μ, T)-plane because they are regarded as the elementary building block of hadrons in discrete GN models [16]. This picture is consistent with Dashen-Hasslacher-Neveu (DHN) [9] baryons which interpolate between two different vacua separated in space x and topologically stabilising the single kink-antikink state. The latter corresponds to the baryon solution with mass $m_{\mathrm{B}} = \sigma_0 \frac{2N}{\pi}$ [42] and σ_0 the non-vanishing vacuum expectation value of the scalar field σ.
Naturally the condensate then connects two points on the chiral vacuum manifold S^1 which respects the symmetries of both the discrete GN and the χGN model (cf. Ch. 2). To implement chirally twisted condensates on a regularised system with finite spatial size L_1, it suffices to impose anti-periodic spatial boundary conditions on $\sigma(x_1) = -\sigma(x_1 + L_1)$ and the ψ fields according to Γ in (2.17). A naive functional ansatz is

$$\sigma(x_1) = \sigma_0 \tanh(\sigma_0 x_1) \; . \tag{4.1}$$

Choosing such an explicit functional form fails to reflect the purpose of the survey in this thesis. Possible further minimisation procedures would then depend on this choice which is why we emphasised to conduct an unbiased variational study similar to [10]. Hence, only a suitable orthonormal basis for the Hilbert space $L^2(\mathbb{R})$ is selected (cf. Ch. 3).

Starting from the three solutions (I,II,III) the minimal effective action controls which phase is favoured. Certain regions of the (μ, T)-plane then might be predestined for a different ordering in S_{eff}. Thus, when sweeping through the (μ, T)-plane one encounters reversion points in this ordering of solutions – implying an emergent phase boundary.
The motivation for this approach is its direct extension towards higher dimensions and models that do not enjoy renormalisability. The latter is a UV phenomenon and affects the effective action for (I–III) equivalently. Thereby our algorithm has the advantage to circumvent previously discussed regularisation schemes in $(3+1)$ dimensions e.g. the Pauli-Villars regularisation in the GN_4 model (cf. Sec. 2.1.4). Hence, for both the GN_2 and GN_4 model the process is similar, provided the developed algorithm is stable enough in $(1+1)$ dimensions.

To exemplify this idea, we will obtain the phase boundary of the discrete $(1+1)$ dimensional GN model on the lattice using staggered fermions as well as through mode expansion. Besides, we will use this first section to argue why inhomogeneous condensation should be favoured compared to any translationally invariant special case of σ.

4.2 Lattice Formulations of the GN Model

We present again the gap equation of the discrete GN_2 model (cf. Sec. 2.1.1) which will be our starting point for the formulation of the model on the lattice

$$\frac{1}{\lambda} = \int \frac{d^2k}{(2\pi)^2} \frac{2}{k^2 + \sigma^2} \; , \tag{4.2}$$

together with the trivial stationary point $\sigma = 0$ of S_{eff} in (2.14). Initially, we are merely interested in constant σ and confine the theory in a box by defining

$$S_{\mathrm{eff}}[\sigma] = \lim_{L_1, L_0 \to \infty} \frac{\tilde{S}_{\mathrm{eff}}[\sigma]}{L_1 L_0} \; , \tag{4.3}$$

where the tilde in $\tilde{S}_{\mathrm{eff}}$ designates the discretised version of the effective action with L_0 and L_1 the temporal and spatial extent, respectively. Furthermore, the regularisation of the

theory on the lattice involves introducing a lattice spacing a where the lattice momenta $\hat{k}_\mu$ implied by our discretisation enter

$$\hat{k}_\mu = \frac{2}{a}\sin\frac{ak_\mu}{2}\,, \quad k_0 = \frac{2\pi}{N_0}\left(n_0+\frac{1}{2}\right)\,, \quad k_1 = \frac{2\pi n_1}{N_1}\,, \quad n_\mu \in [0, N_\mu - 1]\ . \tag{4.4}$$

Hence, substituting the integral over momenta k_μ with a discrete sum over $\hat{k}_\mu$ produces the lattice version of the gap equation where we introduced a temperature $T = \frac{1}{L_0}$ reciprocal to L_0. In order to retrieve meaningful results it is advantageous to base numerical calculations on dimensionless quantities. We reformulate all dimensionful quantities in units of $\sigma_0 = \langle\sigma\rangle$, the expectation value of the condensate at zero chemical potential $\mu = 0$ and temperature $T = 0$. Especially the lattice spacing a is now cast to $\hat{a} = (a\sigma_0)$ similar to the coordinates $\hat{x}_\mu = x_\mu\sigma_0$ and

$$\hat{\mu} = \frac{a\mu}{a\sigma_0} = \frac{\mu}{\sigma_0}\,, \quad \hat{\sigma} = \frac{\sigma}{\sigma_0}\,. \tag{4.5}$$

Effectively the gap equation remains unchanged, except that all prior dimensionful quantities are now denoted with a hat $\hat{}$. The lattice counterpart of Eq. (4.2) is obtained by differentiation of the discrete effective action (4.2)

$$\frac{1}{2\hat{\sigma}}\frac{d}{d\hat{\sigma}}\frac{S_{\text{eff}}}{N} = 0\,. \tag{4.6}$$

For an arbitrary chemical potential $\hat{\mu} \geq 0$ this yields

$$\frac{1}{\lambda} = \frac{2}{\hat{L}_0\hat{L}_1}\sum_{n_0,n_1}\frac{\left[\frac{2}{\hat{a}}\sin\frac{\pi(n_0+1/2)}{N_0}\right]^2 + \left[\frac{2}{\hat{a}}\sin\frac{\pi n_1}{N_1}\right]^2 + \hat{\sigma}^2 - \hat{\mu}^2}{\left[\left[\frac{2}{\hat{a}}\sin\frac{\pi(n_0+1/2)}{N_0}\right]^2 + \left[\frac{2}{\hat{a}}\sin\frac{\pi n_1}{N_1}\right]^2 + \hat{\sigma}^2 - \hat{\mu}^2\right]^2 + \left[\frac{4\hat{\mu}}{\hat{a}}\sin\frac{\pi n_1}{N_1}\right]^2}\,, \tag{4.7}$$

which simplifies for zero chemical potential $\hat{\mu} = 0$

$$\frac{1}{\lambda} = \frac{2}{\hat{L}_0\hat{L}_1}\sum_{n_0,n_1}\left[\left[\frac{2}{\hat{a}}\sin\frac{\pi(n_0+1/2)}{N_0}\right]^2 + \left[\frac{2}{\hat{a}}\sin\frac{\pi n_1}{N_1}\right]^2 + \hat{\sigma}^2\right]^{-1}\,. \tag{4.8}$$

4.2.1 Coupling Constant Renormalisation

To define the model uniquely and compute comparable results among different degrees of freedom a coupling constant renormalisation is necessary. The procedure to achieve this uses a predetermined finite temperature and spatial extension at zero chemical potential $\hat{\mu} = 0$. Thus, for given $\hat{a}$, $\hat{L}_1$ and $\hat{L}_{0c}$ corresponding to the critical temperature $\hat{T}_c = \frac{e^{\gamma_E}}{\pi} = 0.567$ [7] one solves the gap equation (4.7) for λ. Here $\gamma_{\text{E}} = 0.577$ is Euler's constant. That also allows to obtain σ as a function of λ which is displayed in the left panel of Fig. 4.1 for different lattice extents. The asymptotic scaling curve $\sigma(\lambda) = 2^{\frac{5}{2}}e^{-\frac{\pi}{\lambda}}$ [3] is also included. As already observed in Fig. 4.1 the value of vanishing condensate σ corresponds to the critical temperature where chiral symmetry is broken. Lastly, the computation at arbitrary finite temperatures $\hat{L}_0 > \hat{L}_{0c}$ requires a zero temperature computation to fix the vacuum expectation value σ_0 and render the constituent quantities finite (4.5). This means, we pick the maximal finite temporal extent $\hat{L}_{00}$ of the order $\mathcal{O}(\hat{L}_1)$ to approximate the zero temperature where $\hat{\sigma} = \frac{\sigma}{\sigma_0} \approx 1$.
From the square dependency of $\hat{a}$ in (4.7), we expect quadratic scaling of the condensate. o check this, we fix $\hat{L}_0 = 3$ i.e. $\hat{T} = \frac{1}{3}$ which yields the scaling behaviour illustrated in Fig. 4.1 (left) where the extrapolated black solid line converges towards the analytically computed value in the infinite-volume continuum $\hat{\sigma}(T) = 0.914$. The formalism displays

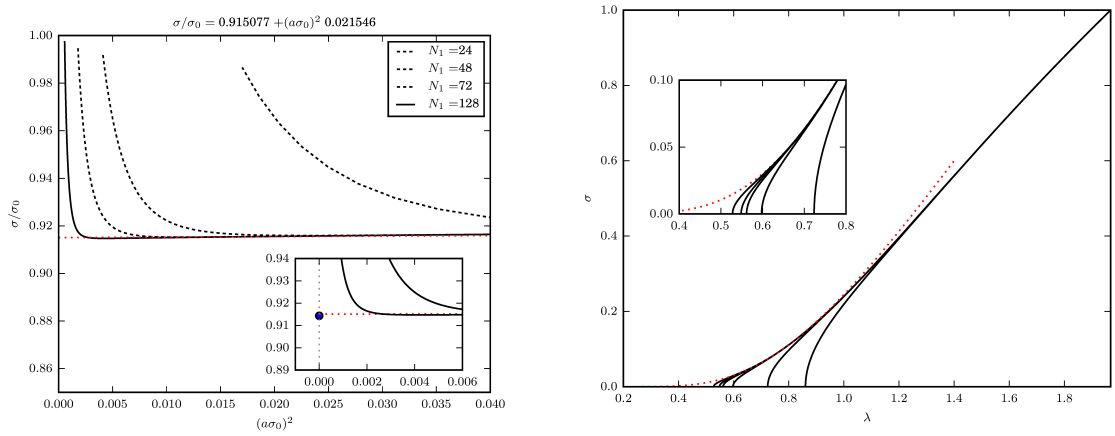

Fig. 4.1: (Right) Condensate σ as a function of the coupling λ for staggered fermions including asymptotic scaling curves (dotted). (Left) Scaling of the condensate σ/σ_0 as a function of $(\sigma_0 a)^2$ for lattice sizes N_1.

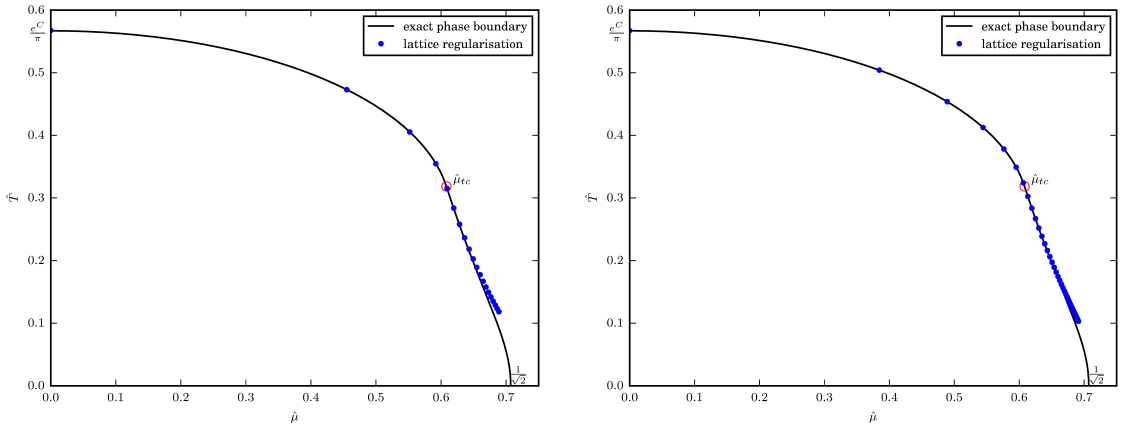

Fig. 4.2: Phase diagram of the GN-model on the lattice assuming a homogeneous condensate $\hat{\sigma} = \text{const.}$ for (left) $N_1 = 30$ and (right) $N_1 = 50$. The underlying solid line and the tri-critical point $\hat{\mu}_{tc}$ present analytic results obtained from [7].

lattice artefacts with positive sign such that the curves approach the continuum limit from above.
Alternatively, one can regard the discussed scaling behaviour (cf. Fig. 4.1) as equivalent to a change in temperature $\hat{T}$ for fixed temporal box size while varying the coupling constant λ. The direct proportionality between lattice spacing $\hat{a}$ and λ allows to mimic a similar way to renormalise the coupling.

With all the free parameters fixed, the phase boundary is then determined by the solution of the gap equation (4.2). Conversely this corresponds to monitoring the discretised effective action from (4.3) for the two solutions of (I) $\hat{\sigma} = 0$ and (II) $\hat{\sigma} = \text{const.}$ for minimised value of $\hat{\sigma}$. Around high values of $\hat{\mu}$ both actions will coincide because the minimum of S_{eff} will be identical with the zero solution outside the region of spinodal decomposition. In comparison with analytical obtained results [7], we show the obtained homogeneous phase boundary in Fig. 4.2 for different lattice sizes. Thus, for an increase in the spatial box size $\hat{L}_1$, we observe the expected increase in accuracy analogous to the scaling of the chiral condensate in Fig. 4.1.

4.2.2 Thermodynamics and Homogeneity of the GN_2 model

The obtained phase diagram shows a second order phase boundary from $\hat{\mu} = 0$ up to the tri-critical point $(\hat{\mu}_{tc}, \hat{T}_{tc})$ whereafter it becomes first order and reaches zero temperature for $\hat{\mu}_c = \frac{1}{\sqrt{2}}$. As argued in the introduction the *naive* GN_2 phase diagram contradicts the known baryon spectrum at zero temperature and is not tenable. At low baryon chemical potential and baryon density one still expects that due to sufficient distance between baryons

$$-\frac{\partial}{\partial \rho_{\mathrm{B}}} \log \mathcal{Z}\big|_{\substack{\rho_{\mathrm{B}}=0 \\ T=0}} = \hat{\mu}_c = m_{\mathrm{B}}. \tag{4.9}$$

However, this would yield a baryon mass identical to the critical value $m_{\mathrm{B}} = \hat{\mu}_c$. The resulting question would be if the mean field approach suffers from a systematic deficiency. Fundamentally, this issue originates from the assumption of a uniform condensate obeying translational invariance which we will relax from now on.

4.2.3 Inhomogeneous Phases of the GN_2 model

We advance with a numerical survey of the phase plane omitting homogeneity in $\hat{\sigma}$ in exchange for spatially dependent condensates. This results in non-trivial solutions of the non-linear functional differential equations from Eq. (2.30). We will use the lattice approach in this subsection to elucidate numerical difficulties related to this change n $\hat{\sigma}$. Remember that in the large N-limit the dominating field configuration is the one that minimises the effective action (2.24). This was easy for uniform mean fields in space-time where one carries out the procedure for only one parameter $\hat{\sigma}$ which was uniformly distributed over all lattice sites in the fermion matrix $Q^\dagger Q$.
Let us exemplify the scenario after the transition towards inhomogeneity. In particular, we remain on the lattice but instead of the preceding naive discretisation, we employ staggered fermions [43] on a two dimensional grid with the altered effective action from (2.14)

$$S_{\mathrm{eff}} = N \sum_x \frac{\sigma(x)^2}{2\lambda} + \sum_{x,y} \bar{\chi}^a(x) Q_{x,y} \chi^a(y), \tag{4.10}$$

for lattice sites x, y and suppressing summation over flavour indices. The fields $\chi^a(x), \bar{\chi}^a(x)$ emerge from one component of the diagonalised Dirac operator and are Grassmann valued but exhibit no Dirac structure. Note that the condensate $\sigma(x)$ explicitly depends on both coordinates and is not yet chosen to be only spatially inhomogeneous. Here x_1 refers to the spatial and x_0 to the temporal coordinate i.e. $x = (x_0, x_1)$. Moreover, we employ the staggered version of the Q-operator consisting of the Dirac operator $D_{x,y}$ and the non-uniform condensate in the staggered formalism

$$\begin{aligned} Q_{x,y} =& \frac{1}{2}\left[\delta_{x,y+\hat{1}} - \delta_{x,y-\hat{1}}\right] + \frac{1}{2}(-1)^{x_1}\left[e^{+\mu}\delta_{x,y+\hat{0}} - e^{-\mu}\delta_{x,y-\hat{0}}\right] && (4.11) \\ &+ \frac{1}{4}\left[\sigma(x) + \sigma(x-\hat{1}) + \sigma(x-\hat{0}) + \sigma(x-\hat{1}-\hat{0})\right] , && (4.12) \end{aligned}$$

with $\hat{1}$ and $\hat{0}$ the unit vectors in space and time direction. We also define the site dependent staggered sign functions in front of the derivative terms

$$\eta_\mu(x) = (-1)^{\sum_{i=1}^{\mu-1} x_i} , \quad \eta_1 = 1 , \quad \eta_0 = (-1)^{x_1} , \tag{4.13}$$

where $\eta_0 = \eta_d$ with d the dimensionality of the model. In this way the degrees of freedom are placed on non-intersecting hypercubes $h_\mu = 0, 1, \ldots, N_\mu/2 - 1$ sketched in Fig. 4.3 which require the discrete spatial or temporal extent N_μ to be even. Corresponding site labels then assume values in the range $x_\mu = 0, 1, \ldots, N_\mu - 1$. On terms of the hypercubes,

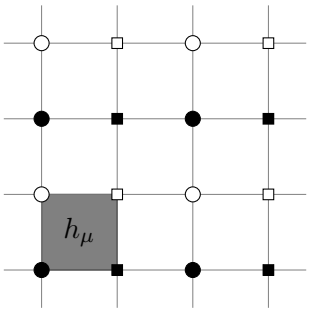

Fig. 4.3: Distribution of the 2^d degrees of freedom on hypercubes in a $d = 2$ lattice.

coordinate labels are restated $x_\mu = 2h_\mu + s_\mu$ where $s_\mu = 0, 1$ within the respective hypercube. An additional even exponent leaves the staggered sign (4.13) invariant such that it becomes only dependent on s i.e. $\eta_\mu(x) = \eta_\mu(s)$.
The introduction of the chemical potential μ in the temporally discretised enhanced Dirac operator (4.11) via weighting the temporal derivative with $e^{\pm\mu}$ is equivalent to the imaginary extension of $\partial_t \to (\partial_t - i\mu)$ in (2.4) for Euclidean space-time [13]. The counterpart of the γ_5-Hermiticity prescription is defined via

$$\eta_5(x) = (-1)^{x_1+x_2}. \tag{4.14}$$

Notably η_5 also acquires a site dependency and in the chiral limit $m_0 = 0$, we encounter a remnant chiral symmetry preserving (2.17) in the discrete GN model

$$\chi^a(x) \to (-1)^{x_1+x_2}\chi^a(x)\,, \quad \bar{\chi}^a \to -(-1)^{x_1+x_2}\bar{\chi}^a(x)\,, \quad \sigma \to -\sigma\,. \tag{4.15}$$

Finally, the condensate's structure of the Q-operator in the second line of (4.11) is not arbitrary. It originates in order to avoid naive diagonal terms $\sigma(x)\delta_{x,y}$ and to make sure the continuum limit is reproduced correctly by averaging over the four nearest neighbour sites [44]. In the resulting fermion matrix $Q_{x,y}$ the condensate degrees of freedom are spread over the diagonal. For later purposes, we will employ the peculiar choice of a condensate that is fully spatially inhomogeneous but independent of the temporal direction $\sigma(x_0, x_1) = \sigma(x_1)$.
Returning to the numerical minimisation of (4.10), the difficulty lies in the computation of the matrix-logarithm and/or the determinant. By discretising the theory, the approximation of $\sigma(x_1)$ is strictly relying on the spatial extent of the lattice – the number of sites N_1 in spatial direction. In other words, the degrees of freedom of the χ^a fields are equivalent to the coefficients of the condensate that have to be minimised. Conversely, this signifies that by choosing bigger lattices one not only has to deal with more expensive computations of the fermion determinant but also the minimisation will become cumbersome. Notably also here we favour the matrix $Q^\dagger Q$ (cf. Sec. 3.1.1).

To this end, we reproduce the revised inhomogeneous phase boundary at a spatial extent of $N_1 = 30$ which permits to relate the results to the previous homogeneous solution in Fig. 4.4. The coupling renormalisation procedure for λ is then equivalent to the one proposed before in Sec. 4.2.1. The resultant boundary is depicted in Fig. 4.4. We clearly observe the three regimes of solutions (I–III) and more importantly a different value for the critical chemical potential $\hat{\mu}_c = \frac{2}{\pi}$ at $\hat{T} = 0$ which is in agreement with the expected baryon density in two dimensions [8]. The emergent crystalline phase for $\hat{\mu}$ higher than $\hat{\mu}_c$ enjoys solutions for non-constant condensates and minimal effective actions in this regime. These results are in agreement with the analytically obtained phase boundary by [8] in the

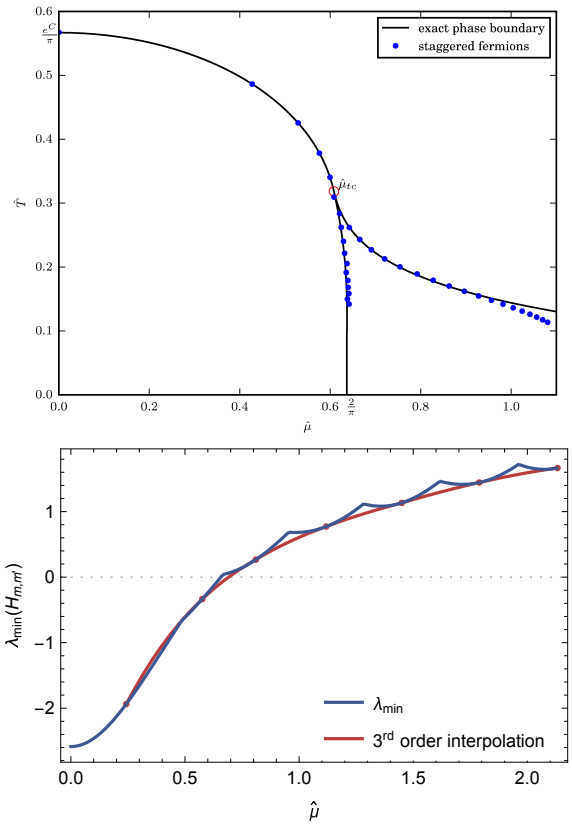

Fig. 4.4: Phase diagram of GN_2 model on the lattice using staggered fermions assuming an inhomogeneous condensate $\hat{\sigma} = \hat{\sigma}(\hat{x}_1)$ for (left) $N_1 = 30$ and (right) the corresponding lowest eigenvalue $\lambda_{\min}$ of the Hessian at $\hat{T} = 0.227$. The underlying line and the tri-critical point $\hat{\mu}_{tc}$ show analytic results obtained from [45].

continuum when extrapolated to infinite volume. The remaining obstacle is a continuation of the procedure to higher dimensions which affects computational time tremendously. The apparent argument lies in the computational complexity of both the functional determinant of $Q^\dagger Q$ with order $\mathcal{O}(N_1^3)$ by means of a LU-decomposition and the subsequent minimisation of maximal $\mathcal{O}(M)$ due to the fact that $\hat{\sigma}$ is discretised along the spatial direction $\hat{\sigma}(x_1) \propto \sum_m \sigma_m$ with $m = 1, \ldots, N_1$. Here M is the number of degrees of freedom of the condensate which is $N_1 = M$ on the lattice. One possible solution we discussed in Sec. 4.1.1 is to pick a special functional ansatz for the chiral condensate which, however, is very restrictive.
Apart from that, one can further reduce the degrees of freedom M in $\hat{\sigma}$ by selecting an orthonormal basis for the fermion fields and the condensate thereof. In this generalisation the solution will be maximally unbiased which is why the pseudoparticle approach is suggested as a suitable basis choice. For a less abrupt transition, we span the discussion employing a finite-mode regularisation closely related to using pseudoparticles.

4.3 Finite-Mode Regularisation

Having explored the lattice formulation of the theory, one can again start out from the GN_2 effective action (2.14) and consider a finite volume of space time $\hat{L}_0 \times \hat{L}_1$ with the Q-operator (2.9) in the $Q^\dagger Q$-regularisation (cf. Sec. 3.1.1).
Eigenfunctions of the pure Dirac operator D without the σ term in Q are plane waves which makes an expansion of the fermion fields in this functional basis a natural choice. As in the lattice expression (4.5), we ensure dimensionless quantities in units of σ_0. Additionally, the fermionic fields fulfill anti-periodic and periodic boundary conditions for temporal (3.3) and also spatial direction (cf. Sec. 4.1.1), respectively

$$\hat{k}_0 = \frac{2\pi}{\hat{L}_0}\left(n_0 + \frac{1}{2}\right) , \quad \hat{k}_1 = \frac{2\pi}{\hat{L}_1} n_1, \quad n_0, n_1 \in \mathbb{Z} , \tag{4.16}$$

acting on both Dirac components. The fields are rephrased as

$$\hat{\psi}^a(\hat{x}_0, \hat{x}_1) = \frac{\psi^a(x_0, x_1)}{\sqrt{\sigma_0}} = \sum_{n_0, n_1} \eta^a_{n_0, n_1} \frac{e^{-i(\hat{k}_0 \hat{x}_0 + \hat{k}_1 \hat{x}_1)}}{\sqrt{\hat{L}_0 \hat{L}_1}}, \tag{4.17}$$

$$\hat{\bar{\psi}}^a(\hat{x}_0, \hat{x}_1) = \frac{\bar{\psi}^a(x_0, x_1)}{\sqrt{\sigma_0}} = \sum_{n_0, n_1} \bar{\eta}^a_{n_0, n_1} \frac{e^{+i(\hat{k}_0 \hat{x}_0 + \hat{k}_1 \hat{x}_1)}}{\sqrt{\hat{L}_0 \hat{L}_1}}. \tag{4.18}$$

In these discrete Fourier series the dimensionless Grassmann variables $\eta^a_{n_0,n_1}$, $\bar{\eta}^a_{n_0,n_1}$ have entered. When studying only a finite number of modes, we set the cut-off to be $\pi/\hat{L}_{0,1}$ bigger than the largest momentum in every direction

$$\hat{k}_0^{\text{cut}} = \frac{2\pi}{\hat{L}_0} N_0, \quad \hat{k}_1^{\text{cut}} = \frac{2\pi}{\hat{L}_1}\left(N_1 + \frac{1}{2}\right). \tag{4.19}$$

For the finite-mode regularisation, we start from the effective action (2.14) and insert the mode expanded fermion fields (4.17) and (4.18) with inhomogeneous condensate hich yields the most general expression of the action. However, for spatially non-uniform $\hat{\sigma}(x_1)$ the plane waves are no longer eigenfunctions of Q which means that the functional $\log(\det Q^\dagger Q)$ needs to be expanded in the plane wave basis of the fermionic fields. We define the Hermitian matrix $Q^\dagger Q$ in the functional basis ith factorising G_{k_μ}

$$G_{\hat{k}_0, \hat{k}_1} = G_{\hat{k}_0} G_{\hat{k}_1} = \frac{e^{\mp i(\hat{k}_0 \hat{x}_0)}}{\sqrt{\hat{L}_0}} \frac{e^{\mp i(\hat{k}_1 \hat{x}_1)}}{\sqrt{\hat{L}_1}} = \frac{e^{\mp i(\hat{k}_0 \hat{x}_0 + \hat{k}_1 \hat{x}_1)}}{\sqrt{\hat{L}_0 \hat{L}_1}} \tag{4.20}$$

Furthermore, we carry out the computation of the matrix elements analytically

$$\begin{aligned}\left\langle G_{\hat{k}_0,\hat{k}_1}|Q^\dagger Q|G_{\hat{k}_0',\hat{k}_1'}\right\rangle &= \frac{1}{\hat{L}_0\hat{L}_1}\int d\hat{x}_0\int d\hat{x}_1\, e^{i(\hat{k}_0\hat{x}_0+\hat{k}_1\hat{x}_1)}\left(-\gamma_\mu\hat{\partial}_\mu+\gamma_0\hat{\mu}+\hat{\sigma}(\hat{x}_1)\right)\\ &\times\left(+\gamma_\mu\hat{\partial}_\mu+\gamma_0\hat{\mu}+\hat{\sigma}(\hat{x}_1)\right)e^{-i(\hat{k}_0'\hat{x}_0+\hat{k}_1'\hat{x}_1)} \qquad (4.21)\\ &= \frac{\delta_{\hat{k}_0,\hat{k}_0'}}{\hat{L}_1}\int d\hat{x}_1\, e^{i\hat{k}_1\hat{x}_1}\left(i\gamma_0\hat{k}_0+i\gamma_1\hat{k}_1+\gamma_0\hat{\mu}+\hat{\sigma}(\hat{x}_1)\right)\\ &\times\left(-i\gamma_0\hat{k}_0'-i\gamma_1\hat{k}_1'+\gamma_0\hat{\mu}+\hat{\sigma}(\hat{x}_1)\right)e^{-i\hat{k}_1'\hat{x}_1}\ . \qquad (4.22)\end{aligned}$$

where we inserted the definition of the integral representation of the Kronecker delta. The result (4.21) does not require any specification of the boundary conditions on $\hat{\sigma}(\hat{x}_1)$ as well as its ansatz. The simplest form of the chiral condensate is homogeneous $\hat{\sigma}(\hat{x}_1)=\hat{\sigma}$ which renders the matrix $\langle G_{\hat{k}_0,\hat{k}_1}|Q^\dagger Q|G_{\hat{k}_0',\hat{k}_1'}\rangle$ block diagonal. The determinant reduces to

$$\begin{aligned}\log\det(Q^\dagger Q) &= \log\left\{\prod_{\hat{k}_0,\hat{k}_1}\det\left[(i\gamma_\mu\hat{k}_\mu-\gamma_0\hat{\mu}+\hat{\sigma})(-i\gamma_\mu\hat{k}_\mu+\gamma_0\hat{\mu}+\hat{\sigma})\right]\right\}\\ &= \log\left\{\prod_{\hat{k}_0,\hat{k}_1}\left[(\hat{k}_0^2+\hat{k}_1^2+\hat{\sigma}^2-\hat{\mu}^2)^2+(2\hat{\mu}\hat{k}_0)^2\right]\right\}\ . \qquad (4.23)\end{aligned}$$

where in the second line we utilised the factorisation of determinants of block diagonal matrices. Linear terms in $\hat{\mu}\hat{\sigma}$ have dropped because carrying out (4.23) gives only rise to quadratic terms. Together with (2.14) and insertion of (4.17) and (4.18) with determinant (4.23), we obtain a finite-mode regularised effective action

$$\begin{aligned}\frac{S_{\text{eff}}}{N} &= \frac{\hat{L}_0\hat{L}_1\hat{\sigma}^2}{2\lambda}\\ &-\frac{1}{2}\sum_{n_0=-N_0}^{N_0-1}\sum_{n_1=-N_1}^{N_1}\log\left\{\left[\left[\frac{2\pi}{\hat{L}_0}\left(n_0+\frac{1}{2}\right)\right]^2+\left[\frac{2\pi}{\hat{L}_1}n_1\right]^2+\hat{\sigma}^2-\hat{\mu}^2\right]^2\right.\\ &\left.+\left[2\hat{\mu}\frac{2\pi}{\hat{L}_0}\left(n_0+\frac{1}{2}\right)\right]^2\right\}\ . \qquad (4.24)\end{aligned}$$

The major difference to (4.7) appears in the finite-mode momenta (4.16) in contrast to the ones on the lattice (4.4). Hence, also the sum extends symmetrically over the finite-modes $n_0\in[-N_0,N_0-1]$ and $n_1\in[-N_1,N_1]$. Likewise, in (4.26) the regulator of this scheme is introduced via the aforementioned lattice cut-offs $\hat{k}_0^{\text{cut}},\hat{k}_1^{\text{cut}}$ (4.19) different in both temporal and spatial direction $\hat{k}_0^{\text{cut}}\neq\hat{k}_1^{\text{cut}}$. With this modification the effective action is altered

$$\begin{aligned}\frac{S_{\text{eff}}}{N} &= \frac{2\pi^2N_0(N_1+1/2)\hat{\sigma}^2}{\lambda\hat{k}_0^{\text{cut}}\hat{k}_1^{\text{cut}}}\\ &-\sum_{n_0=1}^{N_0}\sum_{n_1=-N_1}^{N_1}\log\left\{\left[\left(\hat{k}_0^{\text{cut}}\frac{n_0+1/2}{N_0}\right)^2+\left(\hat{k}_1^{\text{cut}}\frac{n_1}{N_1+1/2}\right)^2+\hat{\sigma}^2-\hat{\mu}^2\right]^2\right.\\ &\left.+\left(2\hat{\mu}\hat{k}_0^{\text{cut}}\frac{n_0+1/2}{N_0}\right)^2\right\}\ . \qquad (4.25)\end{aligned}$$

Conversely, upon minimisation of S_{eff} of the discrete GN_2 model in Eq. (4.25) with respect to $\hat{\sigma}$, we arrive at either the trivial solution $\hat{\sigma}=0$ from (4.6) or solutions arising from the

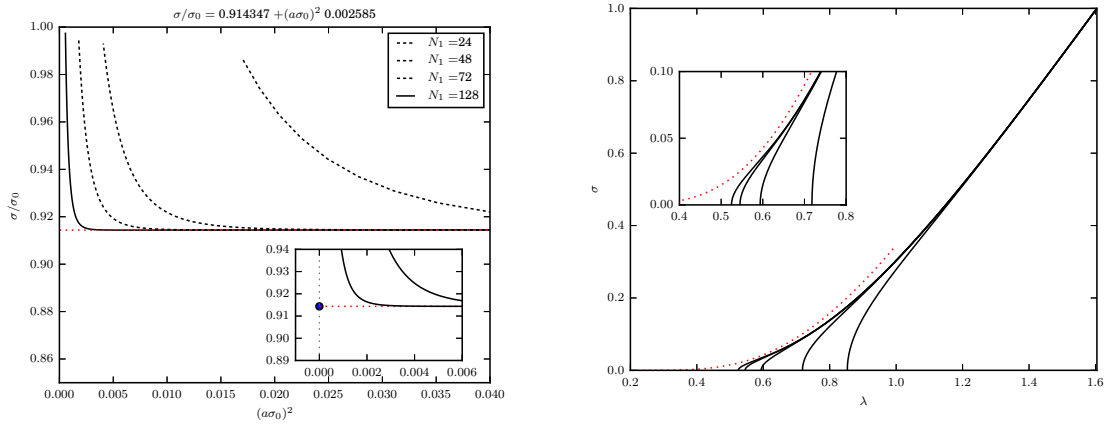

Fig. 4.5: (Right) Condensate σ as a function of the coupling λ for mode expanded fermions including asymptotic scaling curves (dotted). (Left) Scaling of the condensate σ/σ_0 as a function of $(\sigma_0 a)^2$ for number of lowest modes N_1.

gap equation in the same manner as for the lattice regularisation scheme (4.7)

$$\frac{1}{\lambda} = \frac{2}{\hat{L}_0\hat{L}_1}\sum_{n_0,n_1}\frac{\left[\frac{2\pi}{\hat{L}_0}\left(n_0+\frac{1}{2}\right)\right]^2+\left[\frac{2\pi}{\hat{L}_1}n_1\right]^2+\hat{\sigma}^2-\hat{\mu}^2}{\left[\left[\frac{2\pi}{\hat{L}_0}\left(n_0+\frac{1}{2}\right)\right]^2+\left[\frac{2\pi}{\hat{L}_1}n_1\right]^2+\hat{\sigma}^2-\hat{\mu}^2\right]^2+\left[\frac{4\pi\hat{\mu}}{\hat{L}_0}\left(n_0+\frac{1}{2}\right)\right]^2}\,. \tag{4.26}$$

with $n_0 \in [0, N_0-1]$ and $n_1 \in [-N_1, N_1]$ reducing to its zero chemical potential expression

$$\frac{1}{\lambda} = \frac{2}{\hat{L}_0\hat{L}_1}\sum_{n_0,n_1}\left[\left[\frac{2\pi}{\hat{L}_0}\left(n_0+\frac{1}{2}\right)\right]^2+\left[\frac{2\pi}{\hat{L}_1}n_1\right]^2+\hat{\sigma}^2\right]^{-1}\,. \tag{4.27}$$

The latter gives rise to the phase diagram of the homogeneous fermion condensate. The gap equations (4.7) and (4.26) allow to compare the two procedures on the lattice and in the mode expansion, respectively. After a redefinition of the cut-offs (4.19) regarding a lattice spacing namely $\hat{k}_{0,1}^{\text{cut}} = 2\pi/\hat{a}$, we obtain the lattice equivalent of the action. Their momenta still differ as seen in (4.4) for the lattice and (4.16) for the finite-modes. Nevertheless, in the infrared regime $\hat{L}_\mu \to \infty$ both formulations are equivalent which also holds for the UV limiting case $(a\sigma_0) \to 0$ when removing the regulator. Here the finite-mode formalism also approaches lattice calculations. For fixed temperature and chemical potential both regularisation schemes converge to the infinite-volume continuum result with $\mathcal{O}(\hat{a}^2)$. This can be seen in Figures 4.1 and 4.5 where for a given temperature $\hat{T} = 1/3$ both formalisms have identical scaling behaviour and positive sign lattice artefacts with an increase in the cut-off (lattice spacing).

The aim for expanding in a finite number of modes is to approach continuum infinite-volume results by still keeping computational resources low. The effective action (4.25) is determined by choosing the free parameters λ, N_0, N_1, $\hat{k}_0^{\text{cut}}$, $\hat{k}_1^{\text{cut}}$ in an optimal way to minimise the number of finite modes N_0, N_1 and reduce finite size effects. As mentioned for the lattice, we need a coupling constant renormalisation before computations become comparable (cf. Sec. 4.2.1). In this context $\hat{k}_0^{\text{cut}}$ and λ cannot be chosen independently because the cut-off relation (4.19) imposes

$$\hat{k}_0^{\text{cut}} = 2\pi N_{0c}\hat{T}_c, \tag{4.28}$$

where N_{0c} is the number of temporal modes matching the critical temperature $\hat{T}_c$. The freedom in most of the parameters allows a more refined λ renormalisation where we can

even tune a low number of modes $\hat{k}_\mu$ to closely retrieve analytic results from [7]. As usual, we focus on zero chemical potential calculations $\hat{\mu} = 0$ for the critical temperature $\hat{T}_c$ and maximal number of modes in temporal direction denoted as N_{00}. First, to determine $\hat{k}_0^{\text{cut}}$, the gap equation (4.27) at $\hat{\mu} = 0$ and $\hat{T} = \hat{T}_c$ needs to satisfy $\hat{\sigma} = 0$ at the phase boundary

$$\frac{\pi^2(N_1 + 1/2)}{\lambda \hat{k}_0^{\text{cut}} \hat{k}_1^{\text{cut}}} = \frac{1}{N_{0c}} \sum_{n_0=1}^{N_{0c}} \sum_{n_1=-N_1}^{N_1} \left[\left(\hat{k}_0^{\text{cut}} \frac{n_0 + 1/2}{N_0} \right)^2 + \left(\hat{k}_1^{\text{cut}} \frac{n_1}{N_1 + 1/2} \right)^2 \right]^{-1} . \quad (4.29)$$

Similarly at $\hat{\mu} = 0$ and approximately $\hat{T} = 0$ the condensate assumes $\hat{\sigma} \approx 1$

$$\begin{aligned} &\frac{\pi^2(N_1 + 1/2)}{\lambda \hat{k}_0^{\text{cut}} \hat{k}_1^{\text{cut}}} = \\ &= \frac{1}{N_{00}} \sum_{n_0=1}^{N_{00}} \sum_{n_1=-N_1}^{N_1} \left[\left(\hat{k}_0^{\text{cut}} \frac{n_0 + 1/2}{N_0} \right)^2 + \left(\hat{k}_1^{\text{cut}} \frac{n_1}{N_1 + 1/2} \right)^2 + 1 \right]^{-1} . \end{aligned} \quad (4.30)$$

Consistency in λ demands equating the right-hand sides of Eqs. (4.29) and (4.30) which recovers the dependence of $\hat{k}_0^{\text{cut}}(N_{0c})$. Eventually one fixes the mode numbers N_{0c}, N_{00}, N_1 and $\hat{k}_1^{\text{cut}}$ from where the resulting equation

$$\begin{aligned} \sum_{n_1=-N_1}^{N_1} \Bigg\{ &\frac{1}{N_{0c}} \sum_{n_0=1}^{N_{0c}} \left[\left(\hat{k}_0^{\text{cut}} \frac{n_0 + 1/2}{N_0} \right)^2 + \left(\hat{k}_1^{\text{cut}} \frac{n_1}{N_1 + 1/2} \right)^2 \right]^{-1} \\ &- \frac{1}{N_{00}} \sum_{n_0=1}^{N_{00}} \left[\left(\hat{k}_0^{\text{cut}} \frac{n_0 + 1/2}{N_0} \right)^2 + \left(\hat{k}_1^{\text{cut}} \frac{n_1}{N_1 + 1/2} \right)^2 + 1 \right]^{-1} \Bigg\} = 0 \end{aligned} \quad (4.31)$$

permits to compute $\hat{k}_0^{\text{cut}}$. Inserting the result into one of the gap equations (4.29) and (4.30) at $\hat{\mu} = 0$ produces the corresponding value for λ.
In comparison with the lattice formalism, we reproduce the same scaling plots regarding the chiral condensate as a function of the coupling and the quadratic convergence of σ depicted in Fig. 4.5. We observe a high similarity for the same amount of degrees of freedom N_1, namely lattice sites on the one hand and number of modes on the other hand. As mentioned before, we also have lattice artefacts which are present in both models with the same sign. The condensate's scaling approaches a different asymptotic scaling curve.

The approach described in Sec. 4.1 allows us to keep track of both the effective actions for the symmetric $\hat{\sigma} = 0$ and homogeneous broken phase $\hat{\sigma} = \text{const}$. The expected change in the ordering results from an increased $S_{\text{eff}}[\hat{\sigma}]$ due to the non-zero chiral condensate in Eq. (4.25). The kink on the r.h.s. of Fig. 4.6 marks the upper spinodal line before the second minimum in S_{eff} vanishes for the trivial $\hat{\sigma} = 0$.
In Fig. 4.7 we present the plane wave expanded phase boundary for two spatial extents with number of spatial modes $N_1 = 30$ and $N_1 = 50$ (degrees of freedom) and the corresponding parameters summarised in Tab. 4.1. The method of the optimisation of $\hat{k}_\mu^{\text{cut}}$ was adopted from [10].

4.3.1 Matsubara Summation

In the previous calculation both the spatial as well the temporal extent of the box are finite. In the following we present an alternative approach which permits to dispose of the integration over the temporal direction. We adjust the momentum integrals of functions $f(k_0, \mathbf{k})$

$$\int \frac{d^2k}{(2\pi)^2} f(k_0, \mathbf{k}) \to iT \sum_n \int \frac{dk}{(2\pi)} f[i(\omega_n - i\mu), \mathbf{k}] , \quad (4.32)$$

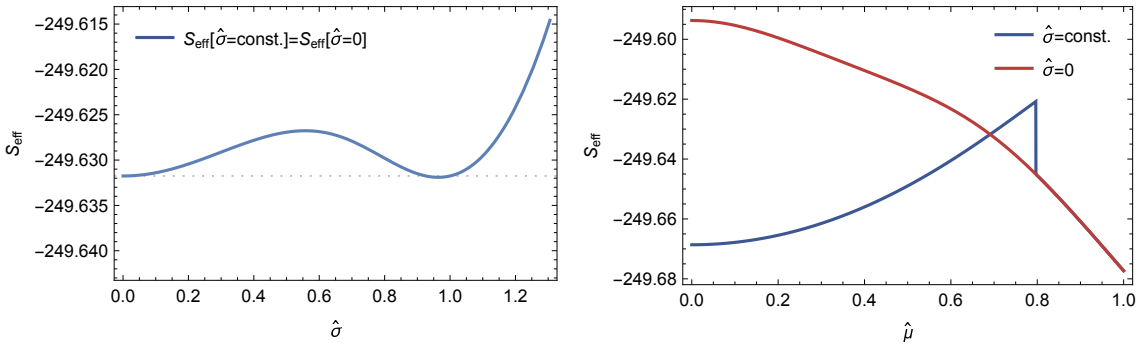

Fig. 4.6: Effective action $S_{\text{eff}}[\hat{\mu}]$ with change in ordering at $\hat{\mu} = 0.692$ and $\hat{T} = 0.113$ for the symmetric $\hat{\sigma} = 0$ and broken phase $\hat{\sigma} \neq 0$. Number of spatial modes $N_1 = 30$.

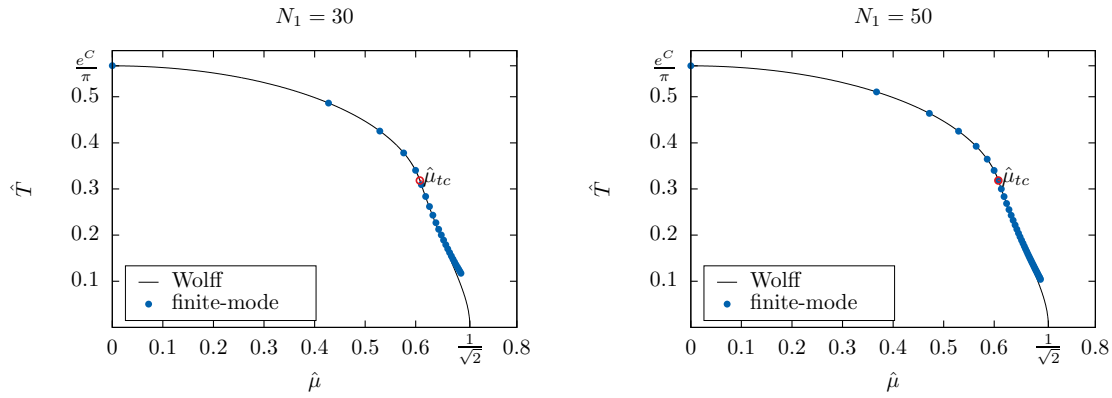

Fig. 4.7: Mode expanded phase diagram of the GN_2 model assuming a homogeneous condensate $\hat{\sigma} = \text{const.}$ for (left) $N_1 = 30$ and (right) $N_1 = 50$. The underlying line and the tri-critical point $\hat{\mu}_{tc}$ show analytic results obtained from [7].

Tab. 4.1: Optimised parameters for the finite-mode regularisation given a spatial number of modes N_1 with critical number of temporal modes N_{0c}, momentum cut-offs $\hat{k}_\mu^{\text{cut}}$ and coupling constant λ.

N_1	N_{0c}	$\hat{k}_0^{\text{cut}}$	$\hat{k}_1^{\text{cut}}$	λ
30	6	21.387	21.374	0.990
50	9	32.069	32.060	0.878

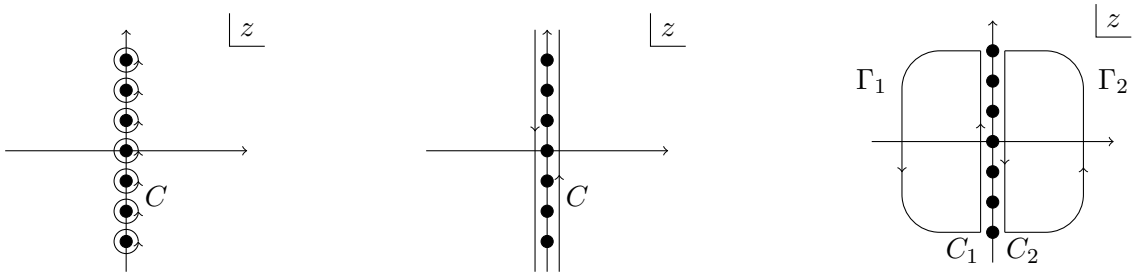

Fig. 4.8: Contours over fermionic Matsubara modes $i\omega_n$ on the complex axis.

of the zero mode using $k_0 \to 2\pi(n+1/2)T \equiv \omega_n$, $n \in \mathbb{Z}$ in agreement with (4.16). Assuming that the fermion condensate is inhomogeneous with regard to spatial separations only, an explicit integration over the temporal modes is performed using summation over Matsubara frequencies. To evaluate the sum explicitly, one has to deal with expressions of the form [31]

$$S_{\mathrm{F}} = \frac{1}{\beta}\sum_{i\omega} g(i\omega)\ . \tag{4.33}$$

The sum can be rewritten as a contour integral under the use of a weighting function v_β which exhibits simple poles at the desired ω_n on the complex axis

$$S_{\mathrm{F}} = \frac{1}{2\pi i\beta}\oint dz\ g(z)v_\beta(z)\ , \tag{4.34}$$

where we chose the poles to be at $z = i\omega_n$. The choice of the Matsubara weighting functions is rather delicate. Two possibilities are either

$$v_\beta^{(1)} = \frac{\beta}{1+e^{-\beta z}} = \beta N_\beta^{\mathrm{F}}(-z) = \beta(1-N_\beta^F(z)) \tag{4.35}$$

$$v_\beta^{(2)} = \frac{-\beta}{1+e^{\beta z}} = -\beta N_\beta^{\mathrm{F}}(z)\ , \tag{4.36}$$

where $v_\beta^{(1)}$ and $v_\beta^{(2)}$ handle the convergence of the integrand on $\Re(z) < 0$ and $\Re(z) > 0$ respectively. We rewrote the result by using the fermionic occupation numbers $N_\beta^{\mathrm{F}}(z) = 1/(1+\exp(\beta z))$. Otherwise regarding the denominator also

$$v_\beta = \frac{1}{2}\tanh\left(\frac{\beta z}{2}\right) = \frac{1-e^{\beta z}}{2(1+e^{\beta z})}\ , \tag{4.37}$$

becomes a valid candidate. The equivalence of the contour integral with the summation over modes ω_n allows to deform the contour as sketched in Fig. 4.8 such that

$$S_{\mathrm{F}} = \frac{1}{2\pi i\beta}\left(-\int_{-i\infty-\varepsilon}^{i\infty-\varepsilon} dz\ g(z)v_\beta(z) + \int_{-i\infty+\varepsilon}^{i\infty+\varepsilon} dz\ g(z)v_\beta(z)\right)\ . \tag{4.38}$$

Furthermore, both individual integrations are decomposed into

$$\int_{-i\infty-\varepsilon}^{i\infty-\varepsilon} = \oint_{C_1} - \int_{\Gamma_1} \text{ and } \int_{-i\infty+\varepsilon}^{i\infty+\varepsilon} = \int_{\Gamma_2} - \oint_{C_2}\ , \tag{4.39}$$

employing the fact that for $|z| \to \infty$ both Γ_i contributions vanish requiring $g(z)v_\beta(z) \to 0$. Eventually the integrations encompass only poles originating from $g(z)$

$$S_{\mathrm{F}} = -\frac{1}{\beta}\sum_{z_0 \in g(z)\ \text{poles}} \mathrm{Res}\ \{g(z_0)v_\beta(z_0)\}\ , \tag{4.40}$$

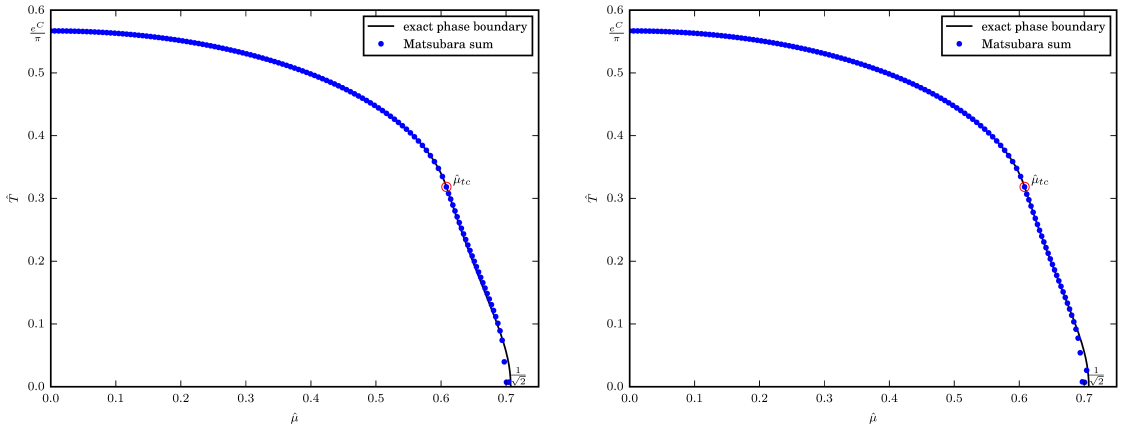

Fig. 4.9: Mode expanded phase diagram of the GN_2 model assuming a homogeneous condensate $\hat{\sigma} = \text{const.}$ for (left) $N_1 = 30$ and (right) $N_1 = 50$ with Matsubara mode summation. The underlying solid line and the tri-critical point $\hat{\mu}_{tc}$ show analytic results obtained from [7].

where now the change in orientation of the integrations is denoted by the additional minus sign. To this end, the expression for the effective action becomes

$$\frac{S_{\text{eff}}}{N} = \frac{\sigma^2}{2\lambda} - T \sum_{n_0} \int \frac{dk_1}{2\pi} \log\left[(\omega_{n_0} - i\mu)^2 + \omega_{k_1}^2(\sigma)\right] \,, \tag{4.41}$$

using $\omega_{k_1}^2(\sigma) = \hat{k}_1^2 + \hat{\sigma}^2$. In correspondence with Eq. (4.25) and its derived gap equation (4.26) we trade the zero momentum $\hat{k}_0$ for the aforementioned Matsubara frequencies along the imaginary axis and identify ω_{k_1} and arrive at

$$\frac{\hat{L}_0}{2\lambda} = \frac{1}{\hat{L}_1} \sum_{i\omega_{n_0}} \sum_{n_1=-N_1}^{N_1} \frac{-\omega_{n_0}^2 + \omega_{k_1}^2 - \hat{\mu}^2}{\left[-\omega_{n_0}^2 + \omega_{k_1}^2 - \hat{\mu}^2\right]^2 - 4\hat{\mu}^2\omega_{n_0}^2} \,. \tag{4.42}$$

The procedure regarding the explicit summation now conveniently disposes of the sum over temporal modes via the residues at the poles of the denominator.

$$\frac{\hat{L}_0}{2\lambda} = \sum_{n_1=-N_1}^{N_1} \frac{1}{4\omega_{k_1}} \left(\tanh\left(\frac{\omega_{k_1} + \hat{\mu}}{2\hat{T}}\right) + \tanh\left(\frac{\omega_{k_1} - \hat{\mu}}{2\hat{T}}\right)\right) \,. \tag{4.43}$$

Similarly the sum of Matsubara frequencies in the large-N approximation for the effective potential itself reduces to

$$\frac{S_{\text{eff}}}{N} = \frac{\hat{\sigma}^2}{2\lambda} - \sum_{n_1=-N_1}^{N_1} \left[\omega_{k_1}(\hat{\sigma})\right. \tag{4.44}$$

$$+ \hat{T} \log\left(1 + \exp\left\{-[\omega_{k_1}(\hat{\sigma}) + \hat{\mu}]/\hat{T}\right\}\right) \tag{4.45}$$

$$\left. + \hat{T} \log\left(1 + \exp\left\{-[\omega_{k_1}(\hat{\sigma}) - \hat{\mu}]/\hat{T}\right\}\right)\right] \,. \tag{4.46}$$

Eventually the integral over spatial modes is discretised again in the mode expanded field momenta (4.16). The resultant phase boundary in Fig. 4.9 is obtained using the same parameters for the $\hat{k}_1^{\text{cut}}$ cut-off and also the number of degrees of freedom in the spatial direction from Tab. 4.1.

4.3.2 Spatially Inhomogeneous Condensate using Finite-Modes

We have already obtained the inhomogeneous phase boundary on the lattice in Fig. 4.4 where we compared the results with the proposed analytical result [45] in the kink-crystal phase $\sigma(x_1)$ using the Lamé potential [46] as an ansatz

$$\sigma(x_1) = A\kappa^2 \frac{\mathrm{sn}(Ax_1,\kappa)\mathrm{cn}(Ax_1,\kappa)}{\mathrm{dn}(Ax_1,\kappa)} \,, \tag{4.47}$$

denoting Jacobi elliptical functions sn, $\mathrm{cn} = \sqrt{1-\mathrm{sn}^2}$ and $\mathrm{dn} = \sqrt{1-\kappa^2\mathrm{sn}^2}$ with modulus κ. Therefore, the space of physical values $(\hat{\mu}, \hat{T})$ is mapped onto the two-dimensional space in $(\kappa, A) \in (0,\ldots,1,0,\ldots,\infty)$ such that κ and A are analytic functions in $\hat{T}$ and $\hat{\mu}$. When permitting an inhomogeneous condensate $\hat{\sigma}(\hat{x}_1)$ its expansion is of the same form as the fermion fields (4.18, 4.17)

$$\hat{\sigma}(\hat{x}_1) = \frac{\sigma(x_1)}{\sigma_0} = \sum_{m=-M}^{M} \sigma_m \frac{e^{-i\hat{p}\hat{x}_1}}{\sqrt{\hat{L}_1}} \,, \quad \hat{p} = \frac{2\pi}{\hat{L}_1} m \,, \quad \sigma_{+m} = (\sigma_{-m})^* \,, \tag{4.48}$$

which admits $2M+1$ degrees of freedom because of the Hermiticity among coefficients. The accuracy in the expansion of both the fermionic fields and the condensate is not arbitrary and its relation is explained in Rem. 4.1.

Remark 4.1 *The oscillatory frequency of eigenfunctions of $Q^\dagger Q$ for low eigenvalues will be higher than those of the interpolating function $\sigma(x_1)$. Thus, the assumption of $M \ll N_1$ in comparison to fermionic fields becomes sufficient* [30]*. In turn, functions ψ^a must still be able to approximate the eigenfunctions such that the discrepancy in degrees of freedom is justified.*

Recall that the inhomogeneity of $\hat{\sigma}(\hat{x}_1)$ spoils the simple expansion of the determinant with ψ^a eigenfunctions of $Q^\dagger Q$. Proceeding from the generic case of the matrix elements (4.21) and after integration over $\hat{x}_0$, we arrive at the Hermitian matrix

$$\begin{aligned}\left\langle G_{\hat{k}_0,\hat{k}_1} | Q^\dagger Q | G_{\hat{k}'_0,\hat{k}'_1} \right\rangle = \frac{\delta_{\hat{k}_0,\hat{k}'_0}}{\hat{L}_1} \int d\hat{x}_1 \, e^{i\hat{k}_1\hat{x}_1} \\ \times \left(i\gamma_0\hat{k}_0 + i\gamma_1\hat{k}_1 + \gamma_0\hat{\mu} + \sum_{m=-M}^{M} \sigma_m \frac{e^{-i\hat{p}\hat{x}_1}}{\sqrt{\hat{L}_1}} \right) \\ \times \left(-i\gamma_0\hat{k}'_0 - i\gamma_1\hat{k}'_1 + \gamma_0\hat{\mu} + \sum_{m'=-M}^{M} \sigma_{m'} \frac{e^{-i\hat{p}'\hat{x}_1}}{\sqrt{\hat{L}_1}} \right) e^{-i\hat{k}'_1\hat{x}_1} \,. \end{aligned} \tag{4.49}$$

And its analytical evaluation at the delta functions

$$\begin{aligned}\left\langle G_{\hat{k}_0,\hat{k}_1} | Q^\dagger Q | G_{\hat{k}'_0,\hat{k}'_1} \right\rangle = \delta_{\hat{k}_0,\hat{k}'_0} \Bigg[\mathbf{I}_2 \delta_{\hat{k}_1,\hat{k}'_1} \left(\hat{k}_0^2 + \hat{k}_1^2 + \hat{\mu}^2 \right) + \frac{\mathbf{I}_2}{\hat{L}_1} \sum_{m=-M}^{M} \sigma_{\hat{p}(m)} \sigma_{\hat{k}_1 - \hat{k}'_1 - \hat{p}(m)} \\ + 2\hat{\mu} \left(\gamma_0 \frac{\sigma_{\hat{k}_1-\hat{k}'_1}}{\sqrt{\hat{L}_1}} - i\gamma_5 \hat{k}_1 \delta_{\hat{k}_1,\hat{k}'_1} \right) + \gamma_1 \frac{\sigma_{\hat{k}_1-\hat{k}'_1}}{\sqrt{\hat{L}_1}} \left(\hat{k}_1 - \hat{k}'_1 \right) \Bigg] \,. \end{aligned} \tag{4.50}$$

The sparsity of the matrix (4.50) is bounded by condensate's expansion coefficients σ_m and exhibits an overall block-diagonal structure. Thus, the determinant is split into a product over determinants of sub-matrices at equal zero momenta $\hat{k}_0 = \hat{k}'_0$ which becomes a sum over logarithms. The resulting matrices are computed using a LU-decomposition and are only dependent on the number of low lying spatial modes $(2N_1+1)$ and the two

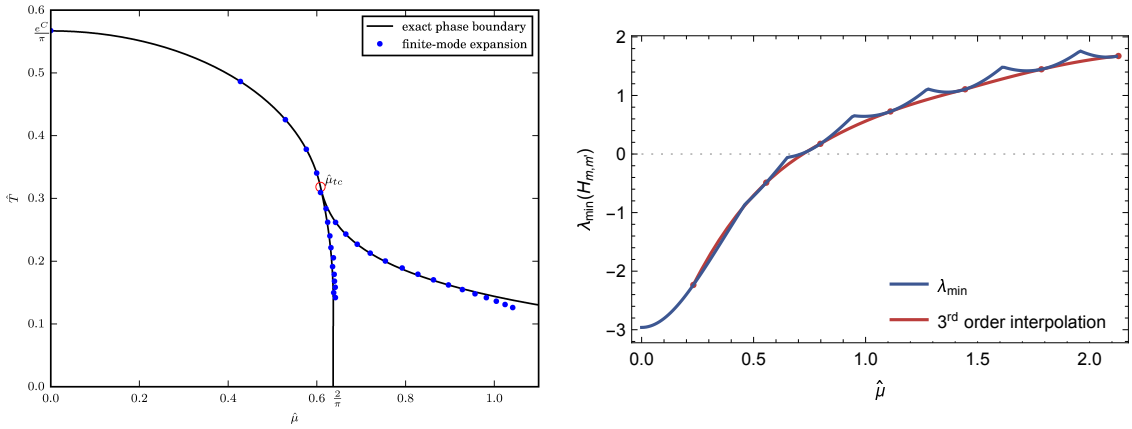

Fig. 4.10: Phase diagram of the mode expanded GN_2 model assuming an inhomogeneous condensate $\hat{\sigma} = \hat{\sigma}(\hat{x}_1)$ for (left) $N_1 = 30$ and (right) the corresponding lowest eigenvalue $\lambda_{\min}$ of the Hessian at $\hat{T} = 0.227$. The underlying line and the tri-critical point $\hat{\mu}_{tc}$ show analytic results obtained from [45].

Dirac spinor components in $(1+1)$ dimensions with $2(2N_1+1)$ elements.
The relaxation of translational invariance enables the minimisation of the effective action to be even lower than in the homogeneous cases before. Thus, we monitor the lowest eigenvalues of the Hessian matrix

$$H_{m,m'} = \frac{\partial}{\partial \Sigma_m}\frac{\partial}{\partial \Sigma_{m'}} fr S_{\text{eff}} N\Big|_{\hat{\sigma}=0} \tag{4.51}$$

assuming real $\Sigma_{2m} = \Re(\sigma_m)$ and imaginary $\Sigma_{2m+1} = \Im(\sigma_m)$ parts such that $0 < m, m' \leq M$. The analysis is set in the homogeneous vacuum $\hat{\sigma} = 0$ corresponding to $\sigma_m = 0 \,\forall\, m \in M$. After derivation w.r.t. the Σ_m and using *Jacobi's* formula

$$\delta \det A = \text{Tr}(\text{adj}(A)\delta A), \tag{4.52}$$

valid in arbitrary dimensions and where $\text{adj}(A) = (\det A)A^{-1}$ the Hessian amounts to

$$H_{m,m'} = \frac{2\hat{L}_0}{\lambda}\delta_{m,m'} + \sum_{n0=0}^{N_0-1} \text{Tr}\left[(Q^\dagger Q)^{-1}\frac{\partial^2(Q^\dagger Q)}{\partial\Sigma_m\partial\Sigma_{m'}} - (Q^\dagger Q)^{-1}\frac{\partial(Q^\dagger Q)}{\partial\Sigma_m}(Q^\dagger Q)^{-1}\frac{\partial(Q^\dagger Q)}{\partial\Sigma_{m'}}\right]_{\hat{\sigma}=0}. \tag{4.53}$$

The reason for inspecting the lowest eigenvalue of the Hessian in (4.51) is that a negative sign is associated with the possibility to further lower the effective action. In other words, the effective curvature in S_{eff} is also negative and subject to inhomogeneous perturbations. In the mode expansion the latter takes a simple representation and can be written in closed form demonstrated in App. B.4. Also there is no effect of whether we assume a real kink crystal with periodic (4.47) or anti-periodic (twisted kink) boundary conditions as the effect only results in a change of $\hat{k}_1$ which is not affecting the Hessian matrix.
The finite spatial extent $\hat{L}_1$, however, provokes a non-monotony of its lowest eigenvalue due to non-commensurability of the period of the analytic solution (4.47) and $\hat{L}_1$. In other words, if $\hat{L}_1$ is an exact multiple of the period of $\hat{\sigma}(\hat{x}_1)$ no finite size effects are observed. For all other values the lowest eigenvalue exhibits an oscillatory behaviour. To circumvent this obstacle, we use a third order interpolation by matching first derivates at the midpoints between kinks in Fig. 4.10. In the thermodynamic limit where the space dimension reaches infinity $\hat{L}_1 \to \infty$ the resulting curve becomes smooth. In accordance with Rem. 4.1 we pick $M = 5$ in (4.48) which is reflected in Fig. 4.10 as values of $\hat{\mu} \gtrsim 1.0$

yield unreliable results in the right phase boundary. The reason for this is that the amount of basis functions of the chiral condensate in (4.48) fails to approximate the increasing oscillations when advancing in chemical potential.

Anti-Periodic Condensate

Our assumptions where yet independent of the exact shape of the condensate. However, we were following the proposed twisted-kink ansatz from Sec. 4.1.1 with its implementation in the finite-mode approach.
In the light of the discrete γ_5-symmetry in (2.17) the ansatz was justified to topologically stabilise the single kink state and interpolate between the two vacua. Hence, an extra γ_5-matrix for the fermion fields at the spatial boundaries is introduced forcing the condensate to become anti-periodic. Similarly to the quantisation of the initial momenta $\hat{k}_\mu$ before (4.16), the condition on $\hat{k}_1$ now arises through demanding

$$e^{i\hat{k}_1\hat{x}_1} = \gamma_5 e^{i\hat{k}_1(\hat{x}_1+\hat{L}_1)} \,, \quad e^{i\hat{k}_1\hat{L}_1} = \gamma_5 e^{i2\pi n_1} \,. \tag{4.54}$$

In the chosen representation (cf. Sec. 2.1.1) this causes a mixing of the Dirac components of the spinors in the spatial momentum where the matrix logarithm gives $\log(\gamma_5) = \frac{\pi}{2}\gamma_5$ and

$$\hat{k}_1 = \frac{2\pi}{\hat{L}_1}\left(n_1\mathbf{I}_2 - \frac{i\gamma_5}{4}\right) \,, \tag{4.55}$$

is equipped with an additional γ_5-term. Besides, the expansion of the condensate (4.48) is adapted adequately to anti-periodicity

$$\hat{\sigma}(\hat{x}_1) = \frac{1}{\sqrt{\hat{L}_1}}\sum_{m=1}^{M}\left(\sigma_m e^{-i\hat{p}\hat{x}_1} + \sigma_{-m}e^{i\hat{p}\hat{x}_1}\right), \quad \sigma_{+m} = (\sigma_{-m})^* \,, \tag{4.56}$$

with $\hat{\sigma}(0) = \frac{1}{\sqrt{\hat{L}_1}}\sum_m(\sigma_m+\sigma_{-m}) = -\sigma(\hat{L}_1)$ which disposes of the constant σ_0 contribution in (4.48).

4.3.3 Plane waves and pseudoparticles

We explored the advantages of a finite-mode expansion over the formalism on the lattice in a reduced number of degrees of freedom M for higher approximation of the condensate. Let us now delve into the proposed pseudoparticle formalism introduced in Ch. 3. In comparison, both the mode and pseudoparticle expansion (3.1) appear to be quite similar. However, plane waves lack the most significant property of what defines a pseudoparticle: space-time localisation. In order to make the difference obvious, we revisit the $Q^\dagger Q$-regularisation (cf. Sec. 3.1.1) and define eigenvalues λ_n of eigenfunctions ψ_n

$$Q^\dagger Q\psi_n = \lambda_n\psi_n \,. \tag{4.57}$$

From the Hermiticity of $Q^\dagger Q$ (2.15), we know that these λ_n will be real-valued and positive definite. Typically the $V(\phi)$ term in the Q-operator (2.4) will be bounded such that for high λ_n plane waves of kind $\psi_n \approx \eta e^{ikx}$ will be approximate eigenfunctions of $Q^\dagger Q$ and the influence of the bosonic field ϕ is diminished. However, this does not hold for small eigenvalues λ_n. We will refer to them as *low lying eigenvalues* and assume that there exist only finitely many of them. Here the dependency on the bosonic fields ϕ will be high.
It would then be favourable to conduct the minimisation of the effective action based on a small number of these low lying eigenvalues. We will see that plane waves and pseudoparticles show approximately the same behaviour for small λ_n. In the convenient

diagonalised determinant of the fermion matrix (3.10) one can approximate low lying eigenfunctions using pseudoparticles

$$\tilde{G}_n \approx \psi_n \tag{4.58}$$

such that eigenvalues μ_n in (3.10) become

$$\mu_n = \left\langle \tilde{G}_n | Q^\dagger Q | \tilde{G}_n \right\rangle \approx \lambda_n \, . \tag{4.59}$$

For the fermion determinant in the $Q^\dagger Q$-regularisation this means that both the contribution of the pseudoparticles as well as the one from the plane waves are equivalent. Nevertheless, this changes for high λ_n where the pseudoparticle functions $\tilde{G}_n$ are now a superposition of the ψ_n and eigenvalues $\mu_n > \lambda_n$. The effect on the partition functions is negligible as the resulting contribution is merely an additional constant in the effective action that has no impact on the minimisation.
We can conclude that the discrepancies between the two approaches based on plane waves and pseudoparticles are mostly present for high eigenvalues (4.57). By choosing a set of pseudoparticles as a basis for the fermionic fields ψ^a and the condensate there might be a chance that we have better overlap with the operator $Q^\dagger Q$ and presumably less low lying eigenmodes are needed as conjectured from Fig. 3.2.

Following the usage of plane waves as pseudoparticles, we will now consider localised pseudoparticles, namely B-splines. This approach will bridge the discussion before migrating to Daubechies wavelets.

4.4 B-Spline Pseudoparticles

This first part of the section is devoted to the homogeneous chiral condensate similar to what we discussed on the lattice and for plane waves. Based on our specific choice of an anti-symmetric condensate (cf. Sec. 4.1.1) in the mode expansion, we use products of anti-periodic B-spline bases functions which is now achieved on simpler terms applying Eq. (3.17)

$$G_{k_0,k_1}(\hat{x}_0, \hat{x}_1) = N^{\mathrm{ap}}_{2,k_0}(\hat{x}_0) N^{\mathrm{ap}}_{2,k_1}(\hat{x}_1) \, , \tag{4.60}$$

where $k_0 = 0, \ldots, \hat{L}_0 - 1$ and $k_1 = 0, \ldots, \hat{L}_1 - 1$. Hatted quantities are kept dimensionless in terms of σ_0. The total volume of space-time $\hat{L}_0 \times \hat{L}_1$ is determined by integers $\hat{L}_0$ and $\hat{L}_1$ to ensure a uniform distribution of basis functions in space-time. The zero basis function $G_{0,0}$ is illustrated in Fig. 4.11. How is the choice of B-spline pseudoparticles justified on computational efficiency? On the one hand, the basis functions are piecewise polynomial and derivatives and overlap integrals in $\left\langle G_{k_0,k_1} | Q^\dagger Q | G_{k_0',k_1'} \right\rangle$ are known analytically from Eq. (3.19). On the other hand, their finite support renders the fermion matrix sparse. The most general effective action (3.13) in the pseudoparticle approach and $Q^\dagger Q$-regularisation for the discrete GN_2 model is

$$\frac{S_{\mathrm{eff}}}{N} = \frac{1}{2\lambda} \int d^2x \, \sigma^2 - \frac{1}{2} \log \left(\det \left\langle G_{k_0,k_1} | Q^\dagger Q | G_{k_0',k_1'} \right\rangle \right) \, , \tag{4.61}$$

which is independent of the choice of any pseudoparticle candidate. The regularised theory undergoes the same coupling renormalisation for λ at fixed $\hat{L}_{0c}$ as discussed on the lattice and for finite-modes (cf. Sec. 4.2.1). We show the scaling of the coupling dependent on the chiral condensate for different box sizes in Fig. 4.12. To compare the subsequent analysis, we fix a coupling constant $\lambda = 1.542$ and reproduce the homogeneous phase boundary by monitoring the effective action for the two solutions I,II. This survey was done for $\hat{L}_1 = 30$. For the spatially inhomogeneous case, we proceed similar as with the expansion in finite

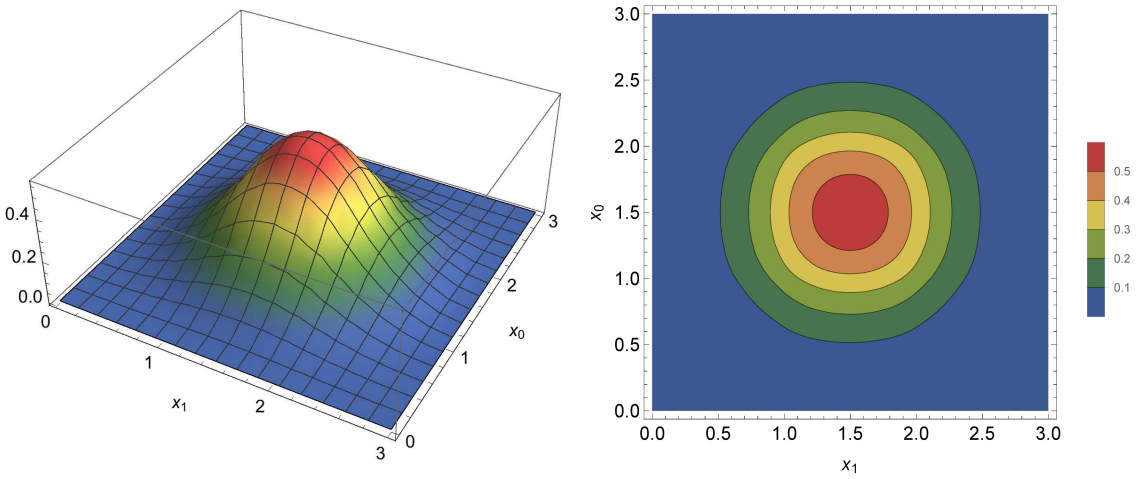

Fig. 4.11: B-spline pseudoparticle $G_{0,0}$ of degree $j = 2$ as a function of $(\hat{x}_0, \hat{x}_1)$ depicted as a (left) 3D Plot and (right) contour plot.

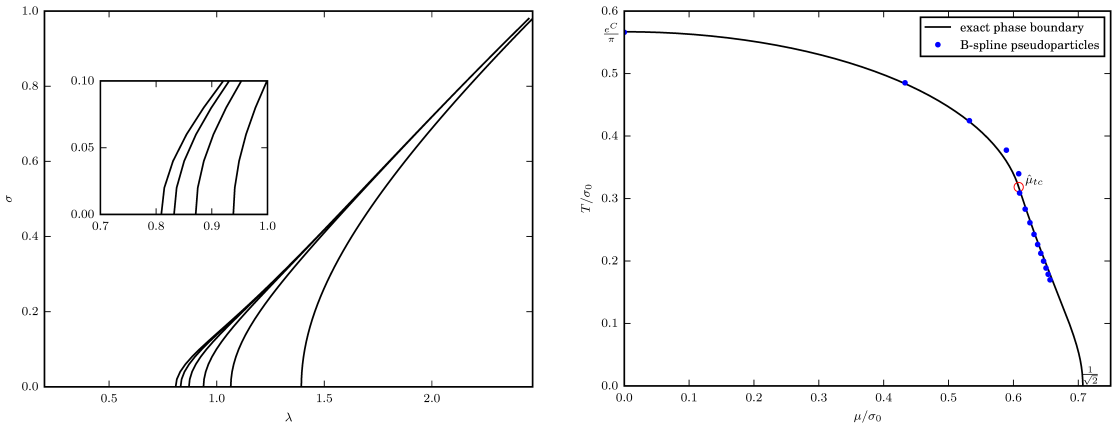

Fig. 4.12: (Right) B-spline pseudoparticle phase diagram of the GN_2-model assuming a homogeneous condensate $\hat{\sigma} = \text{const.}$ for $\hat{L}_1 = 30$ and (left) $\hat{\sigma}$ as a function of the coupling λ.

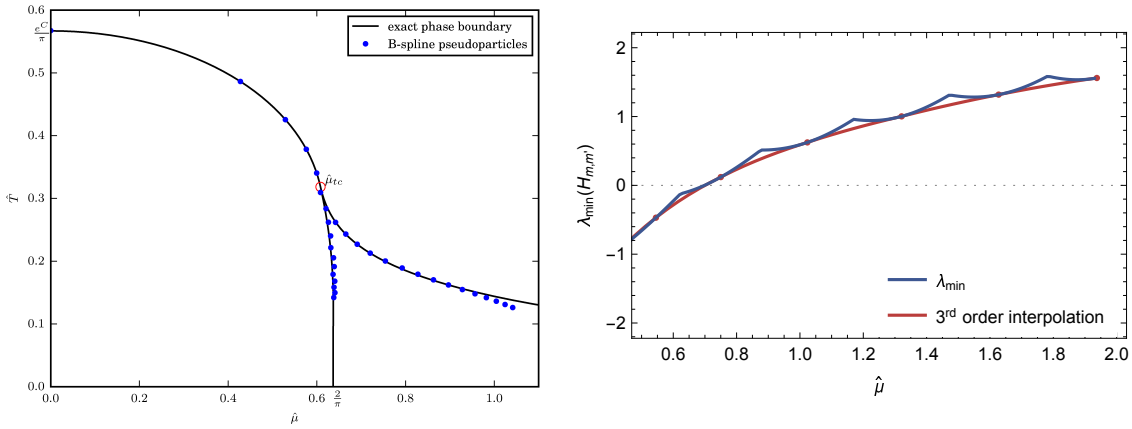

Fig. 4.13: Phase diagram of GN_2 model using B-spline pseudoparticles of degree $j = 2$ assuming an inhomogeneous condensate $\hat{\sigma} = \hat{\sigma}(\hat{x}_1)$ for (left) $\hat{L}_1 = 30$. (Right) The corresponding lowest eigenvalue $\lambda_{\min}$ of the Hessian at $\hat{T} = 0.227$. The underlying line and the tri-critical point $\hat{\mu}_{tc}$ show analytic results obtained from [45].

modes of the chiral condensate in (4.48). We restate the latter as a composition of anti-periodic B-spline pseudoparticles

$$\hat{\sigma}(\hat{x}_1) = \frac{\sigma(x_1)}{\sigma_0} = \sum_{m=0}^{\frac{hatL_1}{3}-1} \sigma_m N^{\text{ap}}_{2,m}(\hat{x}_1) \,. \tag{4.62}$$

employing a uniform knot vector in (3.16) with $m = 3$ of the type $t_k = k\frac{\hat{L}_1}{3} = 3k$ which requires 3 to be a divisor of $\hat{L}_1$. Notably the difference in number of degrees of freedom between fermionic fields ψ^a and the non-uniform condensate (4.62) is built on the same idea mentioned for the plane waves in Rem. 4.1. Thus, it becomes necessary to have a finer scale for fermionic fields in comparison to the condensate which in our case was chosen to be a factor of three with $M = \frac{\hat{L}_1}{3} - 1$ in Eq. (4.62).
With the value for the coupling from its renormalisation $\lambda = 1.542$, we continue to explore the phase boundary. The left phase boundary (I–III) is reconstructed by a brute-force minimisation of the action to retrieve the solution of S_{eff} in region III and find the point where the ordering changes. Furthermore, we inspect the right regime by computing the $Q^\dagger Q$-regularised Hessian in the homogeneous vacuum $\hat{\sigma} = 0$

$$H_{m,m'} = \frac{\partial}{\partial\sigma_m}\frac{\partial}{\partial\sigma_{m'}}\frac{S_{\text{eff}}}{N}\Big|_{\hat{\sigma}=0} \,, \tag{4.63}$$

based on the same arguments regarding instabilities from negative eigenvalues. The resulting plot of the lowest eigenvalue of the Hessian matrix (4.63) is shown in Fig. 4.13 where also the characteristic fringes due to finite size effects are present. We obtain reliable results up to a chemical potential of $\mu/\sigma_0 \approx 1.0$. However, for higher values of $\hat{\mu}$, we know that the frequency of the condensate $\hat{\sigma}(\hat{x}_1)$ increases as the quark density also increases. This reflects the fact that the condensate is no longer presentable with the corresponding order of approximation in (4.62) and one ha to use a higher number of degrees of freedom therein.
The scenario in Fig. 4.13 is very much in agreement with Fig. 4.10 using plane waves which suggests that both formalisms are identical in the infinite-volume continuum limit.
Compared to the finite-mode expansion there was no need to introduce a regulator so far i.e. a cut-off or a lattice spacing. Their use was implicit in the uniform distribution of basis functions on the computational domain $[0, \hat{L}_\mu - 1]$ and the corresponding knot vector.

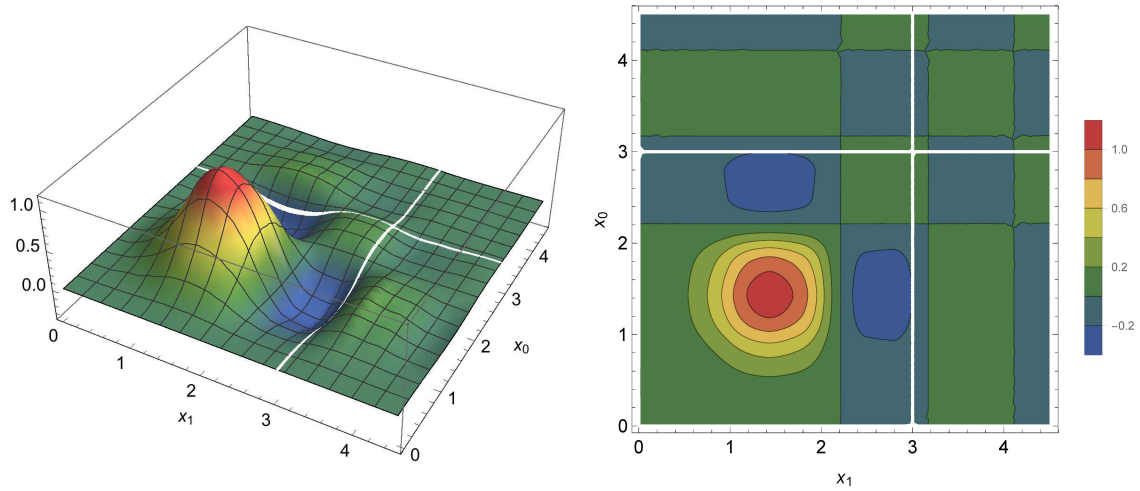

Fig. 4.14: Daubechies D_5 Wavelet pseudoparticle $G_{0,0}$ of genus $g = 5$ as a function of $(\hat{x}_0, \hat{x}_1)$ depicted as a (left) 3D Plot and (right) contour plot.

While in the mode expansion the oscillatory behaviour of $\hat{\sigma}(\hat{x}_1)$ was tuned by the number of low lying eigenmodes now the number of uniformly translated basis functions defines how accurately the function is encoded and therefore can exhibit higher frequencies.
This reasoning will become more apparent and controllable for the usage of wavelets where we encounter the additional dimension of scale j which will serve as the regulator.

4.5 Wavelet Pseudoparticles

At last, we consider the wavelet pseudoparticles as a regularisation prescription for the discrete GN_2 model. Driven by the analogy of higher dimensional wavelets in Eq. (3.45) the anti-periodic scaling functions from (3.78) simply factorise

$$G_{k_0,k_1}(\hat{x}_0, \hat{x}_1) W^{\text{ap}}_{j_0,k_0}(\hat{x}_0) W^{\text{ap}}_{j_0,k_1}(\hat{x}_1) \,, \tag{4.64}$$

with $j_0 = 0$. We present the zero translated Daubechies D_5 ($g = 5$) basis wavelet $G_{0,0}$ in Fig. 4.14 where we can clearly observe its finite support along a space-time extension of $[0, 2g-1] = [0, 9]$. On top to our motivation for B-splines choosing orthonormal finitely supported wavelets, the sparsity of the fermionic matrix $Q^\dagger Q$ increases. With anti-periodic boundary conditions of the analytic ansatz of the condensate (4.47), we examine the performance of the three proposed pseudoparticles: plane waves (actually not a pseudoparticle), B-splines and wavelets. These serve simultaneously as a basis for the $Q^\dagger Q$-matrix and the chiral condensate $\hat{\sigma}(\hat{x}_1)$. Especially for wavelets a mixing with other functional bases is not desirable as overlap derivative integrals (3.52) are only known among wavelet basis functions.
In this benchmark calculation, we approximate the interpolating $\hat{\sigma}(\hat{x}_1)$ at a given temperature $\hat{T} = 0.141$ nd chemical potential $\hat{\mu} = 0.65$ the kink regime close to the left phase boundary (I–III). To this end, we scan the error ϵ computed using the L^2-norm between the analytic solution and the primed $\hat{\sigma}'(\hat{x}_1)$ pseudoparticle expanded condensate

$$\epsilon = \|\hat{\sigma}(\hat{x}_1) - \hat{\sigma}'(\hat{x}_1)\|_{L^2} = \sqrt{\int_0^{L_1} |\hat{\sigma}(\hat{x}_1) - \hat{\sigma}'(\hat{x}_1)|^2} \,. \tag{4.65}$$

All three errors are reproduced in Fig. 4.15 show that the localised nature of pseudoparticles yields a higher convergence already. For the special case of $M = 10$ basis functions

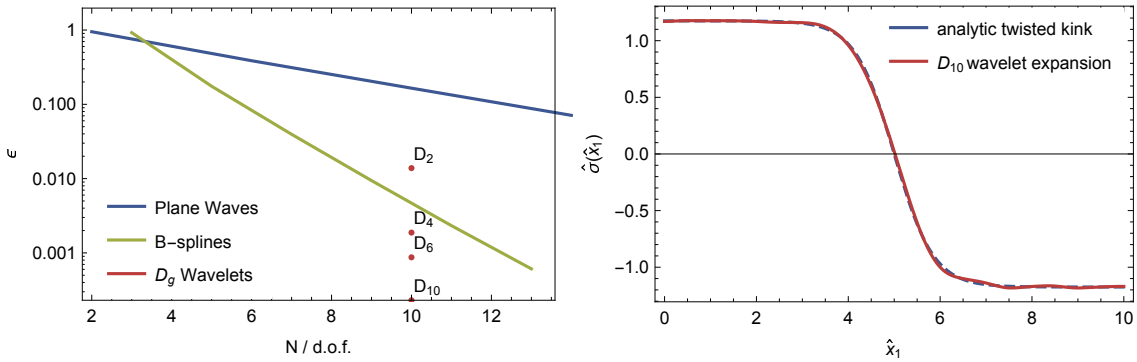

Fig. 4.15: $\hat{T} = 0.141$ and $\hat{\mu} = 0.65$. (Left) Error convergence from Eq. (4.65) of different pseudoparticle candidates towards and anti-periodic condensate for (green) B-splines, (blue) plane waves and (red) Daubechies D_g wavelets. (Right) D_{10} wavelet approximation of the analytic anti-symmetric kink solution [8].

(degrees of freedom) the wavelet approximation displays even higher accuracy with increased genus g at the cost of enhanced computational effort. In the same Figure 4.15, we show the approximation of the chiral condensate based on the Daubechies D_{10} wavelet family with uniform distribution at scale $j_0 = 0$.

4.5.1 The Regulator in the Wavelet Approach

Results from Fig. 4.15 tell us that there exists an explicit choice to regularise the theory based on two parameters, (i) the scale j and the (ii) genus g of the wavelet family. The latter is tantamount to the accuracy at every scale j. How is the difference between scales implemented following Rem. 4.1? For this thesis, we will basically restrict ourselves to pseudoparticle basis functions G_k for the fermionic fields ψ^a and the condensate, where both are of the same genus g. In other words, they have the same number of vanishing moments $\mathcal{N} = 2g$ in Eq. (3.23) i.e. level of approximation. The choice of j turns out to be more delicate. One aims for a condensate with less oscillatory frequency than the fermionic basis functions which means that we have to choose the scale j_σ for $\hat{\sigma}(\hat{x}_1)$ to be at least $j_\sigma < j_0$ where $j_0 = 0$ is the scale of the ψ^as. The great advantage from the wavelet orthonormality conditions (3.34) – (3.36) is the possibility to fully expand the condensate including even wavelet mother functions such that the decomposition becomes exact like in (3.40).
On the other hand, one still has to deal with derivative overlap coefficients which also become very simple as from (3.61) we know that only contributions from the same scale $j_\sigma = j_0$ are relevant. This reduces the computation significantly because the only surviving connection coefficients arise from overlaps $\langle \phi_{j_\sigma} \phi_{j_0} \rangle$ and $\langle \psi_{j_0} \phi_{j_0} \rangle$. For the remaining discussion, we will only regard scaling function contributions which we know well from Sec. 3.3.4

$$\hat{\sigma}(\hat{x}_1) = \frac{\sigma(x_1)}{\sigma_0} = \sum_{m=0}^{2^{j_\sigma} \hat{L}_1 - 1} \sigma_m W^{\text{ap}}_{j_\sigma, m}(\hat{x}_1). \tag{4.66}$$

Effectively the chiral condensate and the fermionic fields then differ by one scale $j_\sigma = j_0 - 1$. In pursuit of low computational cost, we are also employing Daubechies wavelets of genus $g = 3$ i.e. D_3 where the derivative couplings (3.52) are computed exactly. Note that this is the lowest order in g where this is possible (cf. Rem. 3.3).

Equipped with this knowledge, we tackle the homogeneous case with the effective action (4.61). This involves the usual coupling constant renormalisation based on the choice of the critical temperature, temporal box length $\hat{L}_{0c} = 5$, from which we check the dependence of the condensate on the coupling and compute the value of λ at the point where

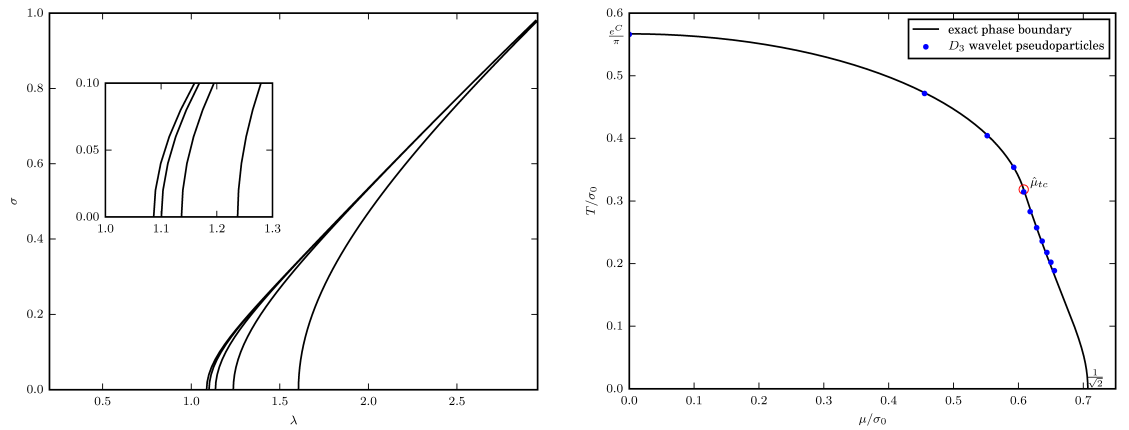

Fig. 4.16: (Right) D_3 wavelet pseudoparticle phase diagram of the GN-model assuming a homogeneous condensate $\hat{\sigma} = \text{const.}$ for $\hat{L}_1 = 30$ and (left) σ as a function of the coupling λ.

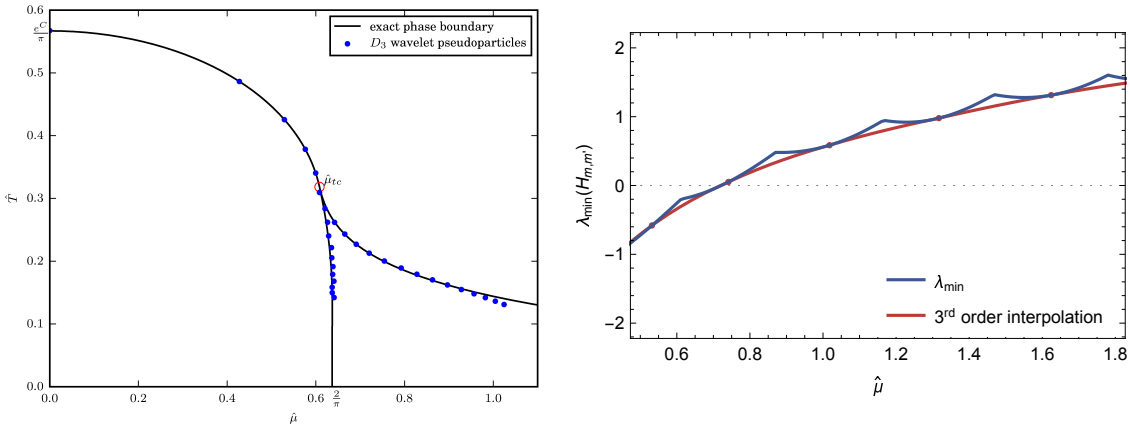

Fig. 4.17: Phase diagram of GN_2 model using Daubechies wavelet pseudoparticles D_3 of genus $g = 3$ assuming an inhomogeneous condensate $\hat{\sigma} = \hat{\sigma}(\hat{x}_1)$ for (left) $\hat{L}_1 = 30$ and (right) the corresponding lowest eigenvalue $\lambda_{\min}$ of the Hessian at $\hat{T} = 0.227$. The underlying line and the tri-critical point $\hat{\mu}_{tc}$ show analytic results obtained from [45].

σ just vanishes such that $\lambda = 1.616$. We present this procedure similar to the previous regularisation schemes in Fig. 4.16 with spatial box size of $\hat{L}_1 = 30$. The phase boundary between the homogeneously restored (I) and broken phase (II) results from checking again the ordering of the minimal effective actions along $\hat{\mu}$ and is illustrated in Fig. 4.16. Compared to the B-spline approach the Hermitian fermion matrix $Q^\dagger Q$ is much sparser because of the orthogonality of scaling functions (3.34) and the finitely supported derivative overlap coefficients (3.52). Therefore, the computational costs of the $\log\det Q^\dagger Q$ evaluation is of the same order as for the plane wave expansion. Additionally, results show higher agreement with the analytically obtained boundary [7] for even lower number of degrees of freedom.

Let us now consider the augmentation towards a non-uniform condensate $\hat{\sigma}(\hat{x}_1)$ with expansion from (4.66) in accordance to $\lambda = 1.616$ with the same procedure for solutions (I–III). Both boundaries in Fig. 4.17 are obtained through a straightforward minimisation of the effective action w.r.t. the condensate expansion coefficients σ_m in (4.66).

In comparison with plane waves in Fig. 4.13 and B-splines in Fig. 4.10 the obtained inhomogeneous phase boundary in the wavelet formalism Fig. 4.17 has better agreement in the tail of the boundary between (I) and (III) around $\hat{\mu} \approx 1.0$. This indicates a higher accuracy in the approximation of the condensate at higher oscillations when $\hat{\mu}$ increases.

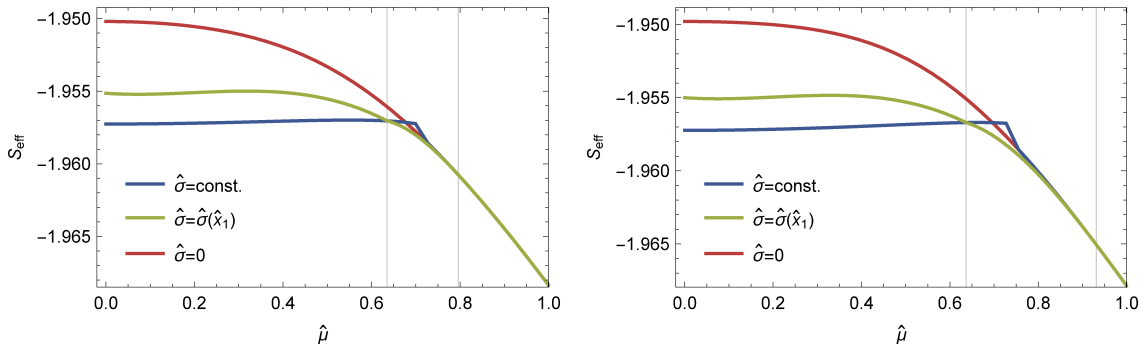

Fig. 4.18: Effective action $S_{\text{eff}}[\hat{\mu}]$ in the wavelet pseudoparticle approach of the GN_2 model with two changes in ordering at temperatures (left) $\hat{T} = 0.186$ and (right) $\hat{T} = 0.155$ for symmetric homogeneous $\hat{\sigma} = 0$, inhomogeneous $\hat{\sigma} = \hat{\sigma}(\hat{x}_1)$ and broken phase $\hat{\sigma} \neq 0$. Spatial extent $\hat{L}_1 = 30$.

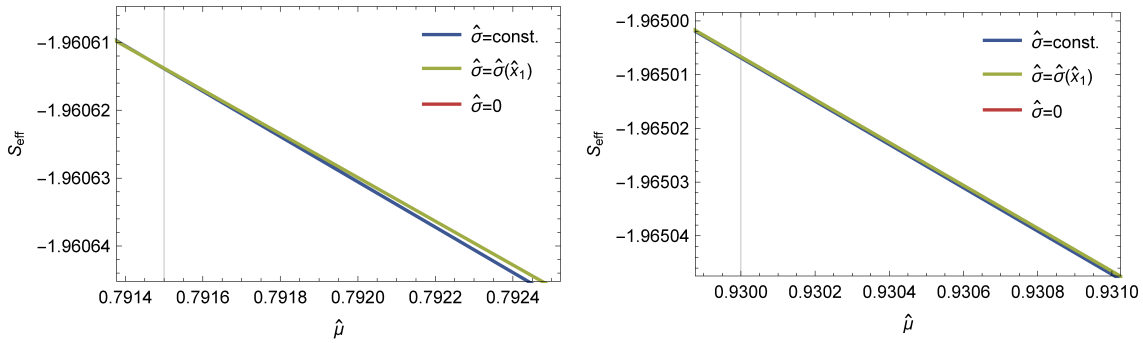

Fig. 4.19: Effective action $S_{\text{eff}}[\hat{\mu}]$ in the wavelet pseudoparticle approach at the right phase boundary with change in ordering at temperatures (left) $\hat{T} = 0.186$ and (right) $\hat{T} = 0.155$ for symmetric homogeneous $\hat{\sigma} = 0$, inhomogeneous $\hat{\sigma} = \hat{\sigma}(\hat{x}_1)$ and broken phase $\hat{\sigma} \neq 0$. Spatial extent $\hat{L}_1 = 30$.

To get an idea of the ordering of the effective actions along the direction of the chemical potential $\hat{\mu}$, we show the situation in Fig. 4.18 for the two cases of $\hat{T} = 0.186$ in the left panel and $\hat{T} = 0.155$ in the right panel. Contrarily to the mode expansion in Fig. 4.6, we encounter the inhomogeneous solution (green) that energetically stabilises the action in the region between the two grey horizontal lines which mark the resultant phase boundary for a given temperature $\hat{T}$. The second change of ordering marks a second order phase transition from the crystalline phase to the symmetrically restored phase which coincides with the right phase boundary in Fig. 4.17 (left).
The second phase transition at $\mu > \mu_{\text{tc}}$ is of special interest because we will also investigate it in higher dimensions and its existence is crucial for an emergent crystalline phase. Thus, we also show a zoomed version for the same two temperatures as before in Fig. 4.19. For lower temperatures the difference in the effective action becomes less apparent after the crossing of the solutions at $\hat{\mu}$ of the right phase boundar between (III) and (I). We also see that the homogeneous (blue) and symmetrically restored (red) solutions coincide while the inhomogeneous (green) curve is no longer energetically favoured.
For right part of the phase boundary, we also employ the optional inspection of the Hessian (4.63) for $\sigma_m = 0, \forall m$. Compared to the B-splines it is delicate to set up the functional determinant and the matrix elements $\left\langle G_{k_0,k_1}|Q^\dagger Q|G_{k_0',k_1'}\right\rangle$ because they are based on the derivative overlap integrals defined in Sec. 3.3.4. Similar to (4.21) we have

$$\left\langle G_{k_0,k_1}|Q^\dagger Q|G_{k_0',k_1'}\right\rangle = \int d\hat{x}_0 \int d\hat{x}_1\, W^{\text{ap}}_{j_0,k_0}(\hat{x}_0) W^{\text{ap}}_{j_0,k_1}(\hat{x}_1)$$

$$\times \left(\gamma_0 \hat{\partial}_0 + \gamma_1 \hat{\partial}_1 + \gamma_0 \hat{\mu} + \sum_{m=0}^{2^{j_\sigma} \hat{L}_1 - 1} \sigma_m W^{\mathrm{ap}}_{j_\sigma, m}(\hat{x}_1) \right)^\dagger$$
$$\times \left(\gamma_0 \hat{\partial}_0 + \gamma_1 \hat{\partial}_1 + \gamma_0 \hat{\mu} + \sum_{m'=0}^{2^{j_\sigma} \hat{L}_1 - 1} \sigma_{m'} W^{\mathrm{ap}}_{j_\sigma, m'}(\hat{x}_1) \right) W^{\mathrm{ap}}_{j_0, k_0'}(\hat{x}_0) W^{\mathrm{ap}}_{j_0, k_1'}(\hat{x}_1) \, . \tag{4.67}$$

The integration over $\hat{x}_0$ is independent of the expansion of the condensate due to factorisation of the pseudoparticle basis functions in (4.64). Therefore, we can carry out the calculation using integration by parts. The resulting expression is tantamount to the explicit calculation in the mode expansion

$$\begin{aligned} \left\langle G_{k_0,k_1} | Q^\dagger Q | G_{k_0',k_1'} \right\rangle = {} & \mathbf{I}_2 \delta_{k_1,k_1'} \Omega^{k_0}_{k_0'} \\ & + \delta_{k_0,k_0'} \Bigg[\mathbf{I}_2 \left(\Omega^{k_1}_{k_1'} + \hat{\mu}^2 \delta_{k_1,k_1'} + \sum_{m=0}^{2^{j_\sigma} \hat{L}_1 - 1} \sigma_m \sigma_{k_1 - k_1' - m} \right) \\ & + 2\hat{\mu} \left(\gamma_0 \sigma_{k_1 - k_1'} + \gamma_5 \Gamma^{k_1}_{k_1'} \right) \\ & + \gamma_1 \sum_{m=0}^{2^{j_\sigma} \hat{L}_1 - 1} \sigma_m \left(\Upsilon^{k_1}_{k_1' - m} + \Upsilon^{k_1' - m}_{k_1} \right) \Bigg] \, . \end{aligned} \tag{4.68}$$

The Υ^k_l in (4.68) correspond to the tri-linear connection coefficients presented in Eq. (3.58). They arise from integrals over derivates of the $Q^\dagger Q$ basis functions and the expanded condensate. We can identify the different terms from (4.50). The connection coefficients are implemented and calculated using the algorithm presented in Sec. 3.3.4. The arising curve of the lowest eigenvalue $\lambda_{\min}$ of the Hessian (4.63) in Fig. 4.17 (right) exhibits the usual fringes for small box sizes that eventually become smooth when taking the infinite-volume limit as discussed in Fig. 4.10 and 4.13.

4.5.2 An Unbiased Wavelet Algorithm

The application of wavelets as a pseudoparticle regularisation scheme of the discrete GN_2 model allowed to reproduce correctly the inhomogeneous phase boundary [8]. Following this idea, we propose to use the algorithm for higher dimensionality of the model i.e. the GN_4 model (cf. Sec. 2.1.4). The extension will be straightforward and no Pauli-Villars regularisation is needed as elucidated above. We follow the proposed algorithm from Sec. 4.1.1 consisting of

(i) Coupling constant renormalisation of λ

(ii) Choose anti-periodic solution $\hat{\sigma} = 0$, $\hat{\sigma} = \text{const.}$, $\hat{\sigma}(\hat{x}_1)$

(iii) Minimisation of the effective action S_{eff} with respect to expansion parameters of the condensate

(iv) Monitor S_{eff} along the chemical potential $\hat{\mu}$ or temperature $\hat{T}$

(v) Determination of the phase boundary from the change in ordering of S_{eff}

With the outline of an effective regularisation scheme in $(1+1)$ dimensions, we finally advance to a more QCD-like scenario in $(3+1)$ dimensions, the GN_4 model.

Chapter 5

Regularisation of the GN_4 Model

Succeeding the reproduction of the analytically known phase boundary of the GN_2 model as an exemplary introduction of the wavelet pseudoparticle regularisation, the following Chapter is dedicated to models in $(3+1)$ dimensions (cf. Ch. 2). We will first discuss the regularisation of the discrete GN_4 model using the algorithm proposed in the preceding Chapter in order to obtain its phase boundary.

5.1 Phase Diagram of the GN_4 Model

Our choice of ansatz in the expansion of the inhomogeneous condensate is motivated from its equivalent in $(1+1)d$ in (4.66). Furthermore, the chiral condensate $\sigma(\mathbf{x})$ depends only on the spatial coordinates $\mathbf{x} = (x_1, x_2, x_3)$. We are then interested in the energetically most favourable field configuration. It has been conjectured that ansätze consisting of more than one spatial coordinate are not always favoured [47, 25]. Nevertheless, we restrict ourselves to the additional assumption of a diagonally inhomogeneous condensate in all spatial directions

$$\sigma(x_1, x_2, x_3) = \sum_{m=0}^{2^{j_\sigma} L_3 - 1} \sigma_m W^{\mathrm{ap}}_{j_\sigma, m}(x_1) W^{\mathrm{ap}}_{j_\sigma, m}(x_2) W^{\mathrm{ap}}_{j_\sigma, m}(x_3), \tag{5.1}$$

with equal extent $L_1 = L_2 = L_3$. Note, that off-diagonal parts of the condensate are neglected in the expansion (5.1). The field configuration that dominates the partition function $\mathcal{Z}$ will therefore yield an effective action S_{eff} that will be lower than in the general case where $\sigma_m = \sigma_{k,l,m}$. The factorisation of the wavelet basis functions in (5.1) signifies that only connection coefficients up to the trilinear form of (3.58) are needed.
As the phase boundary in $(3+1)d$ is analytically unknown the goal will be to check the stability of the three dimensional crystal phase with our wavelet-product ansatz. This means, we need to examine the minimised effective action for all three solutions over the whole regime of μ and infer its ordering for $\mu \to \infty$. The corresponding effective action is equivalent to (4.61) in $(3+1)$ dimensions

$$\frac{S_{\mathrm{eff}}}{N} = \frac{1}{2\lambda} \int d^4x \; \sigma^2 - \frac{1}{2} \log \left(\det \left\langle G_{k_0,k_1,k_2,k_3} | Q^\dagger Q | G_{k'_0,k'_1,k'_2,k'_3} \right\rangle \right) , \tag{5.2}$$

with anti-periodic wavelet scaling basis functions $G_{k_0,k_1,k_2,k_3} = G_{k_0} G_{k_1} G_{k_2} G_{k_3}$ motivated from extension of the factorisation in Eq. (3.45) to four space-time dimensions

$$G_{k_0,k_1,k_2,k_3}(x_0, x_1, x_2, x_3) = W^{\mathrm{ap}}_{j_0,k_0}(x_0) W^{\mathrm{ap}}_{j_0,k_1}(x_1) W^{\mathrm{ap}}_{j_0,k_2}(x_2) W^{\mathrm{ap}}_{j_0,k_3}(x_3). \tag{5.3}$$

As for the $(1+1)d$ case the scale of the fermion fields is $j_0 = 0$. We consider the algorithm in Sec. 4.5.2 starting with the coupling constant (renormalisation) $\lambda = 1.156$ at spatial

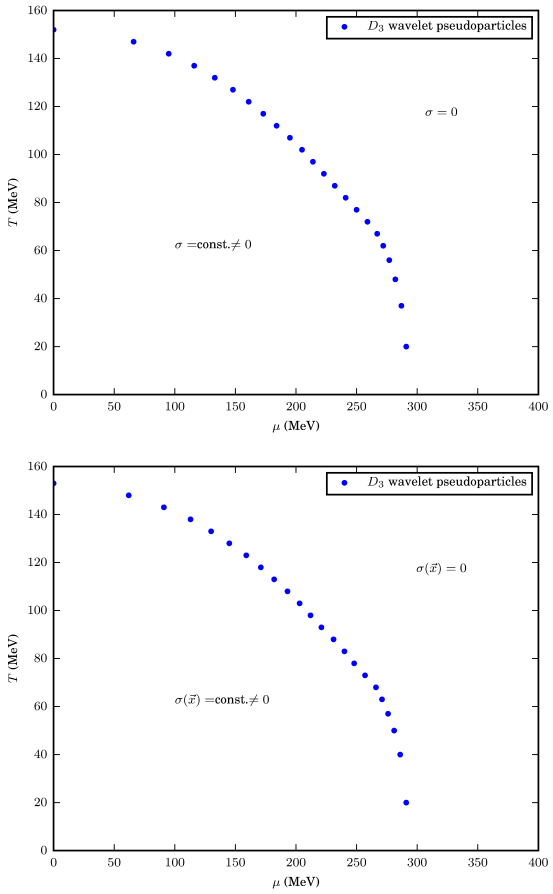

Fig. 5.1: Phase diagram of discrete GN_4 model using Daubechies wavelet pseudoparticles D_3 of genus $g = 3$ assuming (left) a homogeneous condensate and (right) an inhomogeneous condensate $\sigma = \sigma(\mathbf{x})$ in (5.1) for $L_1 = L_2 = L_3 = 50$.

box size $L_3 = 50$ and critical temporal extension $L_{0c} = 5$. With these parameters and the regulator in wavelet approach $j_\sigma = j_0 - 1$ we can minimise the effective action (5.2) w.r.t. the coefficients σ_m in the decomposition (5.1).
The effective action evaluated at this solution (III) is compared with the two other solutions akin to the procedure in two dimensions. In Fig. 5.1 we show the resulting phase boundary between solutions (I) and (II) in the left panel and between (I) and (III) in the right panel. The shape resembles the homogeneous phase diagram of the $(1+1)d$ discrete GN_2 model with no indication of a third phase right to the critical chemical potential μ_c.
The study is again based on the inspection of the ordering of the free energy for all three solutions (I–III) as illustrated in Fig. 5.2 for two values of the chemical potential namely $\mu = 320$ MeV (left) and $\mu = 600$ MeV (right). We observe that the $\sigma = 0$ solution is favoured for all temperatures while the effective action associated with $\sigma(\mathbf{x})$ is always higher. Technically this is analogous to Fig. 4.18. This would rule out an energetically favourable crystal phase for intermediate chemical potential similar to the discrete-symmetric GN_2 model given the specific but unbiased ansatz in (5.1).
To justify this conjecture, we monitor the difference of the effective actions ΔS_{eff} for the two solutions of inhomogeneous $\sigma(\mathbf{x})$ and zero condensate at $T = 20$ MeV in the region right of the critical chemical potential $(\mu_c, T = 0)$ as plotted in Fig. 5.3. The resultant behaviour shows an increasing discrepancy for higher μ such that the solution in the symmetrically restored phase becomes more and more energetically stable. Effectively the solutions drift apart when refining the ansatz of the condensate and including more degrees

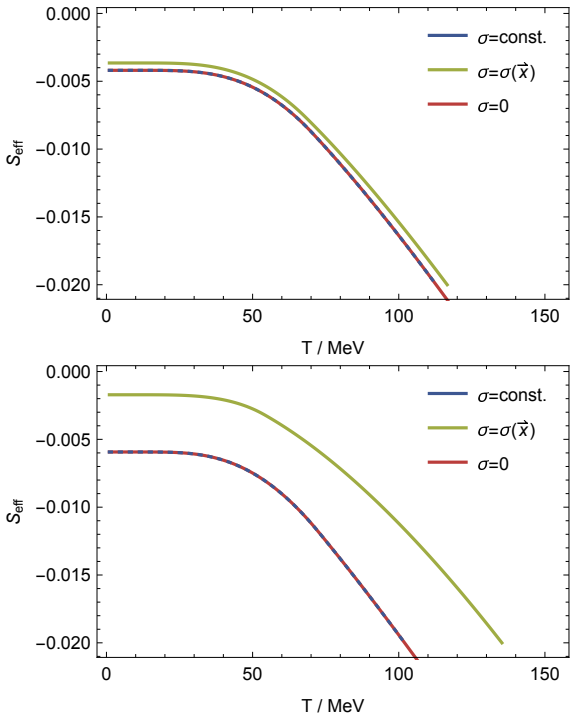

Fig. 5.2: Ordering of the effective action $S_{\text{eff}}[T]$ in the wavelet pseudoparticle approach of the GN$_4$ model at two values of the chemical potential (left) $\mu = 320$ MeV and (right) $\mu = 600$ MeV for symmetric homogeneous $\sigma = 0$, inhomogeneous $\sigma = \sigma(\mathbf{x})$ and broken phase $\sigma \neq 0$. Spatial extent $L_1 = L_3 = L_3 = 50$.

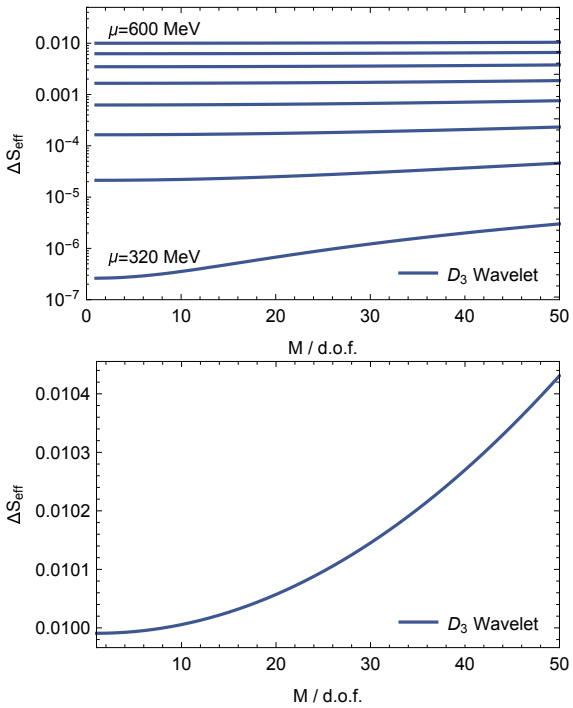

Fig. 5.3: Free energy difference ΔS_{eff} between the inhomogeneous solution and symmetrically restored phase at $T = 20$ MeV and different values of μ for (left) $\mu = [320, 600]$ MeV and (right) $\mu = 600$ MeV using a D_3 Daubechies wavelet family for different number of expansion terms in Eq. (5.1).

of freedom M in the expansion. For the prevailing parameters, we found no evidence of the proposed crystal phase and could rule out an emergent *inhomogeneous island* [10] for regions of high μ.

5.1.1 Implications on the NJL model

For the NJL model the condensate can rotate as a function of spatial coordinates [5]. Our simple ansatz of a chirally twisted kink solution motivated in Sec. 4.1.1 might not hold anymore as it was specifically tailored for a Z_2-symmetry. Therefore, one might use a different ansatz which is still more general than a CDW. Such a choice would be using periodic boundary conditions for all three spatial directions. Also here one can obviate the renormalisation by only looking at the minimal value of the corresponding effective action (2.58) in the wavelet formalism. Also the pion-like field combinations in the Lagrangian density Eq. (2.53) will condense because the NJL model is a quark-meson model. This yields another three additional condensates that enter the minimisation accordingly to the proposed wavelet based algorithm.

5.2 Summary and Conclusion

This thesis is merely an exploratory search for a stable unbiased determination of phase boundaries of effective quark-based QCD models. However, we have not yet exploited the full extent of the wavelet pseudoparticle approach. One possibility would be a translationally invariant condensate where the expansion coefficients also factorise $\sigma_m \to \sigma_{k,l,m}$. Now the sum in (5.1) individually extends over all three spatial directions. Hence, the condensate becomes

$$\sigma(x_1, x_2, x_3) = \sum_{k,l,m=0}^{2^{j_\sigma} L_3 - 1} \sigma_{k,l,m} W^{\mathrm{ap}}_{j_\sigma,k}(x_1) W^{\mathrm{ap}}_{j_\sigma,l}(x_2) W^{\mathrm{ap}}_{j_\sigma,m}(x_3), \tag{5.4}$$

employing $L_1 = L_2 = L_3$. Possibly this change permits extra inhomogeneous perturbations with a decreased contribution from the diagonal coefficients $\sigma_{k,l,m}$ where $k = l = m$ as off-diagonal terms were not allowed during the previous calculation. This could possibly produce an effective action that is energetically favoured at high densities. Optionally to the account of Sec. 4.1.1 the condensate in $(3+1)d$ can be decomposed using a cubic-centered crystal i.e. a periodic function $\hat{\sigma}$ that has a negative sign at the midpoint of the lattice

$$\begin{aligned} \sigma(x_1, x_2, x_3) &= \hat{\sigma}(x_1, x_2, x_3) - \hat{\sigma}\left(x_1 + \tfrac{L_3}{2}, x_2 + \tfrac{L_3}{2}, x_3 + \tfrac{L_3}{2}\right) \\ \hat{\sigma}(x_1 + L_3, x_2, x_3) &= \hat{\sigma}(x_1, x_2, x_3)\ . \end{aligned} \tag{5.5}$$

In subsequent analyses this choice might eventually become more stable and is in favour of the crystal phase which was ruled out for the twisted kink-crystal ansatz above.

The next step is to apply the pseudoparticle approach to QCD. Of course, instead of using a large number of orthonormal wavelet pseudoparticles, as we have implemented them above, the aim is to reduce the functional basis further and restrict ourselves to physically relevant fermionic pseudoparticles. Those could be basis functions that have a significant higher overlap with the QCD Dirac operator which could be achieved by constructing wavelets that are specifically generated for the functional form we want to approximate. In this sense wavelets can also be used for gauge fields [28].

Chapter 6

Summary and Outlook

In this thesis we presented a preliminary study of the pseudoparticle approach based on wavelets as a regularisation scheme for QCD effective models in order to numerically determine the phase boundary. The algorithm was developed for the discrete Gross-Neveu model in $(1+1)$ dimensions in order to reproduce analytically known results both in the homogeneous [7] and the inhomogeneous case [8] illustrated in Fig. 4.16 and 4.17 at discrete spatial box sizes of $\hat{L}_1 = 30$. The convergence for wavelet pseudoparticles appears to be much higher at comparable degrees of freedom and computational costs in comparison to exploratory research using plane-waves [10]. One explanation is the increased overlap with the $Q^\dagger Q$-operator which would allow to further decrease the number of basis functions in future investigations.
The pivotal point of our analysis is to augment the approach to $(3+1)$ dimensions regarding the discrete GN_4 model. This scenario is especially interesting because a plethora of reviews [10, 25, 48] conjectures a similar crystal phase for quark-meson models as in $(1+1)$ dimensions. By using a condensate ansatz (5.1) that only depends on diagonal expansion terms $\sigma_{k,l,m} = \sigma_m$, we were not able to find evidence of such an emergent crystalline phase. Furthermore, we checked the stability of the energetic favourability of the restored phase at intermediate chemical potential as seen in Fig. 5.3. The free energy advantage of the symmetric phase increases when reaching regimes of higher μ which implies that no additional phase except the homogeneous and restored one should be present given our initial choice of ansatz.
The attempt of a detailed comparison of the computational efficiency of the wavelet pseudoparticle approach regarding other studies would require calculations of the exact same quantities within the same model. Throughout our study, we mostly considered rather small spatial box sizes $\hat{L}_1 \sim \mathcal{O}(10)$ such that all approaches for the $(1+1)$ dimensional survey in Ch. 4 were tractable using a desktop machine.
Following our analysis, I devise to study the model in the most general case – a fully spatially inhomogeneous condensate (5.4) which could have additional contributions that reduce the effective action further. Similarly this could also be valid when employing a cubic-centered crystal roposed in Eq. (5.5).
One could also broaden the concept of wavelet pseudoparticles by applying so-called *curvelets* [49] which are a higher dimensional generalisation for a functional basis.

6.1 Applications of Wavelets in Field Theories

Based on results in this thesis the applicability of wavelets appears far from fully uncovered and remains worthy of further investigations.
Wavelet expansions bear high potential in field theories because, as we have seen, additionally to their space-time coordinates also a scale index is included. This allows to set

a scale of measurement to obviate possible divergences in Green's functions. Also their versatility could be useful to compute fixed points of renormalisation flows [**?**]. Especially for field theories with gauge fields it would be interesting to include local gauge invariance using covariant derivatives at all scales. For wavelets this was shown in [50], however, for non-local individual basis functions.
The possibility to explicitly control the scaling prompted other interesting projects in order to exploit this extra dimension. One can for example construct QFTs based on a connection between the holographic principle and tensor networks utilising a so-called *Exact Holographic Mapping* (EHM) [51, 52]. In pioneering research in this field a $(1+1)d$ scalar bosonic QFT with central charge $c = 1$ was mapped from the boundary to a bulk with an emergent AdS geometry therein. The authors were able to generalise the EHM from the simple Haar wavelet to the whole family of Daubechies wavelets. This gives room for studies of how long range entanglement quantities such as the central charge are dependent on the emergent dual geometry in the bulk. Possibly an interesting research topic would be to investigate conformal field theories with central charge different from one, $c \neq 1$, i.e. critical Ising- and the 3-state Potts models. Also the question, if it is possible to extend the procedure to gauge theories on the boundary has not been answered so far. Lastly, the mentioned wavelet connection to tensor networks in the EHM seems very promising. While in this thesis we mostly focus on the explicit family of Daubechies wavelets, there might be a whole different angle to it. Thus, it was conjectured that an arbitrary wavelet family could potentially be constructed from a *universal* nearest neighbour circuit. An example are so-called binary *Multi-Scale Renormalisation Ansatz* (MERA) circuits [53]. Eventually, this would yield a wide range of new wavelet classes reinforcing the interwoven nature of wavelets in MERA. Based on these initial ideas, future studies of the holographic principle in the tensor network formalism via wavelets could give deeper insight on the connection between these disciplines.

Appendix A

Quark-Based Models

A.1 Hubbard-Stratonovich Transformation

In general, the Hubbard-Stratonovich transformation [54] is useful when dealing with theories that exhibit interacting terms like for example the four-fermion coupling in the GN and NJL models from Ch. 2. The principle of the transformation is simply based on the integral identity

$$\int_{\mathbb{R}} dx \, \exp\left\{-\pi x^2 - 2\pi^{\frac{1}{2}} a x\right\} = \exp\left\{a^2\right\} \ , \tag{A.1}$$

with $a > 0$. Its implementation in the partition function is not straightforward if non-commuting operators are involved. Quadratic interacting operators in the exponent of the partition function $\mathcal{Z}$ (2.7) are eventually traded for a trace over non-interacting fields.

A.2 Feynman Rules of the GN_2 Model

We consider the modified Lagrangian after the Hubbard-Stratonovich transformation (2.11) which then yields the Feynman rules for both the fermion field ψ as well as the bosonic auxiliary field σ. The latter is represented as dashed lines sketched in Fig. A.1.

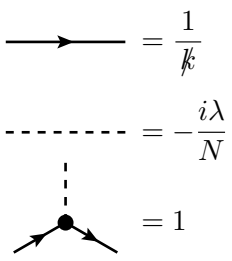

Fig. A.1: Feynman rules for the Gross-Neveu model in $(1+1)$ dimensions.

Appendix B

$Q^\dagger Q$-Regularisation

B.1 B-spline Derivatives

To prove the claim (3.19) for derivatives of B-spline functions, we first inspect the case with degree $N_{0,k}$ in (3.14). Here all derivatives are zero because of the constant B-splines on the subintervals. Therefore, the claim holds for $j = 0$. Let us assume that the derivation prescription (3.19) is also true for $j = 1, 2, \ldots, n$. We are investigating the formula for $j = n + 1$ such that

$$\partial_x N_{n+1,k}(x) = \partial_x \left(\frac{x - t_k}{t_{k+j+1} - t_k} N_{j,k}(x) + \frac{t_{k+j+2} - x}{t_{k+j+2} - t_{k+1}} N_{j,k+1}(x) \right) . \tag{B.1}$$

After differentiation and using the product rule, we encounter further derivatives of of lower degree $j = n$

$$\begin{aligned} \partial_x N_{n+1,k}(x) = {} & \frac{x - t_k}{t_{k+j+1} - t_k} \partial_x N_{j,k}(x) + \frac{1}{t_{k+j+1} - t_j} N_{j,k}(x) \\ & + \frac{t_{k+j+2} - x}{t_{k+j+2} - t_{k+1}} \partial_x N_{j,k+1}(x) - \frac{1}{t_{k+j+2} - t_{k+1}} N_{j,k+1}(x) . \end{aligned} \tag{B.2}$$

With the premise (3.19), we already know the expression for derivatives at degree $j = n$

$$\partial_x N_{j,k+1}(x) = \frac{j}{t_{k+j+1} - t_{k+1}} N_{j-1,k+1}(x) - \frac{j}{t_{k+j+2} - t_{k+2}} N_{j-1,k+2}(x) \tag{B.3}$$

$$\partial_x N_{j,k}(x) = \frac{j}{t_{k+j} - t_k} N_{j-1,k}(x) - \frac{j}{t_{k+j+1} - t_{k+1}} N_{j-1,k+1}(x) . \tag{B.4}$$

After inserting these expressions into (B.2) and some algebra, we modify the resultant expression into the form of (3.19) at $j = n + 1$

$$\partial_x N_{j+1,k}(x) = \frac{j+1}{t_{k+j+1} - t_k} N_{j+1,k}(x) - \frac{j+1}{t_{k+j+2} - t_{k+1}} N_{j,k+1}(x) , \tag{B.5}$$

which proves the claim of B-spline differentiation in (3.19).

B.2 Wavelet Moments

Latto et al. [37] derive a formula to compute the moments presented in Eq. (3.50)

$$M_k^p = \int_{\mathbb{R}} x^p \phi_k(x) , \quad p, k \in \mathbb{Z} \tag{B.6}$$

by induction on k with the wavelet filter coefficients $\{a_k\}$. From Remark 3.2, we already know that $M_k^0 = 1$ so that in succession, we infer conditions on the M_0^p under the usage of the dilation equation (3.48)

$$\begin{aligned} M_0^p &= \int_{\mathbb{R}} x^p \phi(x)\, dx \\ &= \sqrt{2} \sum_{i=0}^{N-1} a_i \int_{\mathbb{R}} x^p \phi_l(2x)\, dx \\ &= 2^{\frac{1-2p-2}{2}} \sum_{i=0}^{N-1} a_i \int_{\mathbb{R}} x^p \phi_i(x)\, dx = 2^{\frac{1-2p-2}{2}} \sum_{i=0}^{N-1} a_i M_i^p \,. \end{aligned} \tag{B.7}$$

The r.h.s. of Eq. (B.7) is restated when expressing shifted momenta $x \mapsto x + k$ at the same degree p

$$\begin{aligned} M_k^p &= \int_{\mathbb{R}} (x+k)^p \phi_k(x)\, dx \\ &= \sum_{l=0}^{p} \binom{p}{l} k^{p-l} \int_{\mathbb{R}} x^l \phi(x)\, dx = \sum_{l=0}^{p} \binom{p}{l} k^{p-l} M_0^l \,. \end{aligned} \tag{B.8}$$

and reinsertion renders M_0^p to only rely upon different degrees without translation k using Eq. (3.49)

$$\begin{aligned} M_0^p &= 2^{\frac{1-2p-2}{2}} \sum_{i=0}^{N-1} a_i \sum_{m=0}^{p} \binom{p}{m} i^{p-m} M_0^m \\ &= 2^{\frac{1-2p-2}{2}} \sum_{n=0}^{p-1} \binom{p}{m} M_0^m \sum_{i=0}^{N-1} a_i i^{p-m} + 2^{\frac{1-2p-2}{2}} \sum_{i=0}^{N-1} a_i \\ &= \frac{\sqrt{2}}{2(2^p-1)} \sum_{m=0}^{p-1} \binom{p}{m} M_0^m \sum_{i=0}^{N-1} a_i i^{p-m} \,. \end{aligned} \tag{B.9}$$

Eventually all the shifted momenta are recovered in the combination of (B.8) and (B.9)

$$M_k^p = \frac{\sqrt{2}}{2(2^p-1)} \sum_{l=0}^{p} \binom{p}{l} k^{p-l} \sum_{m=0}^{l-1} \binom{l}{m} M_0^m \left(\sum_{i=0}^{N-1} a_i i^{l-m} \right) \,. \tag{B.10}$$

B.3 Wavelet Moments Coefficients

With the solution of the proposition in [38] fundamental connection coefficients of the first derivative order $\Gamma = \{\Gamma_l^0\}_{l=1}^{\mathcal{N}-2}$ from Eq. (3.55) of Daubechies wavelets with $\mathcal{N} = 2g$ are given by their genus. Note that $\Gamma_0^0 = 0$.

$$g = 2, \quad \Gamma = \left\{-\tfrac{2}{3}, \tfrac{1}{12}\right\} \tag{B.11}$$

$$g = 3, \quad \Gamma = \left\{-\tfrac{272}{365}, \tfrac{53}{365}, \tfrac{16}{1095}, -\tfrac{1}{2920}\right\} \tag{B.12}$$

$$g = 4, \quad \Gamma = \left\{-\tfrac{39296}{49553}, \tfrac{76113}{396424}, -\tfrac{1664}{49553}, \tfrac{2645}{1189272}, \tfrac{128}{743295}, -\tfrac{1}{1189272}\right\} \tag{B.13}$$

$$\begin{aligned} g = 5, \quad \Gamma = \Big\{&-\tfrac{957310976}{1159104017}, \tfrac{265226398}{1159104017}, -\tfrac{735232}{13780629}, \tfrac{17297069}{2318208034}, \\ &-\tfrac{1386496}{5795520085}, -\tfrac{563818}{10431936153}, -\tfrac{2048}{8113728119}, -\tfrac{5}{18545664272}\Big\} \end{aligned} \tag{B.14}$$

The second order derivative two factor connection coefficients $\{\Omega_l^0[g]\}_{k=1}^{\mathcal{N}-2}$ from (3.57) have been calculated according to the algorithm explained in Sec. 3.3.4. We present them for different genera $g = 3, \ldots, 5$ in Tab. B.1. Also the first order trilinear derivative overlap coefficients $\{\Upsilon_l^k\}_{k,l=1}^{\mathcal{N}-2}$ defined in (3.58) are computed exemplarily for genus $g = 3$ listed in Tab. B.2.

Tab. B.1: The two-factor fundamental connection coefficients (3.57) for $\{\Omega_l^0[g]\}_{k=1}^{\mathcal{N}-2}$ for Daubechies wavelets with $\mathcal{N} = 2g$ and genus $g = 3, \ldots, 5$.

l	$\Omega_l[3]$	$\Omega_l[4]$	$\Omega_l[5]$
0	−5.2678571429	−4.1659736407	−3.8349943138
1	3.3904761905	2.6420702081	2.4147903512
2	−0.8761904762	−0.6978691044	−0.6495021900
3	0.1142857143	0.1509728996	0.1809535501
4	0.0053571429	−0.0105727278	−0.0299079804
5	0.0000000000	−0.0016303769	0.0007946206
6	0.0000000000	0.0000159216	0.0003671454
7	0.0000000000	0.0000000000	0.0000016565
8	0.0000000000	0.0000000000	0.0000000035

Tab. B.2: The three-factor fundamental connection coefficients (3.58) for $\{\Upsilon_l^k\}_{k,l=1}^{\mathcal{N}-2}$ for Daubechies wavelets with $\mathcal{N} = 2g$ and genus $g = 3$.

k	Υ^k_{-4}	Υ^k_{-3}	Υ^k_{-2}	Υ^k_{-1}	Υ^k_{0}
−4	0.0000015241	0.0000329020	−0.0001358901	0.0004451594	−0.0000012296
−3	0.0000329020	0.0014522972	−0.0061773222	0.0204916885	−0.0011881821
−2	−0.0001358901	−0.0061773222	0.0329026887	−0.1252725459	−0.0467741857
−1	0.0004451594	0.0204916885	−0.1252725459	0.4968918011	0.3135877530
0	−0.0000012296	−0.0011881821	−0.0467741857	0.3135877530	0.0000000000
1	0.0000000000	0.0000004887	0.0002498264	0.0378102693	−0.2484459006
2	0.0000000000	0.0000000000	0.0000019494	0.0012518005	−0.0164513443
3	0.0000000000	0.0000000000	0.0000000000	−0.0000004464	−0.0007261486
4	0.0000000000	0.0000000000	0.0000000000	0.0000000000	−0.0000007621

k	Υ^k_{1}	Υ^k_{2}	Υ^k_{3}	Υ^k_{4}
−4	0.0000000000	0.0000000000	0.0000000000	0.0000000000
−3	0.0000004887	0.0000000000	0.0000000000	0.0000000000
−2	0.0002498264	0.0000019494	0.0000000000	0.0000000000
−1	0.0378102693	0.0012518005	−0.0000004464	0.0000000000
0	−0.2484459006	−0.0164513443	−0.0007261486	−0.0000007621
1	−0.6271755060	0.0874622766	0.0049255216	−0.0000324556
2	0.0874622766	0.0935483714	−0.0207415149	0.0001339407
3	0.0049255216	−0.0207415149	0.0023763642	−0.0004456481
4	−0.0000324556	0.0001339407	−0.0004456481	0.0000024593

B.4 Hessian Mode Expansion

In order to derive an expression for the Hessian matrix of the mode expansion first and second order derivatives of the effective action in the homogeneous vacuum $\hat{\sigma} = 0$ are listed below with the use of $\hat{p} = \hat{p}(m)$ and $\hat{p}' = \hat{p}(m')$ from (4.48)

$$\begin{aligned}\frac{\partial(Q^\dagger Q)}{\partial\Sigma_{2m'}} &= 2\gamma_0\hat{\mu}\left(\delta_{\hat{k}_1,\hat{p}'+\hat{k}_1'} + \delta_{\hat{k}_1,-\hat{p}'+\hat{k}_1'}\right) \\ &\quad + 2\mathbf{I}_2 \sum_{\substack{m=-M \\ m\neq 0}}^{M} \sigma_m \left(\delta_{\hat{k}_1,\hat{p}+\hat{p}'+\hat{k}_1'} + \delta_{\hat{k}_1,\hat{p}-\hat{p}'+\hat{k}_1'}\right) \qquad \text{(B.15)} \\ \frac{\partial(Q^\dagger Q)}{i\partial\Sigma_{2m'+1}} &= 2\gamma_0\hat{\mu}\left(\delta_{\hat{k}_1,\hat{p}'+\hat{k}_1'} - \delta_{\hat{k}_1,-\hat{p}'+\hat{k}_1'}\right) \\ &\quad + 2\mathbf{I}_2 \sum_{\substack{m=-M \\ m\neq 0}}^{M} \sigma_m \left(\delta_{\hat{k}_1,\hat{p}+\hat{p}'+\hat{k}_1'} - \delta_{\hat{k}_1,\hat{p}-\hat{p}'+\hat{k}_1'}\right) . \qquad \text{(B.16)}\end{aligned}$$

Following (4.51) and the additivity of the trace, only diagonal elements of the second order derivative term are relevant such that no mixed derivatives of Σ_{2m} and Σ_{2m+1} appear. It is straightforward to check that the inverse of $(Q^\dagger Q)$ due to its block-diagonal structure for $\hat{\sigma} = 0$ becomes

$$(Q^\dagger Q)^{-1} = \delta_{\hat{k}_1,\hat{k}_1'} \frac{(\hat{k}_0^2 + \hat{k}_1^2 + \hat{\mu}^2)\mathbf{I}_2 + 2i\gamma_5\hat{k}_1\hat{\mu}}{(\hat{k}_0^2 + \hat{k}_1^2 - \hat{\mu}^2)^2 + (2\hat{\mu}\hat{k}_0)^2} . \qquad \text{(B.17)}$$

Together with the second order derivative terms

$$\begin{aligned}\frac{\partial^2(Q^\dagger Q)}{\partial\Sigma_{2m'}\partial\Sigma_{2m''}} &= 2\mathbf{I}_2\left(\delta_{\hat{k}_1,\hat{p}''+\hat{p}'+\hat{k}_1'} + \delta_{\hat{k}_1,\hat{p}'-\hat{p}''+\hat{k}_1'}\right. \\ &\quad \left. + \delta_{\hat{k}_1,-\hat{p}'+\hat{p}''+\hat{k}_1'} + \delta_{\hat{k}_1,-\hat{p}'-\hat{p}''+\hat{k}_1'}\right) , \qquad \text{(B.18)}\end{aligned}$$

where the differentiation w.r.t. Σ_{2m+1} has equal diagonal terms, we arrive at the trace of the first term in the sum of (4.51)

$$(Q^\dagger Q)^{-1}_{\hat{k}_1,\hat{k}_2} \frac{\partial^2(Q^\dagger Q)}{\partial\Sigma_{m'}\partial\Sigma_{m''}}\Big|_{\hat{k}_2,\hat{k}_1} = 4\delta_{\hat{k}_1,\hat{k}_1'}\delta_{\hat{p}',\hat{p}''} \frac{(\hat{k}_0^2 + \hat{k}_1^2 + \hat{\mu}^2)\mathbf{I}_2 + 2i\gamma_5\hat{k}_1\hat{\mu}}{(\hat{k}_0^2 + \hat{k}_1^2 - \hat{\mu}^2)^2 + (2\hat{\mu}\hat{k}_0)^2} . \qquad \text{(B.19)}$$

Using the first order derivative terms and the expression for the inverse in (B.17) one obtains as an intermediate result the product of

$$\begin{aligned}B^{\hat{p}'}_{\hat{k}_1,\hat{k}_1'} &= (Q^\dagger Q)^{-1}_{\hat{k}_1,\hat{k}_2} \frac{\partial(Q^\dagger Q)}{\partial\Sigma_{2m'}}\Big|_{\hat{k}_2,\hat{k}_1'} \\ &= \frac{(\hat{k}_0^2 + \hat{k}_1^2 + \hat{\mu}^2)\mathbf{I}_2 + 2i\gamma_5\hat{k}_1\hat{\mu}}{(\hat{k}_0^2 + \hat{k}_1^2 - \hat{\mu}^2)^2 + (2\hat{\mu}\hat{k}_0)^2} \\ &\quad \times \left(2\gamma_0\hat{\mu} + i(\hat{k}_1 - \hat{k}_1')\gamma_1\right)\left(\delta_{\hat{k}_1-\hat{k}_1',\hat{p}'} + \delta_{\hat{k}_1-\hat{k}_1',-\hat{p}'}\right) . \qquad \text{(B.20)}\end{aligned}$$

Finally, the second term in the sum of (4.51) becomes

$$\begin{aligned}B^{\hat{p}'}_{\hat{k}_1,\hat{k}_2} B^{\hat{p}''}_{\hat{k}_2,\hat{k}_1'} &= \delta_{\hat{p}',\hat{p}''} \sum_{m=\{-m',m'\}} \left(\delta_{\hat{k}_1'-\hat{k}_1,\hat{p}'+\hat{p}} \pm \delta_{\hat{k}_1-\hat{k}_1',-\hat{p}'+\hat{p}}\right) \\ &\quad \times \frac{(\hat{k}_0^2 + \hat{k}_1^2 + \hat{\mu}^2)\mathbf{I}_2 + 2i\gamma_5\hat{k}_1\hat{\mu}}{(\hat{k}_0^2 + \hat{k}_1^2 - \hat{\mu}^2)^2 + (2\hat{\mu}\hat{k}_0)^2}\left(2\gamma_0\hat{\mu} + i(\hat{k}_1 - (\hat{k}_1' + \hat{p}))\gamma_1\right) \\ &\quad \times \frac{(\hat{k}_0^2 + (\hat{k}_1' + \hat{p})^2 + \hat{\mu}^2)\mathbf{I}_2 + 2i\gamma_5(\hat{k}_1' + \hat{p})\hat{\mu}}{(\hat{k}_0^2 + (\hat{k}_1' + \hat{p})^2 - \hat{\mu}^2)^2 + (2\hat{\mu}k_0)^2}\left(2\gamma_0\hat{\mu} + i((\hat{k}_1' + \hat{p}) - \hat{k}_1')\gamma_1\right) . \qquad \text{(B.21)}\end{aligned}$$

Bibliography

[1] K.-H. Bennemann and J. B. Ketterson, *Novel Superfluids*, Volume 1. Oxford University Press, 10.1093/acprof:oso/9780199585915.001.0001.

[2] P. de Forcrand, *Simulating QCD at finite density,* PoS **LAT2009** (2010) 010.

[3] D. J. Gross and A. Neveu, *Dynamical Symmetry Breaking in Asymptotically Free Field Theories,* Phys. Rev. **D10** (1974) 3235.

[4] Y. Nambu and G. Jona-Lasinio, *Dynamical Model of Elementary Particles Based on an Analogy with Superconductivity. II,* Phys. Rev. **124** (1961) 246.

[5] U. Vogl and W. Weise, *The Nambu and Jona-Lasinio model: Its implications for Hadrons and Nuclei,* Progress in Particle and Nuclear Physics **27** (1991) 195.

[6] T. Hatsuda and T. Kunihiro, *QCD phenomenology based on a chiral effective Lagrangian,* Physics Reports **247** (1994) 221.

[7] U. Wolff, *The phase diagram of the infinite-N Gross-Neveu model at finite temperature and chemical potential,* Physics Letters B **157** (1985) 303.

[8] M. Thies and K. Urlichs, *Revised phase diagram of the Gross-Neveu model,* Phys. Rev. D **67** (2003) 125015.

[9] R. F. Dashen, B. Hasslacher and A. Neveu, *Semiclassical bound states in an asymptotically free theory,* Phys. Rev. D **12** (1975) 2443.

[10] A. Heinz, F. Giacosa, M. Wagner and D. H. Rischke, *Inhomogeneous condensation in effective models for QCD using the finite-mode approach,* Phys. Rev. D **93** (2016) 014007.

[11] T. Kojo, Y. Hidaka, L. McLerran and R. D. Pisarski, *Quarkyonic chiral spirals,* Nuclear Physics A **843** (2010) 37.

[12] P. de Forcrand and U. Wenger, *Baryonic matter in the lattice Gross-Neveu model. New baryon matter in the lattice Gross-Neveu model,* PoS **LAT2006** (2006) 152.

[13] P. Hasenfratz and F. Karsch, *Chemical Potential on the Lattice,* Phys. Lett. **B125** (1983) 308.

[14] M. Wagner and F. Lenz, *The pseudoparticle approach for solving path integrals in gauge theories,* PoS **LAT2005** (2006) 315.

[15] I. Daubechies, *Orthonormal bases of compactly supported wavelets,* Communications on Pure and Applied Mathematics **41** (1988) 909.

[16] M. Thies, *Non-Abelian twisted kinks in chiral Gross-Neveu model with isospin,* Phys. Rev. D **93** (2016) 085024.

[17] G. Başar, G. V. Dunne and M. Thies, *Inhomogeneous condensates in the thermodynamics of the chiral NJL2model,* Phys. Rev. D **79** (2009) 105012.

[18] S. Coleman, *There are no Goldstone bosons in two dimensions,* Commun.Math. Phys. **31** (1973) 259.

[19] N. D. Mermin and H. Wagner, *Absence of Ferromagnetism or Antiferromagnetism in One- or Two-Dimensional Isotropic Heisenberg Models,* Phys. Rev. Lett. **17** (1966) 1133.

[20] R. F. Dashen, S.-K. Ma and R. Rajaraman, *Finite-temperature behavior of a relativistic field theory with dynamical symmetry breaking,* Phys. Rev. D **11** (1975) 1499.

[21] P. Ramond, *Field Theory*, A Modern Primer. Westview Press, Mar., 1997.

[22] Y. Frishman and J. Sonnenschein, *Non-perturbative field theory: From two-dimensional conformal field theory to QCD in four dimensions*. Cambridge University Press, 2014.

[23] A. Hasenfratz and D. Toussaint, *Canonical ensembles and nonzero density quantum chromodynamics,* Nucl. Phys. **B371** (1992) 539.

[24] S. P. Klevansky, *The Nambu—Jona-Lasinio model of quantum chromodynamics,* Reviews of Modern Physics **64** (1992) 649.

[25] S. Carignano, M. Buballa and B.-J. Schaefer, *Inhomogeneous phases in the quark-meson model with vacuum fluctuations,* Phys. Rev. D **90** (2014) 014033.

[26] C. Itzykson and J. B. Zuber, *Quantum Field Theory*, International Series In Pure and Applied Physics. McGraw-Hill, New York, 1980.

[27] D. Nickel, *Inhomogeneous phases in the Nambu–Jona-Lasinio and quark-meson model,* Phys. Rev. D **80** (2009) 074025.

[28] M. Wagner, *Properties of confining gauge field configurations in the pseudoparticle approach,* in *AIP Conference Proceedings*, pp. 231–234, AIP, 2007, DOI.

[29] M. Wagner, *Classes of confining gauge field configurations,* Phys. Rev. D **75** (2007) 016004.

[30] M. Wagner, *Fermions in the pseudoparticle approach,* Phys. Rev. D **76** (2007) 076002.

[31] J. I. Kapusta and C. Gale, *Finite-Temperature Field Theory*, Principles and Applications. Cambridge University Press, Cambridge, 2 ed., 2009, 10.1017/CBO9780511535130.

[32] G. Farin, *Curves and surfaces for CAGD: a practical guide, 5th edition*. Morgan Kaufmann Publishers Inc., 5 ed., Oct., 2001.

[33] I. Daubechies, *Ten Lectures on Wavelets*. Society for Industrial and Applied Mathematics, jan, 1992, 10.1137/1.9781611970104.

[34] P. Auscher, *Wavelet bases for $L^2(\mathbb{R})$ with rational dilation factor ,* in *Wavelets and their applications*, pp. 439–451. Jones & Bartlett Pub, New York, NY, 1992.

[35] P. G. Lemarié-Rieusset and Y. Meyer, *Ondelettes et bases hilbertiennes,* Revista Matemática Iberoamericana **2** (1986) 1.

[36] A. C. H. Rowe and P. C. Abbott, *Daubechies wavelets and Mathematica,* Computers in Physics **9** (1995) 635.

[37] L. Andrew, E. Tenenbaum and H. L. Resnikoff, *The evaluation of connection coefficients of compactly supported wavelets ,* Tech. Rep. AD910708, Princeton, jun, 1991.

[38] G. Beylkin, *On the Representation of Operators in Bases of Compactly Supported Wavelets,* SIAM Journal on Numerical Analysis **29** (1992) 1716.

[39] J. M. Restrepo and G. K. Leaf, *Inner product computations using periodized Daubechies wavelets,* International Journal for Numerical Methods in Engineering **40** (1997) 3557.

[40] C. Romine and B. Peyton, *Computing connection coefficients of compactly supported wavelets on bounded intervals,* tech. rep., Oak Ridge National Laboratory (ORNL), Oak Ridge, TN, apr, 1997. 10.2172/661583.

[41] D. Nickel, *Inhomogeneous phases in the Nambu-Jona-Lasino and quark-meson model,* Phys. Rev. **D80** (2009) 074025.

[42] F. Karsch, J. B. Kogut and H. W. Wyld, *The Gross-Neveu Model at Finite Temperature and Density,* Nucl. Phys. **B280** (1987) 289.

[43] C. Gattringer and C. B. Lang, *Quantum chromodynamics on the lattice: an introductory presentation*, vol. 788 of *Lecture Notes in Physics*. Springer, Berlin, 2010, 10.1007/978-3-642-01850-3.

[44] Y. Cohen, S. Elitzur and E. Rabinovici, *A Monte Carlo study of the Gross-Neveu model,* Nuclear Physics B **220** (1983) 102.

[45] O. Schnetz, M. Thies and K. Urlichs, *Phase diagram of the Gross–Neveu model: exact results and condensed matter precursors,* Annals of Physics **314** (2004) 425.

[46] G. Dunne and J. Feinberg, *Self-isospectral periodic potentials and supersymmetric quantum mechanics,* Phys. Rev. D **57** (1998) 1271.

[47] M. Buballa and S. Carignano, *Inhomogeneous chiral condensates,* Progress in Particle and Nuclear Physics **81** (2015) 39.

[48] D. Nickel and M. Buballa, *Solitonic ground states in (color) superconductivity,* Phys. Rev. D **79** (2009) 054009.

[49] J. Ma and G. Plonka, *A review of curvelets and recent applications,* IEEE Signal Processing Magazine (2010) .

[50] M. V. Altaisky and N. E. Kaputkina, *Continuous wavelet transform in quantum field theory,* Physical Review D **88** (2013) 025015 [1304.7177].

[51] S. Singh and G. K. Brennen, *Holographic Construction of Quantum Field Theory using Wavelets,* 1606.05068.

[52] G. K. Brennen, P. Rohde, B. C. Sanders and S. Singh, *Multiscale quantum simulation of quantum field theory using wavelets,* Physical Review A **92** (2015) 032315 [1412.0750].

[53] G. Vidal, *Entanglement renormalization,* Physical Review Letters **99** (2005) 220405 [cond-mat/0512165].

[54] J. Hubbard, *Calculation of Partition Functions,* Phys. Rev. Lett. **3** (1959) 77.

List of Figures

List of Tables